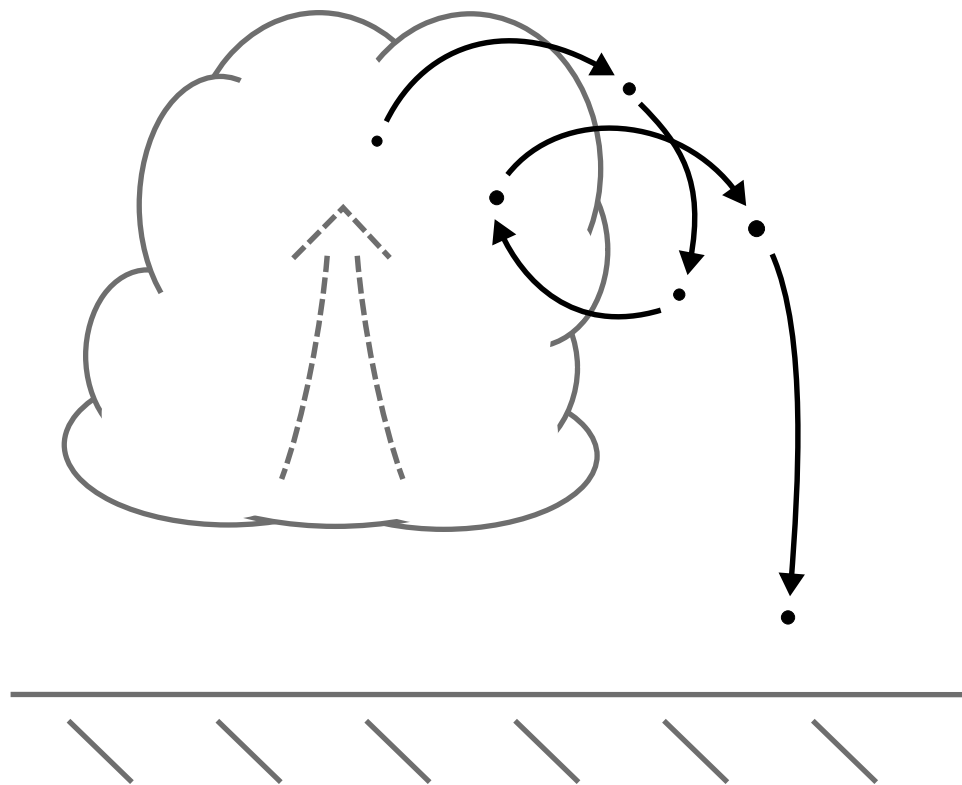




Cloud structures and rain formation in the atmospheric boundary layer



Ann Kristin Naumann

Hamburg 2015

Hinweis

Die Berichte zur Erdsystemforschung werden vom Max-Planck-Institut für Meteorologie in Hamburg in unregelmäßiger Abfolge herausgegeben.

Sie enthalten wissenschaftliche und technische Beiträge, inklusive Dissertationen.

Die Beiträge geben nicht notwendigerweise die Auffassung des Instituts wieder.

Die "Berichte zur Erdsystemforschung" führen die vorherigen Reihen "Reports" und "Examensarbeiten" weiter.

Anschrift / Address

Max-Planck-Institut für Meteorologie
Bundesstrasse 53
20146 Hamburg
Deutschland

Tel./Phone: +49 (0)40 4 11 73 - 0
Fax: +49 (0)40 4 11 73 - 298

name.surname@mpimet.mpg.de
www.mpimet.mpg.de

Notice

The Reports on Earth System Science are published by the Max Planck Institute for Meteorology in Hamburg. They appear in irregular intervals.

They contain scientific and technical contributions, including Ph. D. theses.

The Reports do not necessarily reflect the opinion of the Institute.

The "Reports on Earth System Science" continue the former "Reports" and "Examensarbeiten" of the Max Planck Institute.

Layout

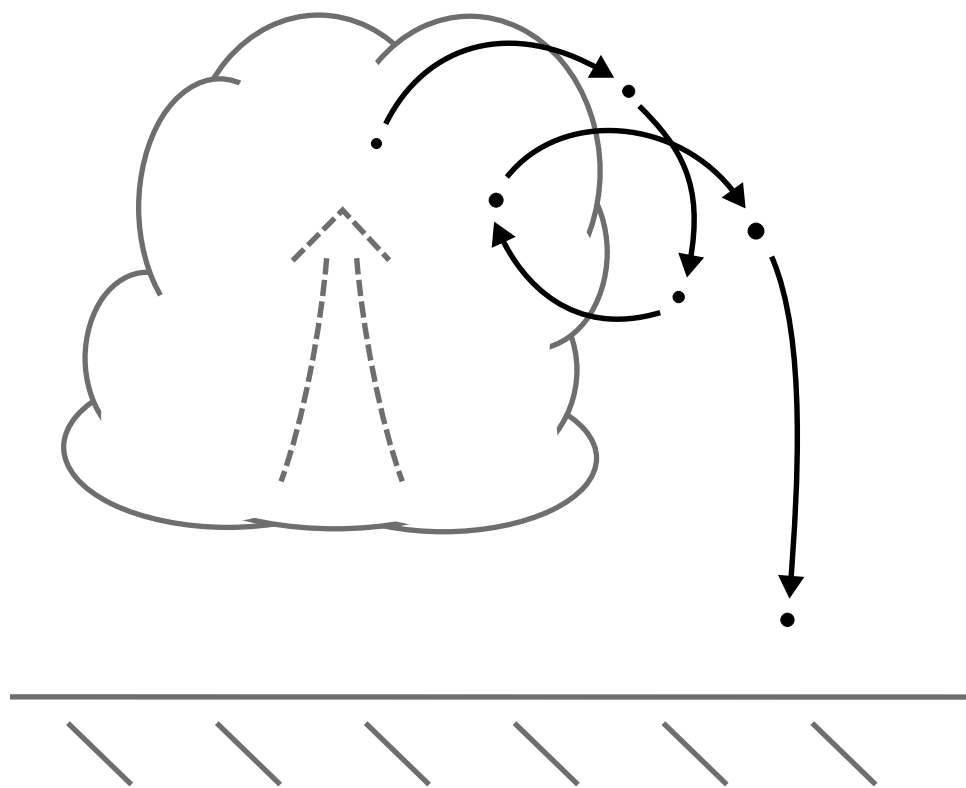
Bettina Diallo and Norbert P. Noreiks
Communication

Copyright

Photos below: ©MPI-M
Photos on the back from left to right:
Christian Klepp, Jochem Marotzke,
Christian Klepp, Clotilde Dubois,
Christian Klepp, Katsumasa Tanaka



Cloud structures and rain formation in the atmospheric boundary layer



Ann Kristin Naumann

Hamburg 2015

Ann Kristin Naumann

Max-Planck-Institut für Meteorologie
Bundesstrasse 53
20146 Hamburg

Als Dissertation angenommen
vom Fachbereich Geowissenschaften der Universität Hamburg

auf Grund der Gutachten von
Prof. Dr. Felix Ament
und
Dr. Axel Seifert

Hamburg, den 21.05.2015
Professor Dr. Christian Betzler
Leiter des Departments Geowissenschaften

ABSTRACT

Dynamical, thermodynamical and microphysical interactions on vastly different spatial and temporal scales determine the structure of clouds and the formation of precipitation. This thesis investigates the effect of small-scale variability on the representation of shallow clouds in large-scale models and on particle-kinetic processes that lead to the formation of precipitation without the occurrence of ice particles.

Using large-eddy simulations of different shallow cloud regimes, a cloud parametrisation for large-scale models that is based on probability density functions is revisited. A regime dependent characteristic behaviour of the probability density functions is found, which can be taken into account by relaxing the strict antisymmetry of the original closure equations and allow cumulus updrafts to be more vigorous than stratocumulus downdrafts. In a priori tests the new set of closure equations reduces the error of the cloud parametrisation for the shallow cumulus regime.

To investigate warm rain microphysical processes on a particle-based level, a Lagrangian drop model is developed that explicitly includes all relevant processes for raindrop growth such as accretional growth from cloud water, selfcollection among raindrops, evaporation and sedimentation. A sensitivity study reveals that the amount of surface precipitation and the slope of the raindrop size distribution are sensitive to the representation of selfcollection in the Lagrangian drop model. The uncertainties in the formulation of the Lagrangian drop model are found to be clearly smaller than uncertainties inherent in a bulk rain microphysics parametrisation.

The Lagrangian drop model is applied to study the development of the raindrop size distribution in individual shallow cumulus clouds. The shape of the raindrop size distribution depends on the stage of the lifecycle of the cloud and closure assumptions currently used in bulk rain microphysics parametrisations, which have been developed for more heavily precipitating cases, are not able to capture this dependence.

Furthermore, the Lagrangian drop model allows us to analyse the growth histories of raindrops. Recirculation of raindrops – a process that is not represented by bulk rain microphysics parametrisations in large-scale models – is found to be common in shallow cumulus and to contribute distinctly to the surface precipitation.

ZUSAMMENFASSUNG

Wechselwirkungen dynamischer, thermodynamischer und mikrophysikalischer Prozesse auf sehr unterschiedlichen räumlichen und zeitlichen Skalen bestimmen sowohl das Erscheinungsbild von Wolken als auch die Niederschlagsbildung. Diese Dissertation untersucht den Einfluss kleinräumiger Variabilität auf flache Konvektion und auf eisfreie Niederschlagsbildung mithilfe von hochauflösenden, numerischen Simulationen.

Zunächst werden Simulationen unterschiedlicher Wolkenregime verwendet, um die Regimeabhängigkeit einer Wolkenparametrisierung, die auf Wahrscheinlichkeitsdichtefunktionen basiert, zu untersuchen. Dabei zeigt sich eine Regimeabhängigkeit in den Wahrscheinlichkeitsdichtefunktionen, die durch eine Änderung in den Schließungsgleichungen der Wolkenparametrisierung berücksichtigt werden kann. Die neuen Schließungsgleichungen verwerfen die Annahme einer strengen Antisymmetrie der Aufwinde im Cumulusregime gegenüber den Abwinden im Stratocumulusregime und reduzieren den Fehler der Wolkenparametrisierung im Cumulusregime in A-priori-Tests.

Des Weiteren wird zur Untersuchung mikrophysikalischer Prozesse der Niederschlagsbildung ein Lagrangesches Tropfenmodell entwickelt, das alle relevanten Prozesse des eisfreien Regentropfenwachstums explizit simuliert: Akkreszenz von Wolkenwasser, Selbsteinfang von Regentropfen, Verdunstung und Sedimentation. Eine Sensitivitätsstudie ergibt, dass die Bodenniederschlagsmenge und die Regentropfenverteilung von der Darstellung des Selbsteinfangs in dem Lagrangeschen Modell abhängt. Weitere Simulationen zeigen, dass Unsicherheiten in der Formulierung des Lagrangeschen Modells deutlich kleiner sind als die inhärenten Unsicherheiten in einer klassischen momentenbasierten mikrophysikalischen Parametrisierung.

Eine Untersuchung der Entwicklung der Regentropfenverteilung in einzelnen Cumuluswolken mit dem Lagrangeschen Tropfenmodell ergibt, dass die Form der Regentropfenverteilung von dem Stadium der Wolke in seinem Lebenszyklus abhängt. Existierende Schließungsgleichungen, die in momentenbasierten mikrophysikalischen Parametrisierungen verwendet werden und die für stärker regnende Wolken entwickelt wurden, sind nicht in der Lage diese Abhängigkeit wiederzugeben.

Das Lagrangesche Tropfenmodell ermöglicht außerdem eine Analyse der Wachstumsgeschichte von Regentropfen. Simulationen eines Cumuluswolkenfeldes zeigen, dass die Zirkulation von Regentropfen – ein Prozess, der in den momentenbasierten mikrophysikalischen Parametrisierungen großskaliger Modellen nicht dargestellt wird – in flachen Cumuluswolken weitverbreitet ist und erheblich zum Bodenniederschlag beiträgt.

CONTENTS

Abstract	I
Zusammenfassung	III
1. Introduction	1
1.1. Barriers to an improved understanding of shallow clouds and precipitation .	2
1.2. Parametrisation of subgrid cloud fraction and microphysical process rates .	4
1.3. A Lagrangian approach for warm rain microphysics	5
1.4. Parametrisation of the raindrop size distribution	8
1.5. A particle-based view on warm microphysics	9
2. A refined statistical cloud closure using double-Gaussian probability density functions	13
2.1. Introduction	14
2.2. Model and data	16
2.2.1. Large-Eddy Simulations	16
2.2.2. Observational data	17
2.3. Introducing a refined cloud closure	18
2.3.1. Data analysis: the double-Gaussian PDF	18
2.3.2. Closure equations considering the regime dependent cloud structures	21
2.3.3. Parametrisation of the liquid water flux	26
2.4. A priori testing of the cloud closure	27
2.5. Error dependence on domain size and the role of mesoscale structures . . .	31

2.6. Extension to autoconversion rate	33
2.7. Conclusions	36
3. A Lagrangian drop model to study warm rain microphysical processes	39
3.1. Introduction	40
3.2. Test case description	42
3.2.1. Large-Eddy Simulation	42
3.2.2. Case setup	42
3.3. Lagrangian drop model	43
3.3.1. Initialisation	45
3.3.2. Trajectory	46
3.3.3. Evaporation and accretion	49
3.3.4. Selfcollection	50
3.3.5. Implementation	52
3.4. Turbulent velocity fluctuations and their effect on collision frequency	53
3.5. Assessment of the bulk microphysics scheme	60
3.6. Conclusions	62
4. On the development of the shape of the raindrop size distribution in shallow cumulus	65
4.1. Introduction	66
4.2. Cloud lifecycle	68
4.3. The RSD's shape parameter	76
4.3.1. Sensitivity of the bulk scheme to the RSD's shape parameter	76
4.3.2. Evolution of the RSD's shape parameter in the LD model	78
4.4. Conclusions	80
5. Recirculation and growth of raindrops in shallow cumulus	83
5.1. Introduction	84
5.2. Model setup	85
5.3. Characterisation of raindrops in a field of shallow cumulus	86
5.3.1. Cloud field statistics	86
5.3.2. Lagrangian drop trajectory	89
5.3.3. Lagrangian drop statistics	90
5.4. Raindrop growth	92
5.4.1. Accretion and selfcollection	92
5.4.2. The role of recirculation	96
5.5. Conclusions	103

6. Conclusions	105
6.1. Developed models and methods	105
6.2. Results	106
6.3. The next steps	109
6.4. Conclusions	111
Appendix	113
A. Derivation of the assumed PDF	113
B. Density dependence of the terminal fall velocity	115
C. Numerical integration of the LD's momentum equation	116
D. Additional sample trajectories	117
Bibliography	IX

CHAPTER 1

INTRODUCTION

It will come as a surprise to most laymen and to not a few meteorologists to be told that there are still unsolved problems regarding the formation of rain.

(Sir George C. Simpson, 1941)

The representation of clouds and precipitation in atmospheric models is a long-standing and widely-recognised source of uncertainty (e.g., Stevens and Bony, 2013; Jakob, 2014). Precipitation is one of the most poorly simulated quantities in general circulation models (GCMs; Hawkins and Sutton, 2011), numerical weather prediction (NWP) models (Olson et al., 1995; Stephens et al., 2010) and in high-resolution models such as Large-Eddy Simulations (LES; van Zanten et al., 2011). While the long-term global mean accumulated precipitation is constrained by the energy balance of the Earth and is in good agreement with observations, this agreement breaks down if regional accumulations are considered (Stephens et al., 2010). In climate models the uncertainty in estimating climate sensitivity, i.e., the change in global mean temperature for a doubling of CO₂ concentration in the atmosphere, largely results from differences in the cloud response, in particular the low cloud response (Bony and Dufresne, 2005; Soden and Held, 2006; Randall et al., 2007; Dufresne and Bony, 2008; Boucher et al., 2013). Despite these uncertainties, clouds and

precipitation have a high relevance for society: besides extreme events also routine weather variations have a strong influence on economy (Lazo et al., 2011), floods related to extreme precipitation can cause serious damage (Pielke and Downton, 2000) and soil erosion in most regions worldwide is predominantly caused by precipitation (Pimentel et al., 1995). A precise forecast of clouds and precipitation can help to mitigate the impacts of weather variability (Jasper et al., 2002; Lazo et al., 2011; Smiatek et al., 2012). To advance the representation of clouds and precipitation in numerical models, an improved understanding of the processes involved in their formation and development is essential.

This thesis strives to contribute to an advanced understanding of the representation of shallow clouds in large-scale models and of the processes that lead to the formation of precipitation. An LES model is used to investigate cloud structures and the formation of precipitation on a process level focusing on marine shallow convection. For the cloud fraction the subgrid-scale variability of temperature and moisture is key to understand how different shallow cloud regimes are represented in models with a coarse resolution. Small-scale variability and turbulence are also key to rain formation, where particle-fluid interaction and particle-particle interaction determine the development of precipitation. To study the formation of precipitation on a particle-based level, a Lagrangian model for warm rain microphysical processes is developed and applied to investigate the evolution of the raindrop size distribution. The growth histories of raindrops, which are exposed to in-cloud variability, are analysed to identify mechanisms that promote the formation of surface precipitation such as the recirculation of raindrops in the cloud layer.

The following section seeks to explain the importance of shallow clouds in the tropical atmospheric boundary layer and the difficulties encountered when representing clouds and precipitation in numerical models. The subsequent sections of this introductory chapter place the individual research questions for each chapter into the context of scientific knowledge. More specific background information is given in the introduction of each individual chapter.

1.1. Barriers to an improved understanding of shallow clouds and precipitation

Shallow clouds are ubiquitous over the world's tropical oceans and influence the radiation budget especially in the shortwave because they sharply increase the albedo compared to the underlying less reflective ocean. They couple the boundary layer dynamically to the free troposphere by the transport of heat, moisture and momentum, and thereby modify the boundary layer height and the vertical profiles of temperature, humidity and motion (Riehl et al., 1951). In the tropics shallow clouds are characterised by warm microphysics, i.e., cloud tops are at temperatures above or just slightly below freezing and hence the formation of precipitation is not further complicated by the occurrence of ice. Although

shallow clouds mostly produce light precipitation, they contribute 20-30 % to the total precipitation amount and 70 % to the total precipitation area over tropical oceans (Short and Nakamura, 2000; Lau and Wu, 2003). Precipitation induced by shallow clouds plays an important role for the evolution of the boundary layer structure, e.g., by the formation of cold pools that triggers organisation in shallow cumulus (Jensen et al., 2000; Seifert and Heus, 2013) or the transition from closed to open cellular structures in stratocumulus (van Zanten and Stevens, 2005; Stevens et al., 2005b; Savic-Jovicic and Stevens, 2008; Wang and Feingold, 2009a;b; Sandu and Stevens, 2011; Feingold et al., 2015).

The difficulty of simulating clouds and precipitation lies in the multiscale nature of the problem and in the interplay of dynamical, thermodynamical and microphysical processes across these scales. Cloud processes act on a broad range of scales from cloud droplet size of few micrometers to cloud structures of several hundreds of kilometres. Such orders of magnitude in scale cannot be resolved by numerical models. Today, GCMs have a horizontal resolution of a few hundreds of kilometres, while LES models resolve scales down to few tens of meters but for a limited domain. All processes that act on scales smaller than those resolved have to be parametrised, i.e., the effect of subgrid-scale processes on the grid-scale variables is represented based on grid-scale variables. In addition to the broad range of scales, processes and phenomena on vastly different scales are also interacting, which is a property that characterises all nonlinear systems. Processes on the smallest scales, such as the growth of cloud droplets and raindrops, determine the macroscopic properties of a cloud, such as its lifecycle or its radiative properties. Due to their coupling to the dynamics, small errors in the representation of clouds and precipitation in a particular location spread and amplify quickly through circulation changes (Jakob, 2014). To improve the parametrisation of clouds and precipitation, a good understanding of the processes involved is essential.

Understanding rain formation, even for relatively simple, shallow cumulus clouds, has proven to be difficult. For shallow cumulus early observational studies have roughly related the cloud depth to surface precipitation but also stressed variability among clouds and the need for a more detailed understanding of rain formation (Byers and Hall, 1955). More recent studies focused on particular aspects of shallow cumulus clouds and found that they are laterally covered by a subsiding shell that has a horizontal dimension of only a few meters (Rodts et al., 2003; Heus and Jonker, 2008) and that entrainment of dry air into the cloud is dominated by small entrainment parcels, which have a size on the order of meters and which do not penetrate far into the cloud (Gerber et al., 2008). This implies that in numerical modelling high-resolution is needed in order to be able to represent process that are important for the development of shallow cumulus clouds.

Another hindrance towards an improved understanding of clouds and the formation of precipitation is the limited availability of reliable observational data that allows for a detailed analyses of microphysical processes. Some desired quantities are impossible to

measure directly, e.g., microphysical collection rates such as accretion. In-situ observations and to a lesser extent also remote sensing data are limited in spatial and temporal resolution and extent. Especially in remote sensing, microphysically meaningful quantities are derived from the measured signal by applying an inversion procedure with often uncertain assumptions. For instance rain rates are derived from radar reflectivities by applying an empirical relationship or by assuming the shape of the raindrop size distribution, a quantity that is not well known (Zhang et al., 2001; 2003; Munchak and Tokay, 2008). Extensive field campaigns such as those described by Stevens et al. (2003) or Rauber et al. (2007) try to close this gap by combining a range of different instruments and platforms, but they are extremely costly and hence limited in spatial and temporal extent. To probe dynamical and microphysical properties of individual clouds on high resolution, helicopter-borne measurements are promising (Siebert et al., 2006) and have recently been analysed to characterise shallow cumulus in different stages of their lifecycle (Katzwinkel et al., 2014; Schmeissner et al., 2015).

Because of the limitations of observational data, high resolution modelling is often a rewarding and sometimes the only alternative. Nevertheless, also high resolution models have several limitations mostly due to subgrid-scale processes that have to be parametrised such as radiation, turbulence and microphysics. Therefore, if potentially important processes or phenomena can be identified from high resolution modelling, an essential next step is to confirm their existence and at best also their relevance from observational data.

1.2. Parametrisation of subgrid cloud fraction and microphysical process rates

Temperature and humidity vary on spatial scales smaller than the typical size of a large-scale model's grid box (e.g., Smagorinsky, 1960; Sundqvist et al., 1989). If the subgrid-scale variability is not taken into account, the cloud fraction inferred from the grid box average values will always be zero for a grid box that on average is subsaturated (Fig. 1.1 a) and one for a grid box that on average is saturated. If the subgrid-scale variability is taken into account, the cloud fraction can be larger than zero for a grid box that on average is subsaturated (Fig. 1.1 b). For warm clouds, i.e., without the ice phase, the assumption that supersaturation is immediately depleted by condensation and that cloud droplets immediately evaporate in subsaturated air is a good approximation to reality. Therefore, the cloud fraction and the liquid water content can be deduced by integrating over the probability density function (PDF) of temperature and moisture, which characterises the subgrid variability.

For large waterdrops the assumption of immediate evaporation in subsaturated air is not valid. Therefore, bulk rain microphysics parametrisations usually distinguish between cloud water and rainwater, and prognostic equations are established for the development

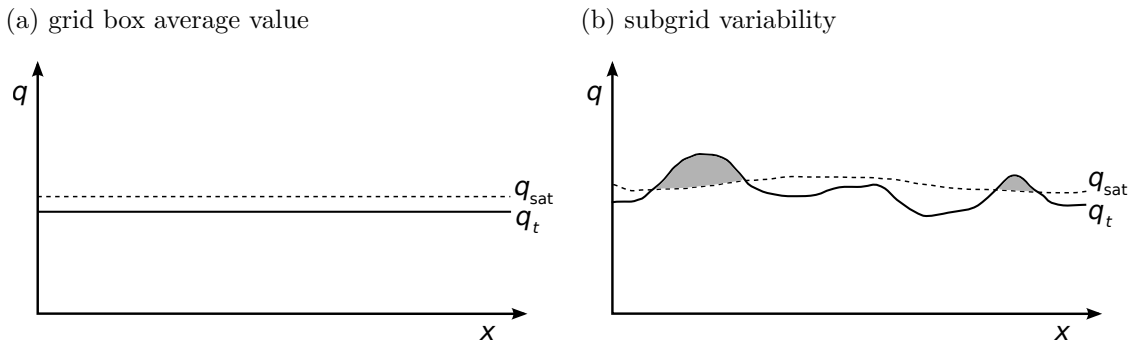


Figure 1.1.: The concept of a subgrid-scale cloud parametrization. (a) If the grid box average total water mixing ratio, q_t , is smaller than the saturation mixing ratio, q_{sat} , the diagnosed cloud fraction from the mean values is zero. (b) For the same mean values but taking the subgrid variability of q_t and q_{sat} into account, the cloud fraction can be larger than zero (grey area).

of the rainwater amount in a grid box. Like the cloud fraction, microphysical process rates – autoconversion, accretion, selfcollection (Fig. 1.2) and evaporation – encounter biases if the subgrid-scale variability in the model’s grid box is neglected because the microphysical process rates do not depend linearly on the bulk field variables (Pincus and Klein, 2000; Chosson et al., 2014).

Parametrisations of boundary layer clouds, which assume different shapes of the PDF, are often used in NWP models or GCMs (Sommeria and Deardorff, 1977; Mellor, 1977; Bougeault, 1982a; Tompkins, 2002). In recent years closures using 5-parameter double-Gaussian PDFs have become increasingly popular because the double-Gaussian distribution can provide very accurate fits to observed or simulated empirical PDFs (Lewellen and Yoh, 1993; Larson et al., 2001a; Perraud et al., 2011). Even if it is assumed that the first three moments of the subgrid PDF can be predicted in large scale models, the number of parameters still has to be reduced from five to three, i.e., two closure equations are necessary. In Chapter 2 a refinement of the closure equations from Larson et al. (2001a) is proposed. Analysing cases of shallow cumulus, stratocumulus and stratocumulus-to-cumulus transition from LES as well as observational data the following questions are posed:

How can the characteristics of different cloud regimes be taken into account in the parametrization of the cloud fraction? Can PDF-based parametrizations be extended to diagnose microphysical process rates?

1.3. A Lagrangian approach for warm rain microphysics

The basic processes underlying the development of cloud water and rainwater are particle-fluid and particle-particle interactions: individual cloud droplets and raindrops interact with their environment (by condensation and evaporation, and by momentum transfer

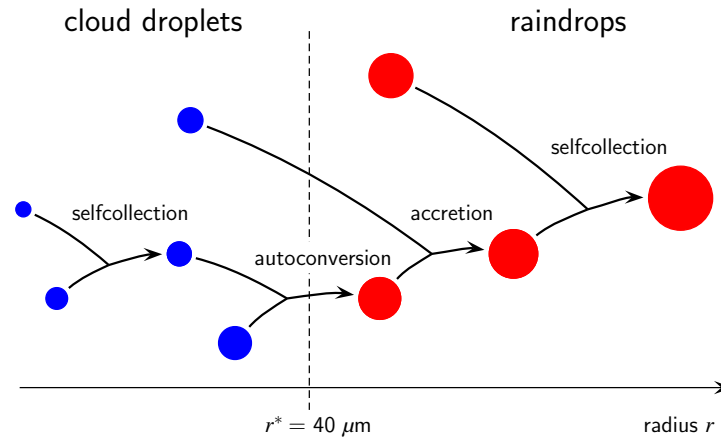


Figure 1.2.: Microphysical growth processes from the interaction of cloud droplets and raindrops (adapted from Seifert, 2002).

through drag force) and with each other (selfcollection, autoconversion and accretion, see Fig. 1.2). Therefore, a particle-based view point is the most natural approach when striving for an improved understanding of rain formation processes.

The fundamental problem of particle-fluid interactions in a turbulent environment is studied extensively in the field of fluid dynamics with numerical models and from experimental measurements. It reveals many important phenomena such as strong acceleration and intermittent velocities along Lagrangian trajectories (e.g., La Porta et al., 2001), statistics of Lagrangian velocity differences and particle dispersion (e.g., Bec et al., 2010; Mazzitelli et al., 2014a), or preferential concentration (e.g., Eaton and Fessler, 1994). A direct transfer of those results to cloud-droplet–fluid interactions and raindrop–fluid interactions is often hampered due to idealised experimental setups, e.g., the assumption of homogeneous, isotropic or stationary turbulence, massless, point-like, non-interacting particles, or the negligence of hydrodynamic interactions or gravity. In addition, such experiments cover regions in non-dimensional number space (spanned at least by the Stokes number and the non-dimensional terminal fall velocity) that often do not coincide with those found in a cloudy environment. Nevertheless, many fundamental results are applied and further advanced to cloud-droplet–fluid interactions (for reviews on this topic see, e.g., Vaillancourt and Yau, 2000; Shaw, 2003; Toschi and Bodenschatz, 2009; Devenish et al., 2012; Grabowski and Wang, 2013).

Methodologically, most Lagrangian studies in the atmospheric community either use massless particles as an analyses tool (e.g., Kogan, 2006; Heus et al., 2008; Yamaguchi and Randall, 2012) or simulate Lagrangian air parcels that include a bin microphysics scheme (e.g., Stevens et al., 1996a; Pinsky et al., 2008; Magaritz et al., 2009). Only recently, the super-droplet method was developed and became computationally affordable (Andrejczuk et al., 2008; 2010; Shima et al., 2009; Riechelmann et al., 2012). Embedded in an LES model, which provides the Eulerian flow dynamics, the super-droplet model

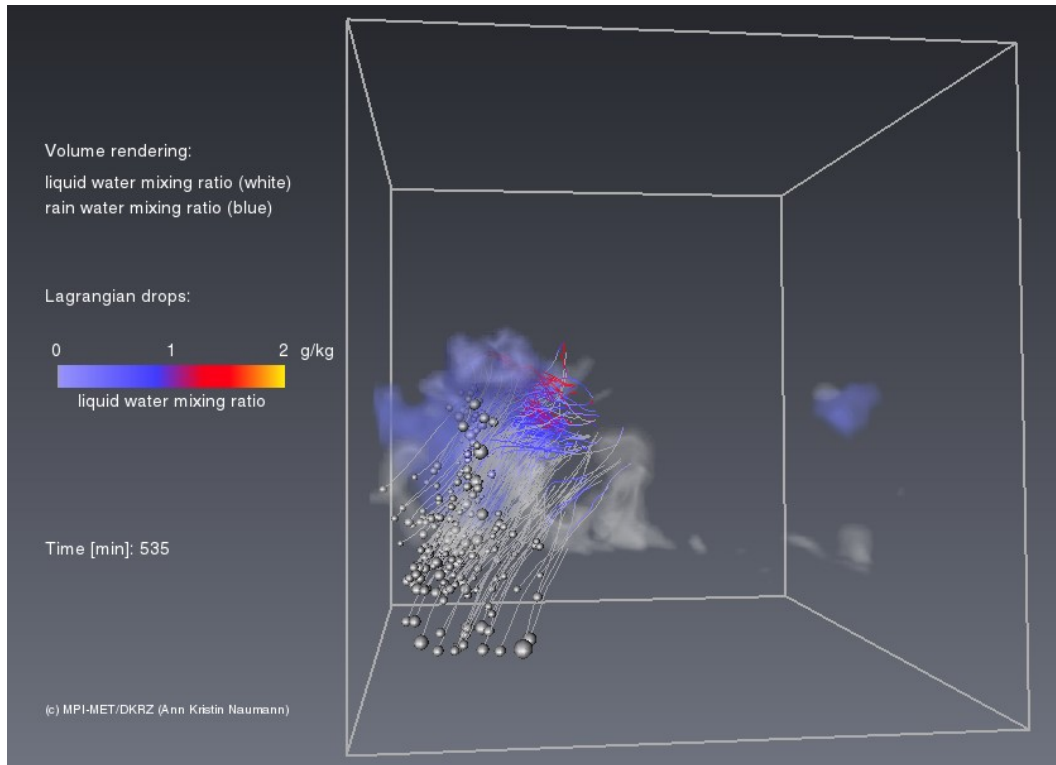


Figure 1.3.: Snapshot of a visualisation of Lagrangian Drops (LDs) in a cloud. Shown are only those LDs that eventually reach the surface in the course of the simulation. The size of an LD is proportional to the size of the raindrops they represent. The trajectories of the LDs are coloured by the ambient cloud liquid water. From the Eulerian model the cloud liquid water (white) and the rainwater (blue) are shown. The model domain is 3.2 km in all three spatial directions.

replaces the Eulerian microphysics parametrisation. The super-droplet model describes the cloud droplet and raindrop development from cloud droplet nucleation until the arrival of raindrops at the surface on a particle-based level and can therefore be used to study, e.g., the collision kernel or aerosol-cloud interactions. For computational reasons not each cloud droplet and each raindrop can be simulated, but one super-droplet represents a multiplicity of real drops of the same size. With such an approach it is possible to analyse rain formation on domains of a few kilometres and thus to simulate a full cloud on a particle-based level. However, because the vast majority of drops in a cloud are small cloud droplets, most of the computational power is spent on the cloud droplet phase and an adequate representation of the tail of the drop size distribution, which is decisive for precipitation characteristics, is challenging.

To investigate in particular the raindrop phase of warm rain formation, a Lagrangian drop (LD) model for simulating raindrops in LES is developed in Chapter 3. The LD model is related to the super-droplet method but solely focuses on the raindrop phase. Such a framework targets specifically the warm rain microphysical processes and explicitly includes all relevant processes for raindrop growth such as accretional growth from cloud

water, selfcollection among raindrops, evaporation and sedimentation, while the Eulerian LES model provides the time-dependent, thermodynamical background fields. In the current implementation of the LD model, the Eulerian LES model is run including the full bulk microphysics scheme and the raindrop phase is additionally simulated by the LD model but without any feedbacks on the Eulerian fields. A snapshot of a visualisation of LDs in a cloud is shown in Fig. 1.3. In Chapter 3, the LD model is developed and applied to simulate two isolated shallow cumulus clouds. In addition, a sensitivity study is performed to test whether the model is fit for purpose and to answer the following question:

How sensitive is the LD model to the representation of dynamical and microphysical processes and how do the uncertainties in the LD model compare to uncertainties in a bulk rain microphysics scheme?

1.4. Parametrisation of the raindrop size distribution

In addition to the subgrid-scale variability of the bulk fields (as described in Sect. 1.2), the microphysical process rates, which one seeks to parametrise, also depend on the raindrop size distribution (RSD). Although particle-based methods are a promising tool to represent cloud droplets and raindrops on small domains with high resolution, they are much too expensive for most applications. Instead bin or bulk microphysics parametrisation are used to describe the development of the RSD.

In bin schemes the RSD is discretised in each model grid box and the amount of rainwater in each size bin can evolve freely. Bin schemes are considerably more expensive than bulk schemes because the amount of rainwater has to be predicted for each bin. As a consequence bin schemes are usually not applied in NWP models or GCMs but are primarily used in microphysical process studies.

In contrast, bulk microphysics schemes predict the moments of the RSD. If the RSD is formulated as a function of the raindrop diameter, its zeroth moment equals the raindrop number density, its third moment is proportional to the rainwater mass density and its sixth moment is proportional to the radar reflectivity.

Determining the PDF that describes the subgrid-scale variability of bulk field variables (Sect. 1.2) and determining the RSD are related problems. Both distributions need to be described with a sufficient degree of accuracy that allows for a good representation of the derived quantity, i.e., the cloud fraction or the microphysical process rates. Therefore an appropriate functional form of the distribution, which has a number of free parameters, has to be chosen. These free parameters are related to the moments of the distribution and for each model grid box they are either predicted or diagnosed by closure equations.

In two-moment rain microphysical schemes, usually the moments of the RSD related to the number density and the rainwater mass density are predicted and the RSD is often

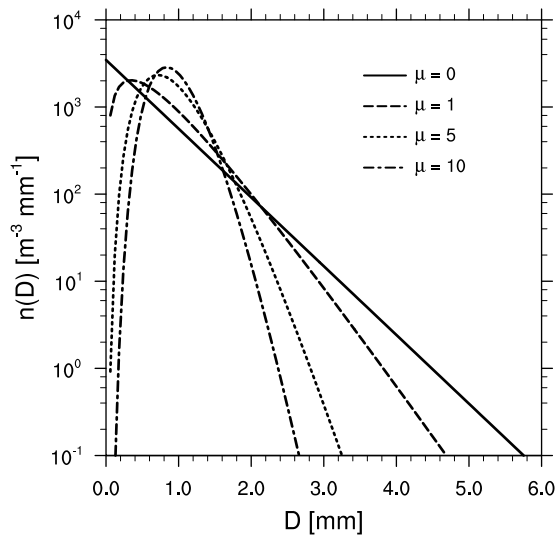


Figure 1.4.: Raindrop size distribution (RSD) following a gamma distribution, $n(D) = N_0 D^\mu e^{-\lambda D}$, for different shape parameters μ at a constant mean volume diameter of $\bar{D} = 1$ mm and rainwater content $L_r = 1$ g/m³. D is the raindrop diameter, N_0 the intercept parameter and λ the slope parameter (adapted from Seifert, 2008).

assumed to be well represented by a 3-parameter gamma distribution (Fig. 1.4). Thus, an additional closure equation has to be established, which typically relates the shape parameter of the gamma distribution to the mean raindrop diameter (Milbrandt and Yau, 2005; Seifert, 2008). However, modelling studies and analyses of observational data suggest that the relationship of the shape parameter to the mean raindrop diameter is quite variable (Munchak and Tokay, 2008; Seifert, 2008; Geoffroy et al., 2014). In Chapter 4 the development of the RSD in shallow cumulus is examined with the LD model and the following questions are investigated:

How does the RSD develop in the course of the lifecycle of a shallow cumulus cloud? Is the development of the shape of the RSD in shallow cumulus well represented in the closure equation of a two-moment bulk rain microphysics scheme?

1.5. A particle-based view on warm microphysics

Most microphysical process studies of warm rain formation focus on two related topics: the cloud droplet size distribution, which is observed to be considerably broader than simple, adiabatic models predict, and the condensation-coalescence bottleneck or the so-called size gap, i.e., the puzzling inconsistency between the observed rapid formation of precipitation in warm clouds and the theoretical understanding of slow cloud droplet growth at sizes between 10-30 μ m in radius, where neither condensation nor collision-coalescence is thought to be very effective (Simpson, 1941; Langmuir, 1948). Different

mechanisms are proposed to explain the broadening of the droplet size distribution and the fast onset of precipitation: entrainment and mixing (Brenguier and Grabowski, 1993; Lasher-Trapp et al., 2005; Cooper et al., 2013), giant cloud condensation nuclei (Yin et al., 2000; Lasher-Trapp et al., 2001), turbulence-enhanced condensation (Shaw et al., 1998; Grabowski and Vaillancourt, 1999; Sidin et al., 2009) and turbulence-enhanced collisions (Saffman and Turner, 1956; Ayala et al., 2008).

For turbulence-enhanced collisions four enhancement mechanisms are found to be important for the formation of raindrops (e.g., by Pinsky and Khain, 1997a;b; Falkovich et al., 2002; Pinsky and Khain, 2004; Pinsky et al., 2006; Wang et al., 2006; Falkovich and Pumir, 2007; Voßkuhle et al., 2014; Park and Lee, 2014): First, turbulent transport (or the sling effect) describes the change in relative velocity of a pair of droplets due to inertia. Turbulent transport especially enhances the collision rate of droplet pairs of similar size, which have very low collision rates for pure gravitational kernels. Second, in a turbulent flow inertial particles cluster in regions of low vorticity and high strain-rate. Compared to a homogeneous distribution of droplets this preferential concentration enhances the collision rates. Third, the changed flow field around a droplet modifies the collision efficiency, called the hydrodynamic interaction effect. Fourth, droplets in a turbulent flow preferentially stay in regions of downward motion, which increases their average settling velocity. In microphysics parametrisations those enhancement mechanisms have been incorporated by applying turbulent enhancement factors on the collision kernel (Franklin et al., 2007; Wang et al., 2008; Ayala et al., 2008). LES studies then use those turbulent kernels to study the effect of turbulent enhancement on the cloud scale and find that the time that it takes a cloud to develop first embryo raindrops is considerably reduced compared to a pure gravitational kernel (Seifert et al., 2010; Wyszogrodzki et al., 2013; Franklin, 2014).

Lateral entrainment and mixing of dry air into the cloud dilutes the cloud droplet population and evaporates cloud droplets completely or partly. In addition, cloud condensation nuclei are entrained into the cloud and can subsequently form new cloud droplets at different heights above cloud base. For cumulus congestus, Lasher-Trapp et al. (2005) find significant broadening of the droplet size distribution due to entrainment and mixing. This broadening is caused by a variability in supersaturation histories along droplet trajectories that arrive in a common point near cloud top. Using a Lagrangian microphysical parcel model, Lasher-Trapp et al. (2005) are able to simulate realistic widths and shapes of the droplet size distribution but their results are sensitive to the assumed nature of the mixing process (homogeneous mixing vs. inhomogeneous mixing). In a subsequent study Cooper et al. (2013) show that raindrop embryos from the broadened droplet spectrum are able to move into areas of high liquid water content, where they grow by collision-coalescence and are able to rapidly form at least a small amount of rain.

There is emerging agreement that for a fast onset of precipitation the enhancement of condensation by small-scale turbulence probably is much less effective than the enhance-

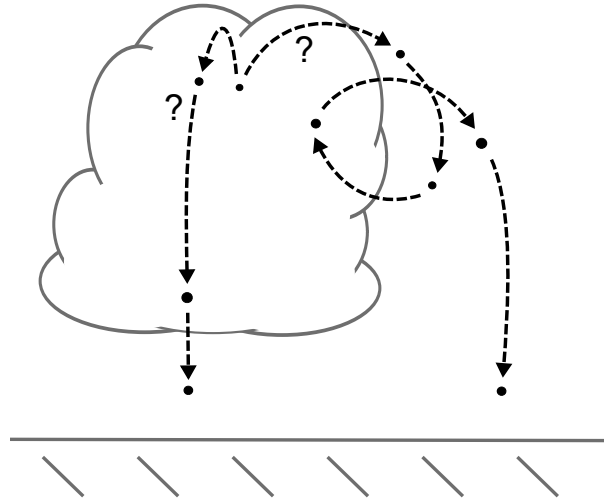


Figure 1.5.: Possible trajectories of raindrops in a shallow cumulus cloud. Raindrops typically emerge near cloud top but their subsequent growth history is less well known. Do raindrops fall straight through the cloud towards the surface or do some of them recirculate in the cloud layer?

ment of collision rates by small-scale turbulence, partly because condensational growth is a reversible process in contrast to the irreversible growth by collision-coalescence (Vailancourt and Yau, 2000; Shaw, 2003; Grabowski and Wang, 2013). For growth by condensation it is, however, hypothesised that small-scale turbulence is needed to allow cloud droplets to move from one large eddy to another, so-called *large-eddy hopping*. Cloud droplets originally located in the vicinity of a single point are able to hop between different large-eddies and are therefore exposed to different environments, resulting in different (condensational) growth histories, which broadens the observed droplet size distribution (Cooper, 1989; Lasher-Trapp et al., 2005; Bewley and Lasher-Trapp, 2011; Devenish et al., 2012; Grabowski and Wang, 2013).

Beyond the size gap, the role of small-scale turbulence and large eddies for the growth history of drizzle drops and raindrops is less well studied. For stratocumulus and for shallow cumulus it has been found that a sufficiently long in-cloud residence time and favourable cloud water conditions are needed for an embryo raindrop to grow large and to be able to reach the surface (Stevens et al., 1996a; Feingold et al., 1996; Kogan, 2006; Pinsky et al., 2008; Magaritz et al., 2009; Cooper et al., 2013). Furthermore, raindrop growth by collision-coalescence exhibits a stochastic nature, i.e., from a population of raindrops some raindrops grow considerably faster than the population grows on average (Telford, 1955; Gillespie, 1975). For instance, Kostinski and Shaw (2005) show that the fastest of a million drops grows about 10 times faster than the average drop. Those statistically fortunate drops will then collect smaller drops and initiate further growth. This is in line with the conception that autoconversion is needed to trigger precipitation, but that accretional growth becomes more important compared to autoconversion for

increasing precipitation rates (Gerber et al., 2008; Stevens and Seifert, 2008; Feingold et al., 2013).

So far the effect of large-eddy hopping and the resulting variability in growth histories has only been discussed for (condensational) cloud droplet growth. It is still unclear whether large-eddy hopping is a common feature of raindrop trajectories and whether it has a significant effect on accretional growth and selfcollection. Therefore, Chapter 5 analyses the growth histories of LDs in a field of shallow cumulus and in particular addresses the following question:

Is recirculation and updraft hopping of raindrops common in shallow cumulus (Fig. 1.5) and how much do recirculating raindrops contribute to surface precipitation?

CHAPTER 2

A REFINED STATISTICAL CLOUD CLOSURE USING DOUBLE-GAUSSIAN PROBABILITY DENSITY FUNCTIONS¹

Ich versuche mir die Welt zu erklären,
als ob zwischen Punkten Linien wären.

(Wir sind Helden)

In this chapter, a probability density function (PDF)-based scheme to parametrise cloud fraction, average liquid water and liquid water flux in large-scale models is introduced. The scheme is developed from and tested against Large-Eddy Simulations and observational data. Because the tails of the PDFs are crucial for an appropriate parametrisation of cloud properties, we use a double-Gaussian distribution, which is able to represent the observed, skewed PDFs properly. Introducing two closure equations, the resulting parametrisation relies on the first three moments of the subgrid variability of temperature and moisture as input parameters. The parametrisation is found to be superior to a single-Gaussian approach in diagnosing the cloud fraction and average liquid water profiles. A priori testing also suggests improved accuracy compared to existing double-Gaussian closures.

¹This chapter has been published with minor modifications as: Naumann, A. K., A. Seifert and J. P. Melado (2013): A refined statistical cloud closure using double-Gaussian probability density functions. *Geosci. Model Dev.*, **6**, 1641–1657, doi:10.5194/gmd-6-1641-2013.

Furthermore, we find that the error of the new parametrisation is smallest for a horizontal resolution of about 5–20 km and also depends on the appearance of mesoscale structures that are accompanied by higher rain rates. In combination with simple autoconversion schemes that only depend on the liquid water, the error introduced by the new parametrisation is orders of magnitude smaller than the difference between various autoconversion schemes. For the liquid water flux, we introduce a parametrisation that is depending on the skewness of the subgrid variability of temperature and moisture and that reproduces the profiles of the liquid water flux well.

2.1. Introduction

The cloud fraction and the average liquid water in a given volume depend on the variability of temperature and moisture within that volume. If subgrid variability is not taken into account at all, the grid volume is either entirely subsaturated or entirely saturated. To overcome this problem, diagnostic relative humidity schemes have been developed, e.g., by Smagorinsky (1960) and Sundqvist et al. (1989) who parametrised partial cloud fraction as a function of relative humidity with a certain critical relative humidity at which a partial cloud cover first appears. This kind of parametrisation has been developed further by implementing secondary predictors like condensate content (e.g., Xu and Randall, 1996) or vertical velocity (e.g., Slingo, 1987).

Another approach in diagnosing cloud fraction is based on one-dimensional PDFs of the subgrid variability in temperature and moisture². Assuming a single-Gaussian PDF, these schemes go back to Sommeria and Deardorff (1977) and Mellor (1977) and need not only the grid-box mean temperature and moisture but also the standard deviations as input parameters. Because the success of such schemes crucially depends on the ability to quantify the tails of the distribution (Bougeault, 1982b), further studies additionally took into account the skewness of the distribution, which lead to the use of, e.g., double-Gaussian (Lewellen and Yoh, 1993; Larson et al., 2001a), Gamma (Bougeault, 1982a) or Beta (Tompkins, 2002) distributions. Perraud et al. (2011) tested several of this distributions against model data and found that the double-Gaussian distribution gives best results.

Compared to relative humidity schemes, PDF-based schemes typically need more and higher moments as input parameters. While the first two moments are commonly available in NWP models and GCMs, there are ongoing efforts to develop higher-order closure boundary layer models, which include an estimate of the third moment, i.e., the skewness (Gryanik and Hartmann, 2002; Gryanik et al., 2005; Mironov, 2009; Machulskaya

²Assuming a uniform PDF of the total water subgrid-scale variability and the variance as a constant fraction of the saturation value, it has been shown (e.g., by Quaas, 2012), that the Sundqvist et al. (1989) relative humidity scheme is a special case of PDF-based schemes.

and Mironov, 2013). Apart from this disadvantage, PDF schemes have several advantages over relative humidity schemes. In PDF schemes, the shape of the PDF is parametrised but the variables aimed for, such as cloud fraction and average liquid water, are derived directly from this PDF. Therefore, the variables are calculated consistently from the assumed PDF. Also, numerical models that ignore subgrid variability are known to encounter systematic errors in cloud and radiative properties (Pincus and Klein, 2000; Rotstayn, 2000; Larson et al., 2001b). To tackle this issue, the knowledge of the subgrid PDF is essential. Furthermore, PDF schemes can potentially be used in a wide range of cloud regimes. Other than for relative humidity schemes, no trigger functions to switch from one regime (and its according parametrisation) to another regime are needed and artificial distinctions can be avoided.

As a further development from one-dimensional PDFs, joint PDFs have been introduced recently (e.g., by Larson et al., 2002). In joint-PDF schemes the variability of temperature and moisture are usually not summarised in one variable and the distribution of the vertical velocity can be added as further input. Because the vertical velocity is taken into account, the liquid water flux can be derived consistently from the joint PDF. This advantage has to be paid for by the prediction or diagnosis of several more moments and correlations among temperature, humidity and vertical velocity (e.g., Larson et al., 2002, used 19 parameters instead of 5 for a double-Gaussian distribution). Hence joint-PDF schemes are much more computational expensive than one-dimensional PDF schemes, but it is not clear yet if the potential benefits of a joint-PDF scheme justify the additional computational cost (Bogenschutz et al., 2013).

We therefore step back to one-dimensional PDF schemes and focus on improving the double-Gaussian PDF scheme to diagnose subgrid cloud fraction and average liquid water. The formulation follows Larson et al. (2001a) and is developed from and tested against Large-Eddy Simulations (LES) as well as aircraft measurements. In Sect. 2.2, the LES model, the case studies the model is applied to and the observational data set are described. The use and construction of a double-Gaussian PDF, the refined closure equations and the parametrisation of the liquid water flux are introduced in Sect. 2.3. Next, in Sect. 2.4, we perform a priori testing of the new cloud closure with LES data as input to examine the parametrisation's behaviour under idealised conditions, i.e., excluding the interplay with other model components as would be done with a posteriori testing in an NWP model or a GCM. In the following Sects. 2.5 and 2.6, the error dependence of the parametrisation on domain size and the role of mesoscale structures are discussed and the introduced cloud closure is extended to the diagnosis of the autoconversion rate. Finally, in Sect. 2.7, we give some concluding remarks.

Table 2.1.: Overview of the different LES cases used in this chapter. The four cases on the left hand side are used to develop (DYCOMS and RICO) and test (ARM and ASTEX) the parametrisations introduced in this chapter. The three cases on the right hand side are solely used in the Sect. 2.5.

	ARM	ASTEX	DYCOMS	RICO	RICO		
				standard	standard	moist	moist
nx	256	256	512	512	1024	1024	2048
L	12.8 km	10.2 km	10.2 km	20.5 km	25.6 km	25.6 km	51.2 km
H	5.1 km	3.2 km	1.4 km	4.0 km	4.0 km	4.0 km	4.0 km
Δx	50 m	40 m	20 m	40 m	25 m	25 m	25 m
Δz	40 m	20 m	5–52 m	20 m	25 m	25 m	25 m
t	15 h	42 h	5 h	36 h	30 h	30 h	30 h

nx : number of grid points in each horizontal direction, L : horizontal domain size, H : vertical domain size, Δx : horizontal resolution, Δz : vertical resolution, t : length of simulation.

The ARM simulation has been performed by Thijs Heus. The DYCOMS simulation and the RICO simulations have been performed by Axel Seifert.

2.2. Model and data

2.2.1. Large-Eddy Simulations

The LES model used in this thesis is the University of California, Los Angeles LES (UCLA-LES; Stevens et al., 2005a; Stevens, 2007) with one major difference to previous work, that is, the time stepping is done with a third-order Runge–Kutta scheme instead of the former leapfrog scheme. Prognostic equations for each of the following variables are solved: the three components of the velocity, the total water mixing ratio, the liquid water potential temperature, the mass mixing ratio of rainwater and the mass specific number of rainwater drops. Considering only warm clouds, we use the double-moment bulk microphysical scheme from Seifert and Beheng (2001). Subgrid fluxes are modelled with the Smagorinsky–Lilly model.

In this chapter, we adapt the UCLA-LES to four different case studies, which span over a range of different cloud regimes. Shallow cumulus over ocean (RICO³; see Rauber et al., 2007) and over land (ARM⁴; see Brown et al., 2002) are considered as well as stratocumulus (DYCOMS⁵; see Stevens et al., 2003) and the transition from stratocumulus to cumulus (ASTEX⁶; see Albrecht et al., 1995). Domain sizes and resolutions of the different LES cases are given in Table 2.1.

³Rain in cumulus over the ocean

⁴Atmospheric radiation measurement

⁵Dynamics and chemistry of marine stratocumulus

⁶Atlantic stratocumulus transition experiment

ARM

The LES setup of the ARM case follows that of the sixth intercomparison project, performed as part of the GCSS⁷ program and described by Brown et al. (2002).

ASTEX

The setup of the LES study for the ASTEX case is similar to that proposed by the Euclipse ASTEX Lagrangian model intercomparison case (Dussen et al., 2013). The initial profiles are identical to the first GCSS ASTEX “A209” modelling intercomparison case and the model is forced by time-varying sea surface temperature and divergence taken from Bretherton et al. (1999).

DYCOMS

For the LES setup of DYCOMS, we follow the DYCOMS-II RF01 setup of the eighth case study conducted under the auspices of the GCSS boundary layer cloud working group and described by Stevens et al. (2005a).

RICO

The initial data and the large-scale forcing for the standard RICO simulations are based on the precipitating shallow cumulus case that was constructed by the GCSS boundary layer working group and described by van Zanten et al. (2011). A modified moister version, which differs from the standard setup only by a moister initial profile, was first used by Stevens and Seifert (2008), to which we refer for a detailed setup of the case. The moister initial condition leads to higher rain rates compared to the standard case and subsequently to mesoscale organization of the cloud field due to the formation of cold pools mainly caused by evaporation of rain in the subcloud layer (Seifert and Heus, 2013).

Unless stated otherwise, we refer to our standard RICO setup with $nx = 512$ when analysing LES data from the RICO case. The three RICO cases on the right hand side in Table 2.1 are equal to the LES runs R01, M01 and M01^{big} of Seifert and Heus (2013). For this thesis they are solely used in Sect. 2.5 when discussing the error dependence on domain size and the role of mesoscale structures.

2.2.2. Observational data

To be able to test our parametrisation against observational data, we use RICO field campaign data (Rauber et al., 2007). This data set includes airborne measurements obtained from the NSF/NCAR Research Aviation Facility C-130Q Hercules aircraft (Tail Number N130AR) at 25 Hz. Besides the static pressure and the ambient temperature, the water

⁷GEWEX (Global Energy and Water Experiment) Cloud system studies

vapour mixing ratio measured with a Lyman-alpha hygrometer as well as the liquid water content measured with a Gerber PV-100 probe are used in this chapter. Because the temperature sensor is susceptible to wetting during cloud penetrations, periods of cloud presence are defined by a threshold value of 10 cloud droplets (3 to 45 μm diameters) per cm^3 and in-cloud temperature is measured by a radiometric temperature sensor that is not sensitive to wetting. In 17 research flights (RF01 to RF13 and RF16 to RF19) all available five-minutes intervals at moderate height (pressure > 600 hPa) and with relatively constant pressure (standard deviation < 1 hPa) were selected and analysed. (Note that, unfortunately, during research flight 14 and 15 the Lyman-alpha hygrometer was out of service, so no analysis of these flights is possible.)

2.3. Introducing a refined cloud closure

2.3.1. Data analysis: the double-Gaussian PDF

For diagnosing the cloud fraction and the average liquid water, Perraud et al. (2011) show that the temperature variability should not be neglected relative to the humidity variability. We therefore follow Sommeria and Deardorff (1977), Mellor (1977) and Lewellen and Yoh (1993) and define the extended liquid water mixing ratio, $s(q_t, T_1)$, by

$$s = \frac{q_t - q_s(T_1)}{1 + \frac{L}{c_p} \left(\frac{\partial q_s}{\partial T} \right)_{T=T_1}}, \quad (2.1)$$

where q_t is the total water mixing ratio, $q_s(T_1)$ is the saturation mixing ratio at a given value of the liquid water temperature $T_1 = \theta_1 T / \theta$ and $(\partial q_s / \partial T)_{T=T_1} = L q_s(T_1) / (R_v T_1^2)$ is the slope of the saturation mixing ratio at $T = T_1$. Furthermore, T is the temperature, θ the potential temperature, θ_1 the liquid water potential temperature, L the latent heat of vapourisation, c_p the specific heat at constant pressure and R_v the gas constant for water vapour. The extended liquid water mixing ratio takes into account the temperature variability as well as the humidity variability and is a measure of subsaturation if s is negative. For $s > 0$, s is approximately equal to the liquid water mixing ratio, q_l . Note that the ratio of the mean of s , \bar{s} , to the standard deviation of s , σ , can be approximated by the normalised saturation deficit, Q_1 , which is defined as the bulk value of s , $s_{\text{bu}} = s(\bar{q}_t, \bar{T}_1)$, divided by σ (Lewellen and Yoh, 1993, ζ therein).

If the PDF of s is known for each grid box in an NWP model or a GCM, the cloud fraction and the average liquid water can be calculated by integration over the PDF of s (see Eqs. 2.8 and 2.9 for the formulation of the integral). As this is not the case, and only the first moments of the PDF of s can usually be predicted in large-scale models, we are using high-resolution LES and observational data to investigate the behaviour of the distribution of s on the subgrid scale of an NWP model or a GCM.

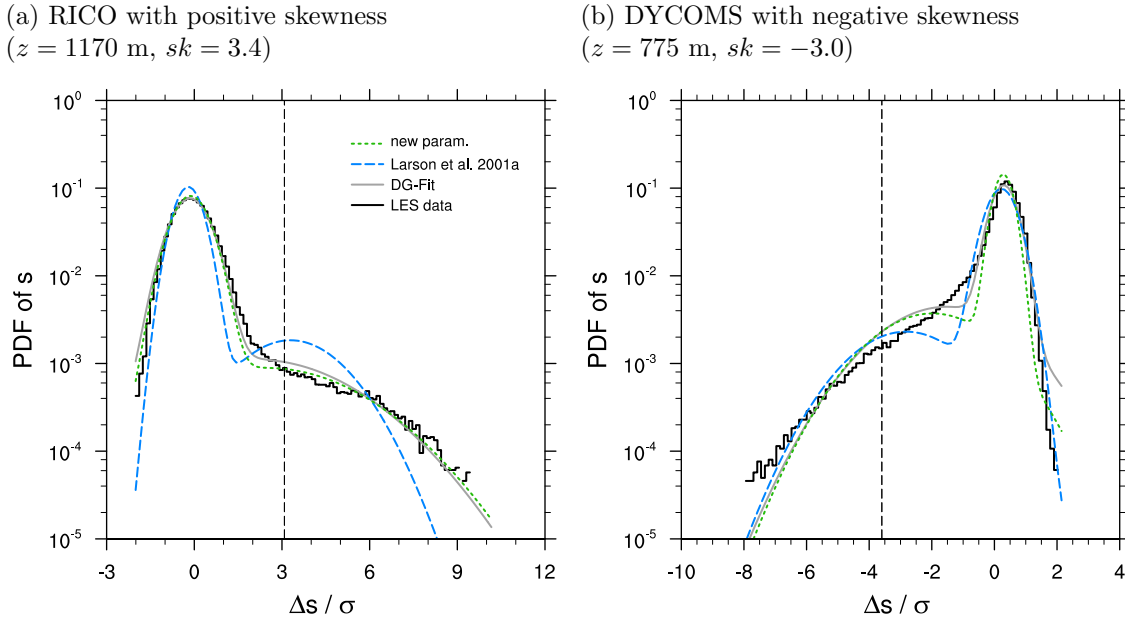


Figure 2.1.: PDF of s for a specific height in the cloud layer. Furthermore, the corresponding best skewness-retaining double-Gaussian fit (DG-Fit) and the resulting PDF when using the closure equations from Larson et al. (2001a) (Eq. 2.3) and the introduced closure equations (Eq. 2.4) are shown. It is $\Delta s = s - \bar{s}$. The black, dashed line indicates the saturation value ($s=0$).

Considering the distribution of s from each model level in the LES data over the whole domain, we find that the PDF of s can be highly skewed in the cloud layer with positive skewness for shallow cumulus and negative skewness for stratocumulus (Fig. 2.1). For shallow cumulus, cloud formation is driven by surface heat fluxes that initiate few but strong updrafts in a slowly descending environment. Therefore the PDF of s is positively skewed with the moist tail representing the (cloudy) updrafts. In contrast, stratocumulus is driven by radiative and evaporative cooling at cloud top. Hence non-cloudy downdrafts emerge in a dry tail of the PDF of s and the PDF tends to be skewed negatively (Helfand and Kalnay, 1983; Moeng and Rotunno, 1990). Consequently for both the shallow cumulus regime and the stratocumulus regime, the success of a scheme diagnosing the cloud fraction and the average liquid water depends crucially on its ability to quantify the tail of the distribution.

Following Larson et al. (2001a), we choose to represent the PDF of s by a double-Gaussian distribution, which can represent skewed distributions and is able to reproduce the tail. The double-Gaussian distribution is quite popular (Larson et al., 2001a; Perraud et al., 2011) because the two single-Gaussian distributions that the double-Gaussian distribution is composed of can be interpreted physically as the updrafts and their slowly descending environment in case of a cumulus regime (Neggers et al., 2009) or as the downdrafts and their well-mixed environment in the case of a stratocumulus regime. In both regimes the dominant mode of the PDF of s is associated with the well-mixed environ-

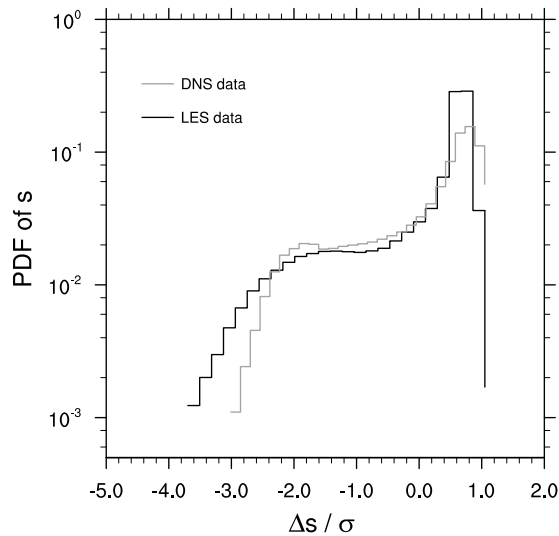


Figure 2.2.: PDF of s from LES data of DYCOMS and from a DNS study by Mellado et al. (2010). Both PDFs are calculated at a height level close to the cloud top where the variance of horizontal winds are at their respective maximum. The DNS data corresponds to a local study of turbulent mixing at cloud top, due solely to evaporative cooling.

ment and assumed to be Gaussian distributed. The tail of the PDF is represented in a secondary mode and is associated with the thermal updrafts in shallow cumulus and the negatively buoyant downdrafts in stratocumulus (Fig. 2.1). This secondary mode is also assumed to be Gaussian distributed.

The choice of the double-Gaussian PDF is further supported by direct numerical simulations (DNS) of an evaporatively driven cloud top, where scales between a few millimetres and a few metres are resolved (Mellado et al., 2010). Consistently with the physical interpretation in terms of the large-scale updraft and downdraft flow structure presented above, agreement between the LES and the DNS data (Fig. 2.2) indicates that the non-Gaussianity is quite insensitive to the details of the small scales, since DNS resolves them and LES parametrises them. Therefore, the skewed shape of the PDF seems to be related to the fact that buoyancy is one of the main forcing mechanisms, which is often the case when clouds are present in the system.

Using a double-Gaussian distribution, the PDF of s is written as

$$\begin{aligned}
 P(s) &= aP_1(s) + (1-a)P_2(s) \\
 &= \frac{a}{\sqrt{2\pi}\sigma_1} \exp\left(-\frac{1}{2}\left(\frac{s-s_1}{\sigma_1}\right)^2\right) + \frac{1-a}{\sqrt{2\pi}\sigma_2} \exp\left(-\frac{1}{2}\left(\frac{s-s_2}{\sigma_2}\right)^2\right), \quad (2.2)
 \end{aligned}$$

where P_1 and P_2 are single-Gaussian distributions and s_1 , s_2 , σ_1 and σ_2 are the mean and the standard deviation of the two single-Gaussian distributions. The relative weights a and $(1-a)$ can be interpreted as the corresponding area fractions (see Appendix A). By convention and without loss of generality, we choose $s_1 > s_2$. With five parameters to

determine the PDF, the double-Gaussian distribution is highly flexible on the one hand. On the other hand, operational NWP models or GCMs are not able to predict five moments of the distribution of s . Therefore closure assumptions will have to be chosen carefully (see Sect. 2.3.2).

In order to be able to analyse the LES data and the observational data in terms of the closure equations, we next aim to find the best fit of a double-Gaussian distribution to the PDF of s for each level of our LES data set and each five-minute interval in the observational data set. Because the skewness of the distribution is a crucial parameter in our closure, we establish an additional constraint for the fit, which retains the skewness of the given PDF for the fitted double-Gaussian distribution. Instead of varying the five parameters of the double-Gaussian distribution (a , s_1 , s_2 , σ_1 , σ_2) like Larson et al. (2001a) did, we express s_1 as a function of a , s_2 , σ_1 , σ_2 and the mean, the standard deviation and the skewness of the given PDF, \bar{s} , σ and sk , using the definition of the third standardised moment of a double-Gaussian distribution: $sk = a \left(3 \left(\frac{s_1 - \bar{s}}{\sigma} \right) \left(\frac{\sigma_1}{\sigma} \right)^2 + \left(\frac{s_1 - \bar{s}}{\sigma} \right)^3 \right) + (1 - a) \left(3 \left(\frac{s_2 - \bar{s}}{\sigma} \right) \left(\frac{\sigma_2}{\sigma} \right)^2 + \left(\frac{s_2 - \bar{s}}{\sigma} \right)^3 \right)$ (Lewellen and Yoh, 1993; Larson et al., 2001a).

The values of \bar{s} , σ and sk are obtained from the LES data or the observational data to evaluate the above equation and hence four parameters are left to be fitted (a , s_2 , σ_1 , σ_2). To calculate the best skewness-retaining fit for each level of the LES data and each five-minute interval in the observational data set, we first do χ^2 -tests in the relevant region of the parameter space. Because this procedure gets computationally expensive easily (at least if four parameters are to be fitted like it is done here), we only search for a coarse estimation of the best fit for the four parameters and then use this best fit as input for the Nelder–Mead downhill simplex method (Press et al., 1992) to find the actual minimum. In Fig. 2.1 two examples of the distribution of s in a cloud layer of the LES data, one with positive skewness and one with negative skewness, are shown together with their best skewness-retaining double-Gaussian fit.

2.3.2. Closure equations considering the regime dependent cloud structures

Even if we assume that the first three moments of the PDF of s are readily available from an NWP model or a GCM, e.g., from a higher-order closure boundary layer model, the number of parameters has to be reduced from five to three, i.e., two closure equations are necessary. Larson et al. (2001a) suggested

$$\frac{\sigma_1}{\sigma} = 1 + \gamma \frac{sk}{\sqrt{\alpha + sk^2}}, \quad \frac{\sigma_2}{\sigma} = 1 - \gamma \frac{sk}{\sqrt{\alpha + sk^2}} \quad (2.3)$$

with $\alpha = 2.0$ and $\gamma = 0.6$ and $s_1 > s_2$ by convention.

Analysing the different LES cases by fitting a double-Gaussian distribution to the (normalised) PDF of s for each vertical level as described in Sect. 2.3.1, we obtain σ_1/σ and

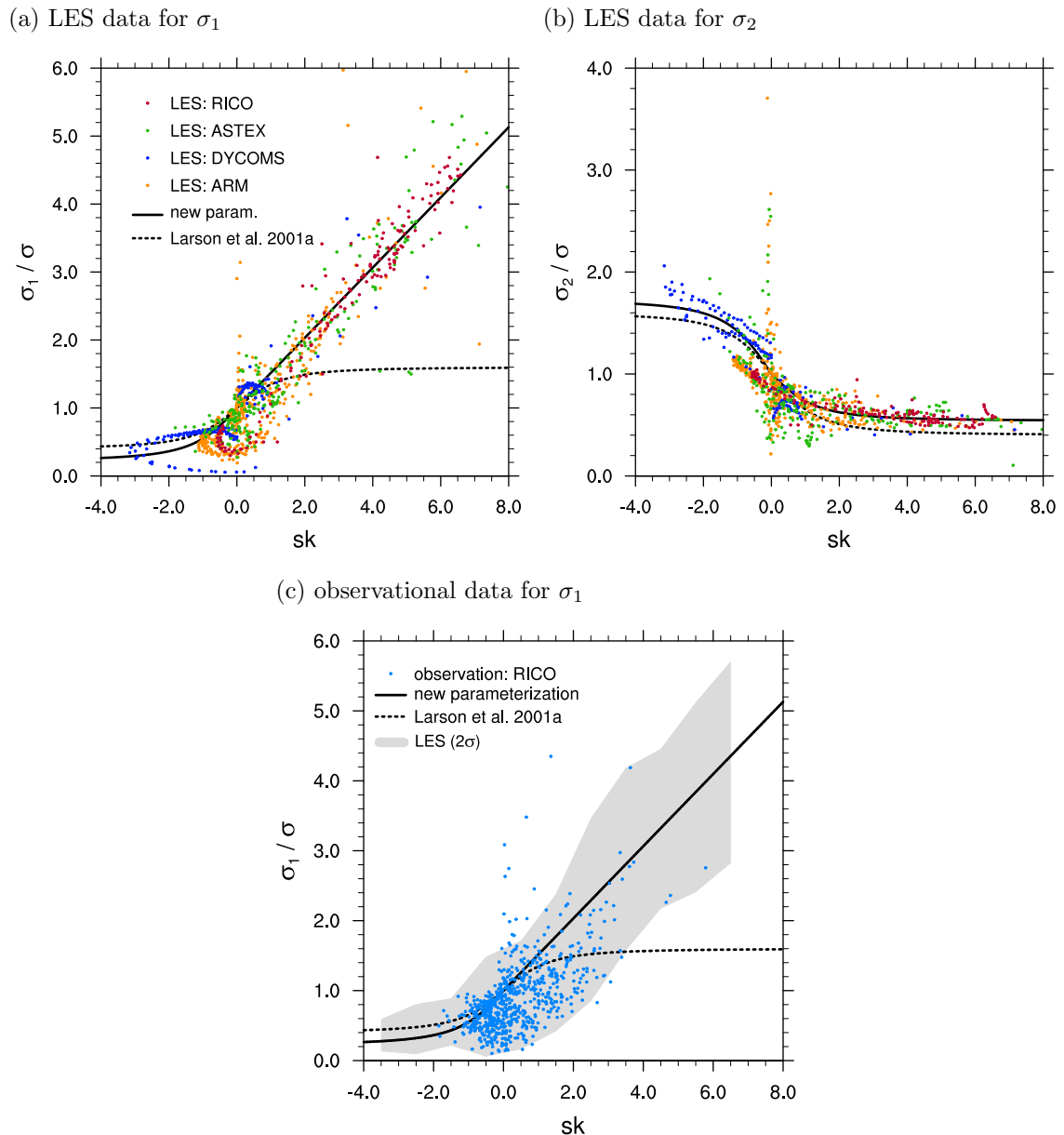


Figure 2.3.: LES data of ARM, ASTEX, RICO and DYCOMS and observational data from the RICO campaign along with the closure equations from Larson et al. (2001a) (dashed line) and the new closure equations (solid line). Note that the new closure equations are fitted to the LES data of RICO and DYCOMS rather than to all available case studies. The grey shading in (c) corresponds to two times the standard deviation from the four LES cases in (a). The legend in (a) also applies to b.

σ_2/σ and plot them as a function of sk (Fig. 2.3 a and b). It is noted that high σ_1/σ or σ_2/σ values (> 1.5) at $sk = 0$ are an artifact of a double-Gaussian distribution being fitted to a distribution that is not skewed. In this case a single-Gaussian distribution might represent the given distribution well. So if a approaches 0.0 (or 1.0) during the fitting procedure, the second (or first) single-Gaussian distribution of the double-Gaussian distri-

bution might fit the given distribution so well that the termination criteria for the fitting procedure is reached, independent of the shape of the first (or second) single-Gaussian distribution, which is essentially irrelevant because of its small amplitude. Therefore, for $sk = 0$ particularly high or low values of σ_1/σ or σ_2/σ can be ignored, when evaluating the closure equations.

Because we defined $s_1 > s_2$, large values for σ_1/σ represent the cloudy tail in shallow cumulus, where sk has high positive values. In stratocumulus, where the skewness is negative, large values for σ_2/σ represent the non-cloudy part of the cloud layer. Larson et al. (2001a) analysed observational data from the ASTEX campaign and found only very few measurements of high positive skewness. They therefore suggested an antisymmetric behaviour for σ_1/σ and σ_2/σ depending on sk (Fig. 2.3 a and b). In contrast, we find from the different LES case studies that in the cumulus regime σ_1/σ has higher values than σ_2/σ in the stratocumulus regime.

This broken antisymmetric behaviour is consistent with the physical understanding that cloudy updrafts in shallow cumulus are more vigorous than non-cloudy downdrafts in stratocumulus. For the shallow cumulus cloud cores the upper limit is a moist adiabatic ascent, while the stratocumulus downdrafts are only initially cloudy and as soon as they become cloud-free follow a dry adiabatic descent. Because the downdrafts are not exactly the reversed process of the updrafts, the tails of the PDFs of s are different for both cloud regimes, that is, the tails are heavier in the cumulus regime than in the stratocumulus regime.

Using the $s_1 > s_2$ convention, we suggest a refinement of the parametrisation of Larson et al. (2001a) using a modified set of closure equations (Fig. 2.3 a and b)

$$\frac{\sigma_1}{\sigma} = \begin{cases} 1 + \gamma_1 \frac{sk}{\sqrt{\alpha}} & \text{if } sk > 0 \\ 1 + \gamma_3 \frac{sk}{\sqrt{\alpha + sk^2}} & \text{if } sk \leq 0 \end{cases} \quad (2.4)$$

$$\frac{\sigma_2}{\sigma} = \begin{cases} 1 - \gamma_2 \frac{sk}{\sqrt{\alpha + sk^2}} & \text{if } sk > 0 \\ 1 - \gamma_4 \frac{sk}{\sqrt{\alpha + sk^2}} & \text{if } sk \leq 0 \end{cases}$$

with $\alpha = 2.0$ adopted from Larson et al. (2001a). Fitting the parameters γ_n with a simple least square fit to the LES data sets of DYCOMS and RICO, we find best agreement for $\gamma_1 = 0.73$, $\gamma_2 = 0.46$, $\gamma_3 = 0.78$ and $\gamma_4 = 0.73$. By fitting the closure equations to only the two data sets of DYCOMS and RICO, which cover the stratocumulus and the cumulus type cloud regime, respectively, the LES data sets of ASTEX and ARM remain as independent test data sets. This generic division in training and test data aims to permit a later comparison between the error of this new parametrisations and other parametrisations from the literature (see Sect. 2.4). The main difference between this set of closure equations and the one from Larson et al. (2001a) is the dependence of σ_1/σ on

sk for (large) positive values of skewness, i.e., for the shallow cumulus regime.

The new parametrisation is also supported by observational aircraft data from the RICO campaign (Fig. 2.3 c). Compared to the simulated RICO case, the skewness from the observational data does not reach values as high as the skewness from the LES. This might be due to the sampling strategy of the observational data with the aircraft. The RICO project was targeting for early stage growing shallow cumulus towers from initiation to early rain formation. The statistics for the observational data set is therefore biased toward those types of clouds and away from fully developed, later stage clouds (A. Schanot, personal communication, 2012) while with LES all stages of the life cycle of such clouds are simulated. Therefore in the observational data regions with particularly high s are undersampled. Nevertheless, the few data points with high skewness obtained from observational data of the RICO campaign fit well into the range of values found from LES and align rather with the introduced closure equations than with the ones from Larson et al. (2001a).

A difficulty in the parametrisation of Larson et al. (2001a) as well as in the new parametrisation is the treatment of distributions that are characterised by $sk \approx 0$. Both sets of closure equations are constructed such that at $sk = 0$ the normalised standard deviations $\sigma_1/\sigma = \sigma_2/\sigma = 1$, i.e., for the closure equations the double-Gaussian distribution collapses to a single-Gaussian distribution as the skewness vanishes. In the LES data in the range of $sk \approx 0$, distributions that match a single-Gaussian distribution occur as well as bimodal double-Gaussian distributions, where the two modes balance in a way that the skewness almost vanishes (Fig. 2.4). The latter distributions often appear in the cumulus regimes at cloud base and are characterised by $\sigma_1/\sigma \approx \sigma_2/\sigma < 1$ (Fig. 2.3). Though the bimodal distributions with zero skewness cannot be captured adequately by the closure equations, the induced error is relatively small and will be discussed again in Sect. 2.4.

Knowing the first three moments of the distribution of s for a certain model level, σ_1 and σ_2 can now be calculated via the closure equations (Eq. 2.4), while a , s_1 and s_2 are obtained from the definition of the first three moments of a double-Gaussian distribution (Larson et al., 2001a, Eqs. 22–24 therein):

$$sk = \left[a(1-a) \left(1 - a \left(\frac{\sigma_1}{\sigma} \right)^2 - (1-a) \left(\frac{\sigma_2}{\sigma} \right)^2 \right) \right]^{\frac{1}{2}} \left[3 \left(\frac{\sigma_1}{\sigma} \right)^2 - 3 \left(\frac{\sigma_2}{\sigma} \right)^2 + \frac{1-2a}{a(1-a)} \left(1 - a \left(\frac{\sigma_1}{\sigma} \right)^2 - (1-a) \left(\frac{\sigma_2}{\sigma} \right)^2 \right) \right] = 0 \quad (2.5)$$

$$\frac{s_1 - \bar{s}}{\sigma} = \left(\frac{1-a}{a} \right)^{\frac{1}{2}} \left(1 - a \left(\frac{\sigma_1}{\sigma} \right)^2 - (1-a) \left(\frac{\sigma_2}{\sigma} \right)^2 \right)^{\frac{1}{2}} \quad (2.6)$$

$$\frac{s_2 - \bar{s}}{\sigma} = - \left(\frac{a}{1-a} \right)^{\frac{1}{2}} \left(1 - a \left(\frac{\sigma_1}{\sigma} \right)^2 - (1-a) \left(\frac{\sigma_2}{\sigma} \right)^2 \right)^{\frac{1}{2}} \quad (2.7)$$

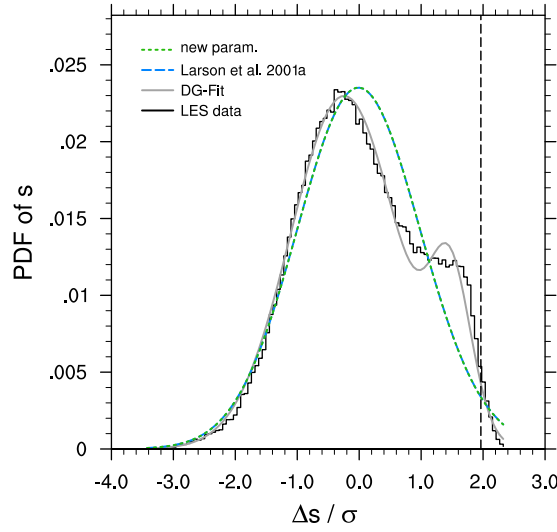


Figure 2.4.: Bimodal PDF of s from the RICO case at cloud base with $sk = 0.04$. While the LES data shows a bimodal distribution and the double-Gaussian fit is able to capture this shape, the two parametrisations coincide in assuming a single-Gaussian distribution for vanishing skewness. For further explanation of the legend see Fig. 2.1.

where Eq. 2.5 may be solved numerically for a . Alternatively, to avoid an iterative solution for a more computational efficient implementation in a GCM or an NWP model, an (e.g., polynomial or matched asymptotics) approximation of a as a function of sk can be used. For the present analysis however, we solve for a numerically using a simple bisection method with an accuracy of 10^{-6} , which typically took about 30 iterations.

Comparing the parametrised distribution of s to the original LES data in all four case studies (Fig. 2.1, ASTEX and ARM not shown), we find that the new parametrisation is able to represent the differences in the distribution of s in a shallow cumulus regime as well as a stratocumulus regime and therefore represents the tails in a shallow cumulus regime better than the parametrisation by Larson et al. (2001a).

Having determined a double-Gaussian PDF of s , the cloud fraction, C , and the average liquid water of a large-scale grid box, \bar{q}_l , are found by integration:

$$\begin{aligned} C &= \int_0^{\infty} P(s) ds \\ &= \frac{a}{2} \left(1 + \operatorname{erf} \left(\frac{s_1}{\sqrt{2}\sigma_1} \right) \right) + \frac{1-a}{2} \left(1 + \operatorname{erf} \left(\frac{s_2}{\sqrt{2}\sigma_2} \right) \right) \end{aligned} \quad (2.8)$$

$$\begin{aligned} \bar{q}_l &= \int_0^{\infty} P(s) s ds \\ &= s_1 \frac{a}{2} \left(1 + \operatorname{erf} \left(\frac{s_1}{\sqrt{2}\sigma_1} \right) \right) + s_2 \frac{1-a}{2} \left(1 + \operatorname{erf} \left(\frac{s_2}{\sqrt{2}\sigma_2} \right) \right) \\ &\quad + \frac{a}{\sqrt{2\pi}} \sigma_1 \exp \left(-\frac{s_1^2}{2\sigma_1^2} \right) + \frac{1-a}{\sqrt{2\pi}} \sigma_2 \exp \left(-\frac{s_2^2}{2\sigma_2^2} \right) \end{aligned} \quad (2.9)$$

Note that for the introduced parametrisation the normalised parameters of the double-Gaussian PDF (a , $(s_1 - \bar{s})/\sigma$, $(s_2 - \bar{s})/\sigma$, σ_1/σ , σ_2/σ) only depend on sk (Eqs. 2.4–2.7). Therefore with $Q_1 \approx \bar{s}/\sigma$, Eqs. 2.8 and 2.9 can be rearranged such that C and the normalised average liquid water, \bar{q}_1/σ , are functions of sk and Q_1 only.

2.3.3. Parametrisation of the liquid water flux

In contrast to the cloud fraction and the average liquid water, the liquid water flux cannot be found analytically by taking only s into account, but it also depends on the vertical velocity, w . Instead of using a joint PDF of s and w , we are here heading for a more straightforward way following Cuijpers and Bechtold (1995). They determined the liquid water flux, $\overline{w'q'_1}$, from the flux of s , $\overline{w's'}$, by

$$\overline{w'q'_1} = FC\overline{w's'}, \quad (2.10)$$

where C is the cloud fraction. F is a proportionality constant that for $C < 1.0$ can be interpreted as a measure of which part of the joint PDF of w' and s' is found in the cloudy part of the domain. Therefore, $\lim_{C \rightarrow 1.0} F = 1.0$. Using coarse resolution LES data of shallow cumulus and stratocumulus cases, Cuijpers and Bechtold (1995) found a dependence of F on the normalised saturation deficit, Q_1 , and sk with the dependence on sk most notable near cloud base where sk is close to zero. Nevertheless, they suggest that F is described fairly well as a function of Q_1 only, giving $F = \exp(-1.4Q_1)$ for $Q_1 \leq 0$ and $F = 1.0$ for $Q_1 > 0$.

Using Eq. 2.10, we find from the different LES cases a dependence of F on both Q_1 and sk (Fig. 2.5, ARM and DYCOMS not shown). Using our training data sets (RICO, Fig. 2.5 a, and DYCOMS), we propose

$$F = \begin{cases} a \exp(b sk) Q_1^2 + 1 & \text{if } Q_1 \leq 0 \\ 1.0 & \text{if } Q_1 > 0 \end{cases} \quad (2.11)$$

with $a = 1.5$ and $b = 0.25$ for a new parametrisation. The proposed parametrisation seems to be appropriate also for the testing data sets (ARM and ASTEX, Fig. 2.5 b). Because this new parametrisation is too sensitive to high sk for $Q_1 < -4.0$ and therefore gives unreasonable values at a thin layer near cloud top, we limit their range of application to $Q_1 \geq -4.0$. We find $Q_1 < -4.0$ only in a thin layer at cloud top, where the liquid water flux is close to zero. A similar unreasonable behaviour is found for the parametrisation of Cuijpers and Bechtold (1995) and we will therefore apply the same limit to both parametrisations when testing it in the following with LES data. In a GCM or an NWP model the cloud top behaviour is very sensitive to the interplay of the cloud parametrisation and the boundary layer scheme. Therefore a meaningful validation of the cloud top

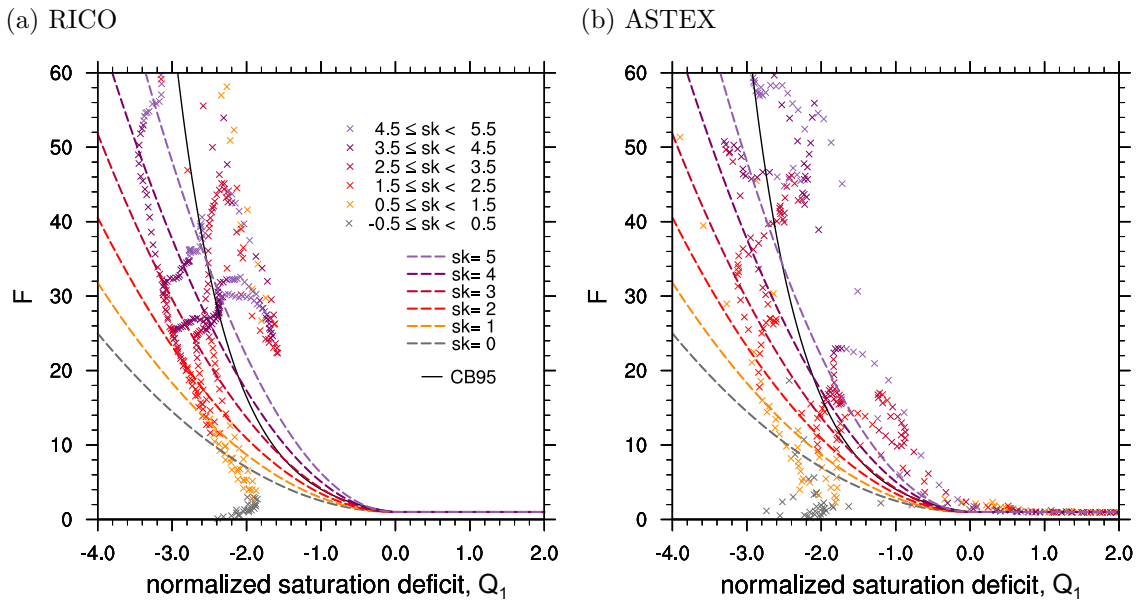


Figure 2.5.: New parametrization of F (dashed lines) as a function of the normalised saturation deficit and the skewness along with the parametrization of Cuijpers and Bechtold (1995, CB95) and the LES data (crosses).

behaviour should be done in such a model with all feedbacks present. However, as a first attempt $\overline{w'q_1'} = 0$ for $Q_1 < -4.0$ might be sufficient.

2.4. A priori testing of the cloud closure

Having introduced a new set of closure equations for σ_1/σ , σ_2/σ and F (Eqs 2.4 and 2.11, respectively), we now analyse the quality of the new parametrizations with a priori testing in LES and by comparing the introduced parametrizations with parametrizations from the literature. Note that the usefulness of a priori testing is in the assessment of validity and accuracy of the parametrizations assumptions (see e.g., Pope, 2000, p. 601). To decide which parametrization is most useful in a certain NWP model or GCM a comparison based on a posteriori testing has still to be done.

In Fig. 2.6, the new parametrization and the parametrization of Larson et al. (2001a) are shown compared to the LES data of the ASTEX case, which is one of the testing data sets. We focus on the cumulus part of the ASTEX case (positive sk and negative Q_1) because the main differences between these two parametrizations are found for the cumulus regime. For stratocumulus the two parametrizations differ only marginally.

For high positive skewness it is found that the new parametrization reproduces the LES data better than the parametrization of Larson et al. (2001a), which overestimates C and \bar{q}_1 for a given Q_1 . Remember that zero skewness for the closure equations equals the case of a single-Gaussian distribution of s (like assumed in Sommeria and Deardorff,

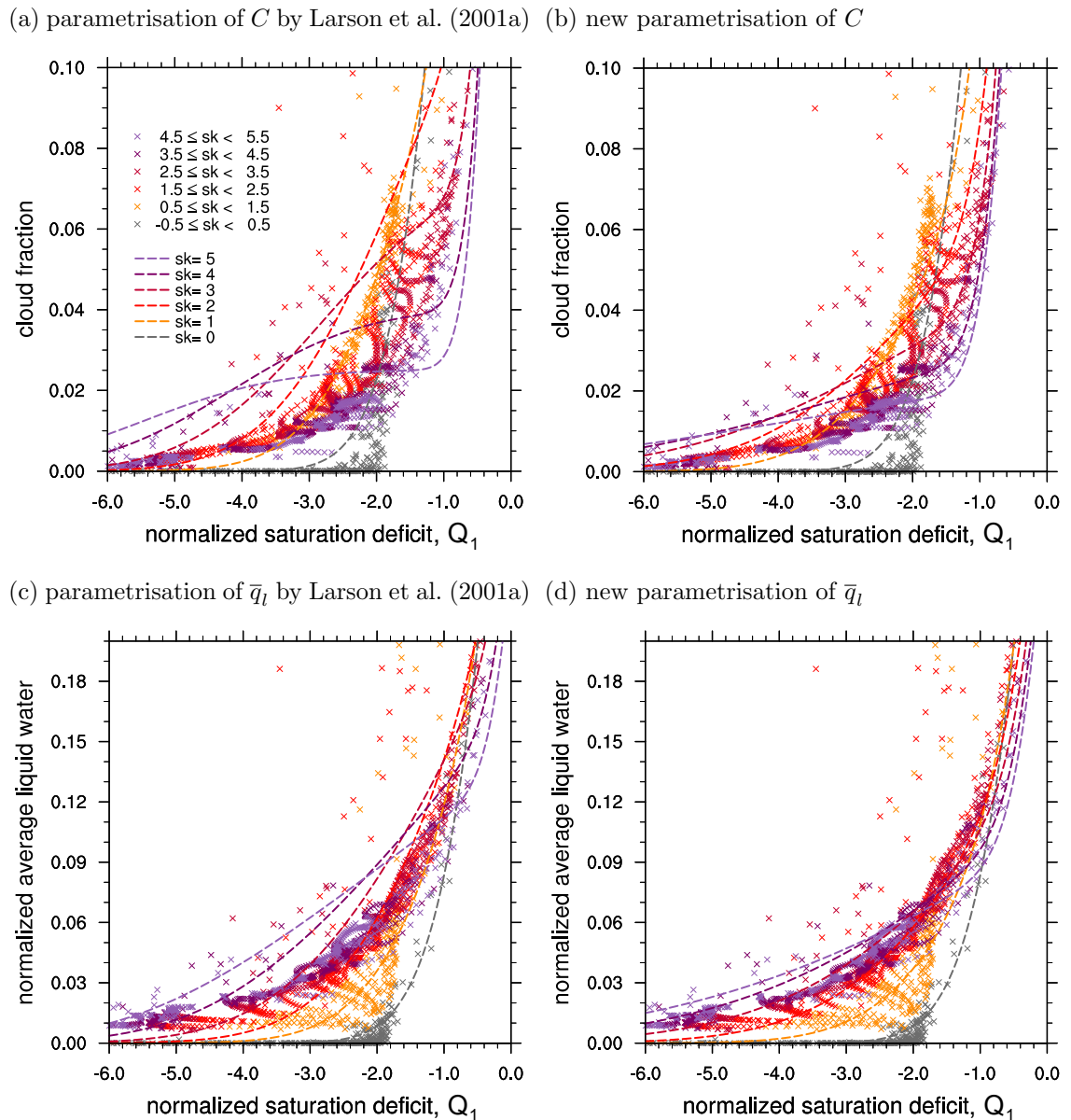


Figure 2.6.: The parametrisations (dashed lines) as a function of the normalised saturation deficit and the skewness applied to the LES data of the ASTEX case (crosses).

1977; Mellor, 1977), while in the LES data bimodal distributions occur as well. In this case and with increasing normalised saturation deficit (which at cloud base corresponds to increasing height), the parametrisations first overestimate and later underestimate the cloud fraction. For the normalised average liquid water the effect is less relevant (see also Fig. 2.7).

To give an estimate of the error of the different parametrisations, the profiles of C , \bar{q}_1 and $\overline{w'q'_1}$ from the LES test data sets are compared with the results of the different parametrisations (Fig. 2.7 a, b and c). The new parametrisation is able to reproduce

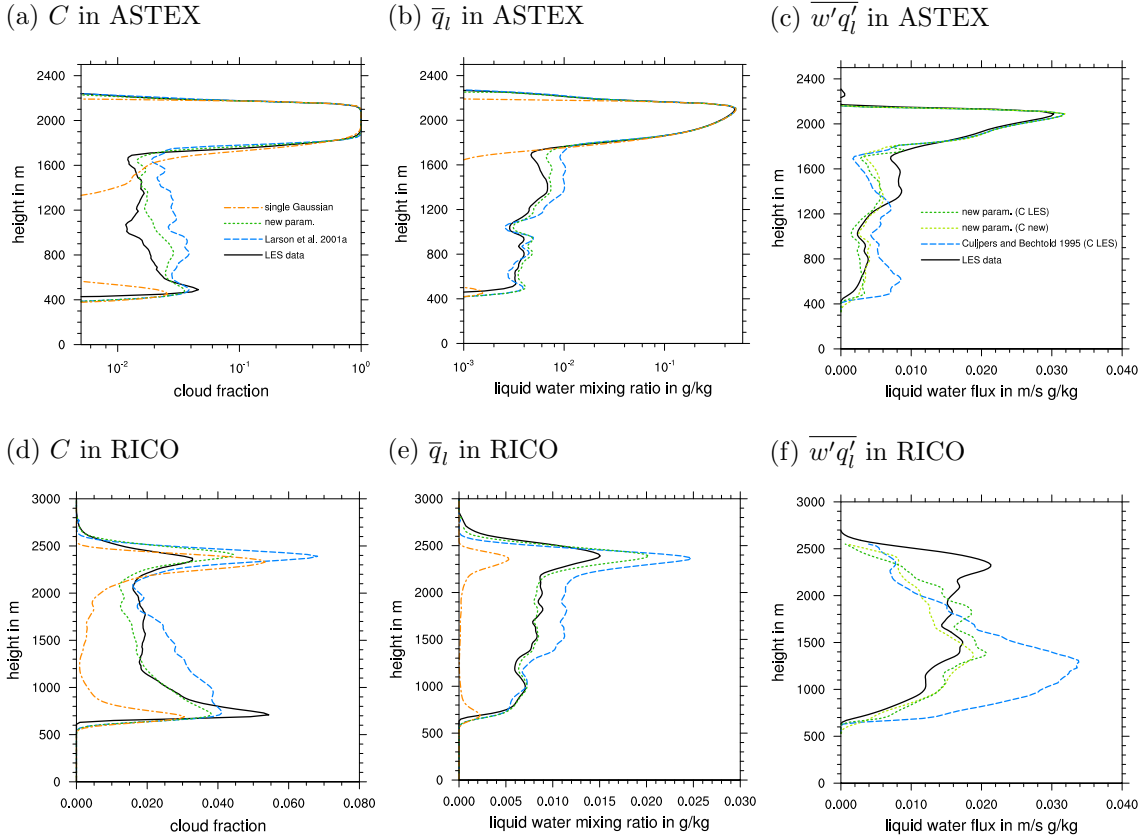


Figure 2.7.: Profiles of cloud fraction, average liquid water and the liquid water flux from LES cases ASTEX (testing data set) after 25 h and RICO (training data set) after 36 h of simulation. For the liquid water flux, C used in Eq. 2.10 has either been taken from the original LES data (C LES) or from the new parametrisation (C new). The legend in (a) also applies to (b, d, e), the legend in (c) also applies to (f). Note the logarithmic scale on the x axis in (a) and (b).

the profiles of C and \bar{q}_l in the shallow cumulus layer better than the parametrisation using the closure equations from Larson et al. (2001a). Both cloud schemes are clearly superior to a single-Gaussian cloud closure, which severely underestimates \bar{q}_l and C and in particular is hardly able to diagnose any liquid water between cloud base and cloud top in the shallow cumulus layer. For the stratocumulus layer, the three parametrisations do not differ noticeably. A distinct difference between testing error (as in ASTEX; Fig. 2.7 a and b) and training error (as in RICO; Fig. 2.7 d and e) is not found.

For the profiles of $\overline{w'q'_l}$, Eq. 2.10 is used with F parametrised like suggested for the new parametrisation. For comparison the parametrisation by Cuijpers and Bechtold (1995) using an exponential fit of F that only depends on Q_1 is also shown in Fig. 2.7 c for the ASTEX case. The new parametrisation is able to reproduce the shape of the profiles of $\overline{w'q'_l}$ as well as their absolute values. Again, for stratocumulus the two parametrisation do not differ noticeably. To estimate the effect of C in the new parametrisation, C used in Eq. 2.10 has either been taken from the original LES data or from the new parametrisation.

Table 2.2.: Errors of the different parametrisations for the testing data sets, ASTEX and ARM.

		C			\bar{q}_1			$\overline{w'q'_1}$	
		[%]			[g kg ⁻¹ × 10 ⁻³]			[g kg ⁻¹ m s ⁻¹ × 10 ⁻³]	
		SG	L01	new para.	SG	L01	new para.	CB95	new para.
ASTEX	l_1	1.10	0.66	0.41	2.37	1.21	0.72	3.39	2.43
	RMSE	2.67	1.26	0.88	4.00	2.00	1.51	5.22	3.54
	l_∞	19.70	9.31	7.05	23.12	10.73	10.98	19.11	11.44
	bias	-0.16	0.35	0.19	-1.22	0.82	0.42	-1.41	-0.83
ARM	l_1	1.35	0.61	0.53	4.60	0.97	0.57	35.51	8.72
	RMSE	1.85	0.84	0.87	6.67	1.42	1.15	42.10	11.78
	l_∞	5.33	2.83	3.58	16.00	6.10	6.30	109.93	34.73
	bias	-1.21	0.30	-0.02	-4.43	-0.29	0.32	35.51	5.30

Parametrisations: SG – single Gaussian, L01 – Larson et al. (2001a), CB95 – Cuijpers and Bechtold (1995), new para. – new parametrisation. Error metrics: $l_1 = 1/n \sum_{i=0}^n |\Delta x_i|$, $\text{RMSE} = (1/n \sum_{i=0}^n (\Delta x_i)^2)^{0.5}$, $l_\infty = \max_{i=0}^n |\Delta x_i|$ and $\text{bias} = 1/n \sum_{i=0}^n \Delta x_i$ with $\Delta x_i = x_{\text{para.},i} - x_{\text{LES},i}$, $x \in [C, \bar{q}_1, \overline{w'q'_1}]$ and i being a index for different vertical levels and output time steps. Values shown are averages over the last three output time steps of the LES data, where clouds are present, and over all vertical levels, where either $x_{\text{LES},i}$ or $x_{\text{para.},i}$ are nonzero. To calculate $\overline{w'q'_1}_{\text{para.}}$, C_{LES} has been used in Eq. 2.10. Smallest errors are printed in bold, largest in typewriter. Note that the parametrisations of $\overline{w'q'_1}$ is only valid for $Q_1 \geq -4.0$, while C and \bar{q}_1 are calculated over the whole range of Q_1 .

Table 2.3.: Errors of the different parametrisations for the training data sets, RICO and DYCOMS.

		C			\bar{q}_1			$\overline{w'q'_1}$	
		[%]			[g kg ⁻¹ × 10 ⁻³]			[g kg ⁻¹ m s ⁻¹ × 10 ⁻³]	
		SG	L01	new para.	SG	L01	new para.	CB95	new para.
RICO	l_1	1.19	0.88	0.41	4.91	1.81	0.71	7.54	2.61
	RMSE	1.44	1.16	0.59	6.03	2.51	1.08	8.80	3.81
	l_∞	3.28	3.57	2.05	14.19	7.61	3.98	18.68	10.97
	bias	-0.87	0.76	0.03	-4.86	1.28	0.32	3.01	-1.29
DYCOMS	l_1	3.09	1.53	1.73	4.17	3.24	3.42	1.07	0.84
	RMSE	4.24	2.83	3.06	8.26	6.95	7.34	1.50	1.04
	l_∞	11.03	9.73	9.98	27.24	28.49	31.70	5.43	2.43
	bias	-0.74	-0.51	-0.51	-3.27	-0.99	-0.97	0.69	0.33

For further description of the abbreviations and error measures please see Table 2.2.

It is shown that C has a minor influence on the profile compared to the difference between the two different parametrisations of F . At the top of the cumulus layer for both the test data set ASTEX and the training data set RICO the new parametrisation underestimates $\overline{w'q'_1}$. Note again that for a shallow layer with $Q_1 < -4.0$ at cloud top the parametrisations of the liquid water flux are not valid while the liquid water flux is close to zero.

For a more quantitative analysis, the errors of the different parametrisations are summarised for the testing data sets in Table 2.2 and for the training data sets in Table 2.3. The different error metrics used are the mean absolute error, l_1 , the root mean square error, RMSE, the maximum absolute error, l_∞ and the bias. Their computation formulas are given in the caption of Table 2.2. For the cloud fraction and the average liquid water, the proposed closure equations are fit to the LES data sets of RICO and DYCOMS. There-

fore the new parametrisation is optimised for RICO and DYCOMS and the error given for the new parametrisation for those cases is a training error, which is potentially lower than the error of an independent test data set. Nevertheless, we do not find a perceptible higher error for the test data sets ASTEX and ARM compared to the training data sets RICO and DYCOMS.

For all four LES data sets, the single-Gaussian parametrisation performs poorly compared to the other two parametrisations, which are based on double-Gaussian distributions. Though the double-Gaussian parametrisations are restricted to their double-Gaussian families by the respective closure equations, both double-Gaussian families are able to represent skewed distributions while a single-Gaussian distribution is not skewed. Therefore the double-Gaussian families are able to represent both cumulus and stratocumulus. For stratocumulus the absolute values of skewness are less than for cumulus, therefore the difference in the errors between the single-Gaussian and the double-Gaussian parametrisations is smaller.

Comparing the two parametrisations based on double-Gaussian distributions, the new parametrisation matches the LES data better than the parametrisation by Larson et al. (2001a) for ASTEX, whereas for ARM the two parametrisations have similar error magnitudes (Table 2.2). This is reasonable, because the closure equations have most notably been changed for high positive skewness, which frequently occurs in ASTEX but is rather scarce for ARM. The same effect can also be found in the training error (Table 2.3). While a lower error of the new parametrisation compared to the error of the parametrisation of Larson et al. (2001a) is found for RICO (where high positive skewness occurs frequently), similar error magnitudes are found for DYCOMS (where the skewness is small).

For the liquid water flux, the error of the parametrisation can be reduced distinctly by the new parametrisation compared to the parametrisation of Cuijpers and Bechtold (1995). The new parametrisation depends on Q_1 as well as on sk while the parametrisation of Cuijpers and Bechtold (1995) is only dependent on Q_1 . The additional dependence of the new parametrisation on sk enables a more precise estimation of F , which reduces the error in all four LES cases.

2.5. Error dependence on domain size and the role of mesoscale structures

NWP models approach resolutions of only a few kilometres (e.g., Baldauf et al., 2011), which is considerably less than the domain sizes of all our LES cases. Hence, the question arises if the introduced PDF scheme is still applicable at such resolutions. We therefore investigate the dependence of the error of the new parametrisations on the domain size considered. To do so the domain of the four different RICO simulations has been divided into subdomains, the RMSE and the bias have been calculated in each subdomain and

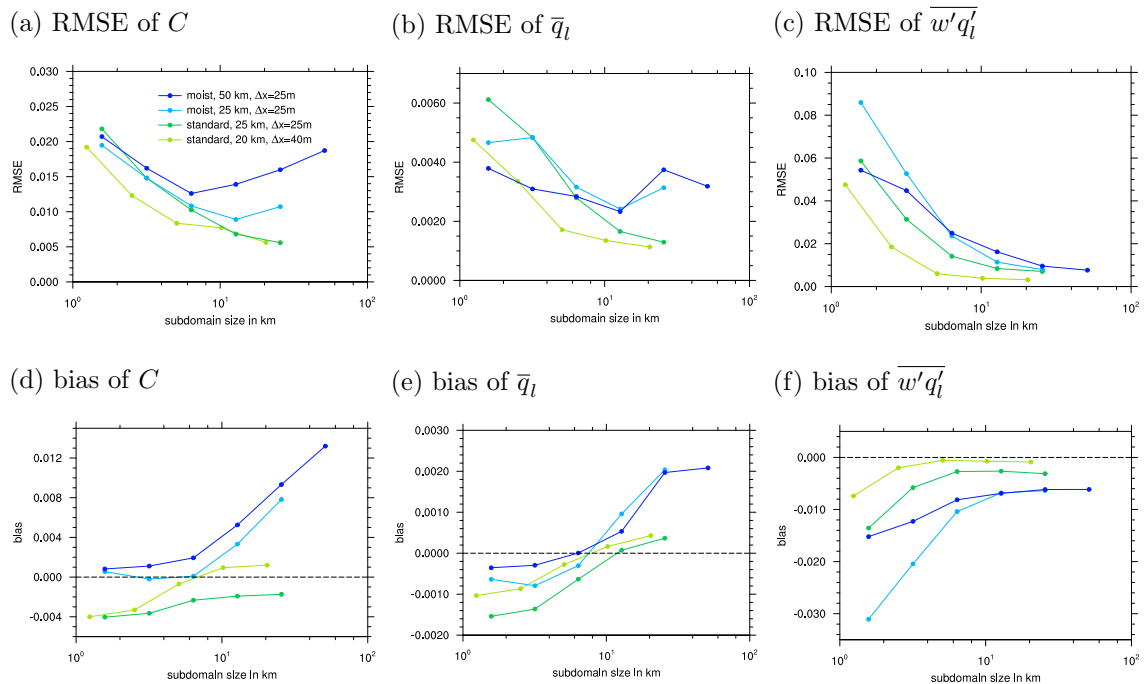


Figure 2.8.: Dependence of the error of the parametrised cloud fraction, liquid water and liquid water flux on the domain size. Shown are different simulations of the RICO case (average error over two output time steps after 24 h); in the moist RICO cases mesoscale structures develop, while in the standard cases the cloud field remains random.

then averaged over all subdomains of the same size. These subdomains in our analysis of the LES data correspond to the grid spacing of an NWP or mesoscale model. The RICO simulations used differ in their overall domain size as well as in the initial humidity profiles of the simulations, giving “standard RICO” and “moist RICO” simulations (see Sect. 2.2.1).

For subdomain sizes smaller than 5 km, the RMSE increases rapidly with decreasing subdomain size for both standard and moist RICO simulations (Fig. 2.8). This rapid increase is probably due to the subdomain size approaching the size of individual cloud structures (i.e., larger cumulus clouds). When these two scales converge, the variability increases rapidly and a continuous, smooth distribution like the proposed family of double-Gaussian PDFs cannot appropriately represent the shapes of the subdomain PDFs. This results in a larger spread of the LES data around the closure equations and consequently in an increasing RMSE with decreasing subdomain size. The increasing RMSE can be interpreted such that the PDF-based, deterministic scheme becomes inappropriate at such small scales and one would have to use a stochastic approach instead.

With standard initial conditions, rain rates are small and no mesoscale structures develop, i.e., the cloud field remains random. Then, for subdomain sizes larger than 10 km the RMSE is small, being around 0.005 and 0.001 g kg^{-1} for cloud fraction and liquid water, respectively. With moist initial conditions, precipitation appears more readily and

mesoscale structures, such as cloud streets, mesoscale arcs and cold pools, develop from 20 h onwards as discussed by Seifert and Heus (2013). In these moist cases and with subdomain sizes larger than 10 km, the cloud fraction as well as the liquid water are mostly overestimated by the double-Gaussian parametrisation (positive bias). The RMSE amounts to about 0.017 and 0.04 g kg⁻¹ for cloud fraction and liquid water, respectively, which for each variable corresponds to roughly 10 % of their respective maximum values. With decreasing subdomain size the RMSE for the moist RICO simulations decreases until the subdomain size reaches 5–10 km. At such subdomain sizes the RMSE is similar for standard and moist RICO simulations. For the moist RICO simulations and large subdomain sizes, the PDFs of s have comparatively longer tails with few very high values of s . This different shape emerges from the more localised but more intense convection and the large cloud free cold pool areas in the moist RICO case. The parametrised double-Gaussian PDF, which is fitted to non-organised random cloud fields with small rain rates, is not able to capture the longer tails of the distributions of s adequately. Therefore, for a given skewness the normalised variance σ_1/σ is underestimated for moist RICO simulations with mesoscale structures.

The discussed error dependence on the domain size and the investigation of the moist RICO case show, on the one hand, that even with a perfect knowledge of the first three moments of the PDF of s it remains challenging to construct a parametrisation that is truly scale adaptive. On the other hand, the statistics of the cloud field at small scales seems to be independent enough from the mesoscale structures and higher rain rates to make the PDF scheme useful for a broader range of cloud regimes than the original LES data set used for the parametrisation. Taking into account both the increasing error at very small subdomain sizes and the difficulties of the scheme to represent cloud properties in the moist RICO case, we conclude that the proposed scheme is most appropriate for NWP models or GCMs with horizontal resolution of about 5–20 km.

For the liquid water flux, the new parametrisation does not depend explicitly on a certain family of PDFs but the factor F is directly parametrised and depends on Q_1 and sk . With this parametrisation the error of the liquid water flux seems to be less dependent on the development of mesoscale structures and higher rain rates, possibly because there is no direct dependence of the parametrisation on the shape of the PDF of s . A dependence of the error of the liquid water flux on the subdomain size is found in accordance with the error of the cloud fraction and average liquid water.

2.6. Extension to autoconversion rate

Autoconversion of cloud droplets to rain drops is a key process in the formation of precipitation in warm clouds. Besides the cloud fraction, the average liquid water and the liquid water flux discussed above, the autoconversion rate is another variable that depends

among others on the variability of the liquid water mixing ratio (e.g., Pincus and Klein, 2000). In simple autoconversion schemes (e.g., Kessler, 1969; Sundqvist, 1978), other dependencies are neglected and the autoconversion rate only depends on the liquid water mixing ratio. With this simplification the autoconversion rate can also be handled by PDF-based schemes.

Following Kessler (1969, K69) and replacing the liquid water mixing ratio with the extended liquid water mixing ratio, the autoconversion rate, A_{K69} , is given as

$$A_{K69}(s) = k(s - s_{\text{crit}})H(s - s_{\text{crit}}), \quad (2.12)$$

where H is the Heaviside step function, $s_{\text{crit}} = 0.5 \text{ g kg}^{-1}$ is a critical threshold below which no autoconversion occurs and k is a rate constant set to $k = 10^{-3} \text{ s}^{-1}$.

Alternatively, Khairoutdinov and Kogan (2000, KK00) suggested a parametrisation based on data from a single Large-Eddy Simulation using spectral bin microphysics, i.e., resolving the drop size distribution explicitly. They found that a good fit to the bulk autoconversion rate is

$$A_{KK00}(s) = c_1 s^{c_2} H(s) \quad (2.13)$$

with $c_1 = (\frac{5.829 \times 10^6}{N_c})^{c_2}$ and $c_2 = 1.89$. Within the factor c_1 , they introduced a dependence on the number of cloud droplets, N_c . Because N_c in UCLA-LES is assumed to be constant throughout a simulation, c_1 can be treated as constant in this study.

For both autoconversion schemes, K69 and KK00, the domain-averaged autoconversion rate, \bar{A} , is then found by integration over the PDF of s :

$$\bar{A}_{\text{para.}} = \int_{s_0}^{\infty} A_{\text{para.}}(s)P(s)ds \quad (2.14)$$

with $s_0 = s_{\text{crit}}$ for Kessler (1969) and $s_0 = 0 \text{ g kg}^{-1}$ for Khairoutdinov and Kogan (2000). While the integral can be solved analytically for Kessler (1969), this is not possible for the scheme of Khairoutdinov and Kogan (2000) because the exponent of s , c_2 , is not a natural number.

Seifert and Beheng (2001, SB01) derived an explicit equation for the autoconversion rate, which is formulated using Long's piecewise polynomial collection kernel and a universal function that is estimated by numerically solving the stochastic collection equation. Doing so they arrived at

$$A_{SB01} = \frac{k_{\text{au}}k_{\tau}\rho_0}{N_c^2} s^4 H(s) \quad (2.15)$$

with $k_{\text{au}} = 6.808 \times 10^{18} \text{ m}^3 \text{ kg}^{-1} \text{ s}^{-1}$ and $k_{\tau} = 1 + \frac{\Phi_{\text{au}}(\tau)}{(1-\tau)^2}$. Here ρ_0 is the base state

density depending on height and $\Phi_{\text{au}}(\tau)$ is a universal function depending on the internal timescale, $\tau = 1 - q_l/(q_l + q_r)$, designed to take into account the broadening of the droplet spectrum with time. Note that q_r is the rainwater content, which is not included in q_l . This dependence on the internal timescale makes it impossible to integrate A_{SB01} according to Eq. 2.14 as long as the PDF of τ is unknown in terms of the PDF of s , which would require the use of a joint PDF or even the introduction of time correlations to the problem. Nevertheless, as the SB01 autoconversion rate is expected to give more realistic results than the simple autoconversion schemes described above, the SB01 autoconversion rate is used as a reference to be compared to the other autoconversion schemes. In our study the full 4-D field of τ is, of course, known from LES and a compensatory factor for k_τ can be determined for each level and each time step individually by solving

$$\begin{aligned} & \overline{A}_{\text{LES}}(z, t) \\ = & k_{\tau, \text{LES}}(z, t) \frac{1}{(nx)^2} \frac{k_{\text{au}} \rho_0}{N_c^2} \sum_{i=1}^{nx} \sum_{j=1}^{nx} s^4(x_i, y_j, z, t) H(s) \end{aligned} \quad (2.16)$$

for $k_{\tau, \text{LES}}$. Here nx is the number of LES grid boxes in each horizontal direction. Then the ability of the new double-Gaussian parametrisation to be used in combination with the SB01 autoconversion rate can be tested using $k_{\tau, \text{LES}}$:

$$\overline{A}_{\text{SB01}} = k_{\tau, \text{LES}}(z, t) \frac{k_{\text{au}} \rho_0}{N_c^2} \int_0^\infty s^4 P(s) ds. \quad (2.17)$$

Note that for the use in an NWP model or a GCM, $k_{\tau, \text{LES}}$ would have to be estimated by some other method and that $k_{\tau, \text{LES}}$ is not equal to a horizontal mean of k_τ .

From Fig. 2.9 showing the different autoconversion rates for the ASTEX case, it is apparent that the profiles of the autoconversion rate differ substantially both in shape and by several orders of magnitude in absolute value among the different parametrisations of the autoconversion rate (K69, KK00, SB01). While the single-Gaussian cloud closure only captures the stratocumulus type cloud layer around 2100 m, the new double-Gaussian cloud closure is additionally able to diagnose the autoconversion rate quite accurately for the cumulus layer. The same results hold for the other three LES cases (not shown).

Using $k_{\tau, \text{LES}}$ as described above, the new double-Gaussian cloud closure is able to reproduce the profile of the SB01 autoconversion rate well for most heights. This is remarkable because A_{SB01} is proportional to the 4th moment of s , which makes $\overline{A}_{\text{SB01}}$ especially sensitive to errors introduced by the cloud closure. Nevertheless, at the cloud top of the stratocumulus layer the new double-Gaussian cloud closure overestimates the SB01 autoconversion rate. This overestimation might be related to the difficulties of LES in resolving the strong gradients that occur at a stratocumulus cloud top.

Using the closure equations of Larson et al. (2001a) (as it is done exemplarily with the KK00 parametrisation in Fig. 2.9) compared to using the new closure equations gives small

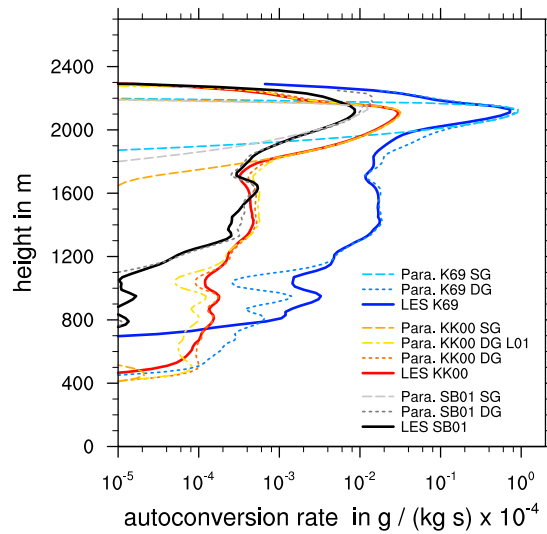


Figure 2.9.: Profile of the autoconversion rate in ASTEX after 25 h of simulation. Note the logarithmic scale on the x axis. Notation: LES: autoconversion rate calculated using the full 3-D field of LES data, SG: single-Gaussian parametrisation, DG: double-Gaussian parametrisation using the new closure equations, DG L01: double-Gaussian parametrisation using the closure equations from Larson et al. (2001a).

and probably negligible differences in the cumulus layer.

Overall the double-Gaussian PDF scheme is successful in capturing the effect of the subgrid variability on the autoconversion rate, which is crucial for the representation in the cumulus layer. Nevertheless, the uncertainty due to the choice of the autoconversion scheme itself remains. Especially the K69 scheme leads to a strong overestimation compared to KK00 and SB01, but also KK00 shows a much higher autoconversion rate in the lowest part of the cumulus cloud layer compared to SB01.

2.7. Conclusions

We introduce a refined statistical cloud closure using double-Gaussian PDFs. Following the work of Larson et al. (2001a), who provided an elegant framework for a diagnostic parametrisation of the cloud fraction and the average liquid water, we modified their parametrisation especially in the case of strong positive skewness of the distribution of the extended liquid water mixing ratio, s , i.e., for shallow cumulus clouds. The introduced double-Gaussian closure is based on different LES case studies and is supported by observational data from aircraft measurements in shallow cumulus. It is relying on the first three moments of s as input parameters and is shown to be superior in diagnosing the cloud fraction and average liquid water profiles compared to a single-Gaussian approach that only needs the first two moments of s for input. A priori testing also suggests improved accuracy compared to existing double-Gaussian closures.

For the liquid water flux, we introduce a new parametrisation of the factor F , which is relating the liquid water flux to the flux of s . With F depending on the skewness of the distribution of s and the normalised saturation deficit, the new parametrisation is able to reproduce the shape of the profiles of the liquid water flux better than when the dependence of the skewness is not retained.

The dependence of the error of the parametrisation on the domain size and the appearance of mesoscale structures has also been tested a priori with LES. Below a domain size of about 5 km the error of the parametrisation of the cloud fraction, the average liquid water and the liquid water flux is increasing rapidly with decreasing domain size. If mesoscale structures occur that are accompanied by higher rain rates and the domain size is chosen large enough to include these mesoscale structures, the error of the parametrisation of the cloud fraction and the liquid water is larger than without the occurrence of mesoscale structures. Considering the liquid water flux, the error of the parametrisation seems to be insensitive to the occurrence of mesoscale structures.

Finally, the cloud scheme has been applied to diagnose the autoconversion rate. Using autoconversion schemes of different complexity, the new parametrisation is able to reproduce profiles of the autoconversion rate adequately. The differences between the various autoconversion schemes are much larger than the error introduced by the double-Gaussian closures.

As a next step, a posteriori testing of the introduced parametrisation in a NWP model or a GCM that diagnoses or predicts the first three moments of s , e.g., from a higher-order closure boundary layer model (Machulskaya and Mironov, 2013), is essential to decide which parametrisation is most useful in the chosen NWP model or GCM.

CHAPTER 3

A LAGRANGIAN DROP MODEL TO STUDY WARM RAIN MICROPHYSICAL PROCESSES¹

Wer bin ich
und wenn ja, wie viele?

(Richard David Precht)

In this chapter, a Lagrangian drop (LD) model to study warm rain microphysical processes is introduced. The approach combines Large-Eddy Simulations (LES) including a bulk microphysics parametrisation with an LD model for raindrop growth. The LD model is one-way coupled with the Eulerian LES and represents all relevant rain microphysical processes such as evaporation, accretion and selfcollection among LDs as well as dynamical effects such as sedimentation and inertia. To test whether the LD model is fit for purpose, a sensitivity study for isolated shallow cumulus clouds is conducted. We show that the surface precipitation rate and the development of the raindrop size distribution (RSD) are sensitive to the treatment of selfcollection in the LD model. Some uncertainty remains for the contribution of the subgrid-scale turbulence to the relative velocity dif-

¹This chapter has been submitted with minor modifications and is currently in review as: Naumann, A. K. and A. Seifert (2015): A Lagrangian drop model to study warm rain microphysical processes in shallow cumulus. *J. Adv. Model. Earth. Syst.*, in review.

ference of a pair of LDs, which appears as a factor in the collision kernel. Sensitivities to other model parameters such as the initial multiplicity or the initial mass distribution are small. Overall, sensitivities of the LD model are small compared to the uncertainties in the assumptions of the bulk rain microphysics scheme and the LD model is well suited for particle-based studies of raindrop growth and dynamics. This opens up the opportunity to study effects like recirculation, deviations from terminal fall velocity and other microphysical phenomena that so far were not accessible for bin, bulk or parcel models.

3.1. Introduction

In atmospheric modelling, microphysical processes are traditionally parametrised on Eulerian grids either using bulk schemes or (potentially more accurate) bin schemes. On a microphysical process level, a Lagrangian approach is the most natural framework to study cloud droplet and raindrop development. Recently, the super-droplet method has been introduced to study cloud droplet behaviour on a particle-based level and on domain sizes of a few kilometres (Shima et al., 2009; Andrejczuk et al., 2010; Riechelmann et al., 2012). Because cloud droplets are typically orders of magnitude more numerous than raindrops, those studies focus their computational resources mostly on cloud droplet behaviour and an adequate representation of the tail of the drop size distribution, which is decisive for precipitation characteristics, is challenging. In this chapter, we introduce a Lagrangian drop (LD) model that focuses on the raindrop phase and that targets specifically the warm rain microphysical processes and the growth history of raindrops after the initial formation of drizzle drops.

Warm rain bulk microphysics parametrisations usually distinguish between two hydrometeor classes: cloud droplets and raindrops (Kessler, 1969; Beheng, 1994; for a triclass parameterization see, e.g., Sant et al., 2013). While the precise separation value in terms of drop radius or mass may differ between the studies, the cloud droplet class is generally defined such that the sedimentation velocity is negligible and cloud droplets are assumed to evaporate immediately when they encounter subsaturated air. For raindrops in contrast condensational growth is neglected because collision-coalescence – both with cloud droplets and among raindrops – is the dominant growth mechanism. Also, raindrops do not behave like massless particles but have a mass-dependent sedimentation velocity and experience inertial effects.

To describe the cloud droplet and the raindrop development in space and time, bulk schemes assume that the cloud droplet size distribution and the RSD in a model grid box can be described well by a family of distributions with few free parameters. Changes in the RSD due to microphysical processes are then formulated as changes in the moments of the RSD. The different moments of the RSD have different sedimentation velocities, which in higher moment schemes generally allows for a representation of gravitational sorting

but is also known to produce too excessive sorting and even the occurrence of shock waves (Wacker and Seifert, 2001; Mansell, 2010; Milbrandt and McTaggart-Cowan, 2010).

In bin schemes the drop size distribution in each model grid box is discretised in a (large) number of size bins, and the temporal development of the number of raindrops in each bin is calculated for each bin separately. Therefore no artificial distinction between cloud droplets and raindrops is needed and (provided that the number of bins is high) the shape of the drop size distribution can evolve freely. Bin schemes are, however, known to encounter diffusion among bins and across grid box boundaries (Stevens et al., 1996b), which hinders a correct representation of important processes such as sedimentation. Another limitation of the bin schemes is that all particles in a bin have identical properties, e.g., fall speeds. This makes it difficult to study inertial effects or the history of raindrops.

In the LD model, we use the distinction between cloud droplets and raindrops from the bulk approach. We run a LES model with a conventional two-moment bulk microphysics scheme that simulates both the cloud droplet and the raindrop phase (Stevens and Seifert, 2008). In addition, the LD model also simulates the raindrop phase of the drop development but is run without feedbacks on the Eulerian LES fields. The RSD in the LD model is not restricted but each LD follows its own trajectory and size evolution driven by the time-dependent, thermodynamical background fields of the Eulerian LES. By allowing for subgrid-scale positions of the LDs within the Eulerian grid also sedimentation and gravitational sorting are considered inherently.

We intend the LD model to be used as a tool to understand warm rain microphysical processes in shallow cumulus on a particle-based level. The LD model is suited to investigate a range of questions such as the effect of subcloud layer evaporation on the RSD, the importance of “lucky raindrops” for the formation of surface precipitation (Magaritz et al., 2009) or the role of a subsiding shell for the growth history of raindrops in shallow cumulus (Heus and Jonker, 2008). In this chapter, we test whether a particle-based model can be used to investigate these questions, i.e., whether the LD model is fit for purpose. To do this, we critically examine the assumptions made in the particle-based approach and attempt to quantify the uncertainties of the LD model. Such a quantification of the uncertainties of the introduced LD model is an essential prerequisite before the method can be applied to specific research questions such as those outlined above or those discussed in Chapter 4 and Chapter 5.

The rest of the chapter is structured as follows: In Sect. 3.2 we shortly describe the LES model and the model setup for a test case of lightly precipitating shallow cumulus. We then introduce the LD model in Sect. 3.3, in particular the initialisation of the LDs, the calculation of their trajectories, and the growth and shrinking mechanisms – accretion, selfcollection and evaporation. In that section we also briefly mention sensitivities to choices of model parameters from the test case setup that are found to be small. In Sect. 3.4 we focus on those sensitivities to model assumptions that are relatively large

and require a more detailed discussion: inertia, the subgrid-scale contribution of the fluid velocity, and their effects on the selfcollection rate. In Sect. 3.5 we set the sensitivities of the LD model in context to uncertainties in the bulk microphysics parametrisation. Finally, in Sect. 3.6 we give some concluding remarks.

3.2. Test case description

3.2.1. Large-Eddy Simulation

We use the UCLA-LES (Stevens et al., 2005a; Stevens, 2007) with a third-order Runge–Kutta scheme for time stepping. Prognostic equations are solved for the three components of the velocity, the total water mixing ratio, the liquid water potential temperature, the mass mixing ratio of rainwater and the mass specific number of raindrops. Warm cloud and rain microphysical processes are parametrised by the two-moment bulk microphysics scheme of Seifert and Beheng (2001) with a diagnostic shape parameter (Seifert, 2008) and a fixed cloud droplet density. We adjusted the density correction exponent to 0.35 to better fit the behaviour of small raindrops (see discussion in Appendix B). Subgrid-scale fluxes are modelled with the Smagorinsky–Lilly model.

3.2.2. Case setup

We use two variants of a case study of shallow cumulus over the ocean (Rain In Cumulus over the Ocean; RICO; see Rauber et al., 2007). For the standard RICO simulation the initial profiles and the large-scale forcing are described by van Zanten et al. (2011). The moist RICO case differs from the standard setup only by a moister initial profile and was first used by Stevens and Seifert (2008). For large domains this moister setup results in a higher rain rate, which is both a result of and also a cause for mesoscale organization (Seifert and Heus, 2013). We choose a much smaller domain size of 3.2 km in both horizontal directions. This has the advantage that there is basically a single cloud in the whole domain at one time, which allows us to isolate the behaviour of an individual cloud.

We use a vertical domain size of 3.2 km and 4.0 km for the standard and moist RICO setup, respectively, and a grid spacing of 25 m in all spatial directions for both setups. The time step is 1 s. The Eulerian model is run for 24 h and 17 h for the standard and moist RICO setup, respectively. We then select the cloud that develops the most bulk rainwater for each run. Over the course of the lifetime of those two clouds (each 1.5 h), we let the model run again including the LDs and output the LD properties with a temporal resolution of 15 s. In the following, we refer to the cloud selected from the standard RICO setup as cloud A and to the cloud selected from the moist RICO setup as cloud B. We do not claim that cloud A (B) is more representative for drier (moister) environmental conditions but the two selected clouds should be seen as different realisations of shallow

Table 3.1.: Characteristic properties of cloud A and cloud B.

	t_{cloud} [min]	A_{max} [km ²]	LWP [g/m ²]	RWP [g/m ²]	z_{base} [m]	$z_{\text{top, max}}$ [m]
cloud A	45	3.3	99	7.1	600	2500
cloud B	55	2.4	94	5.7	650	2000

t_{cloud} – cloud lifetime, A_{max} – maximum cloud area, LWP – mean in-cloud liquid cloud water path, RWP – mean in-cloud rainwater path, z_{base} – mean cloud base height, $z_{\text{top, max}}$ – maximum cloud top height

cumulus convection from slightly different environmental conditions. Some characteristic properties of the two clouds are given in Table 3.1. Overall, cloud B has a longer lifetime than cloud A and shows features of pulsating growth (Rauber et al., 2007; Heus et al., 2009) while the development of cloud A is characterised by a single but stronger updraft.

3.3. Lagrangian drop model

The LD method used here is based on the super-droplet approach (Andrejczuk et al., 2008; 2010; Shima et al., 2009; Riechelmann et al., 2012), but adapted to focus on the raindrop distribution by considering basically two differences: First, instead of modeling the whole lifecycle of drops from their nucleation via a cloud droplet phase until a few of them eventually reach raindrop size, we simulate the raindrop phase only and initialise the LDs according to the autoconversion rate of the bulk microphysics scheme. Therefore errors of the bulk autoconversion rate are not circumvented by the LD model. However, the focus of the LD model is to study the raindrop phase and by avoiding nucleation and cloud droplet growth processes for the LDs, (computational) resources are concentrated on the raindrop phase, which is very effective because cloud droplets are typically several orders of magnitude more numerous than raindrops.

A second major difference to the super-droplet method is that we do not use a two-way coupling of the LDs to the Eulerian model. The LD model uses the data from the Eulerian LES as input but is not coupled back to the Eulerian model. The Eulerian LES is run including all microphysics, especially also including the rain microphysics. Such a one-way coupling poses limitations on the usage of the LD model because differences in the rainwater fields of the bulk microphysics and the LD model result from the different formulations of microphysical processes and may lead to inconsistencies. We will show later in Sect. 4.2 that the differences in the rainwater fields are small and that therefore a one-way coupling is indeed appropriate here. Moreover, the one-way coupling allows for a meaningful comparison of the bulk rain microphysics and the LD statistics because the bulk rain microphysics and the LD model are forced by the same dynamical and thermodynamical fields. The limitations and advantages of comparing two parameterizations

of which the first is fully coupled and the second is one-way coupled have recently been discussed by Grabowski (2014).

To retrieve the properties of the ambient air of an LD, trilinear interpolation from the Eulerian grid to the subgrid-scale position of the LD is used for the liquid water potential temperature, the total water mixing ratio, the pressure, the subgrid-scale velocity variance and the three components of the resolved fluid velocity. All derived variables such as the subsaturation for the calculation of evaporation are determined at the particle position from those interpolated variables.

To explore the sensitivities of the LD model to different model parameters, we ran several additional simulations each differing from the control run by one model parameter. The results are summarised in Table 3.2, which shows the accumulated surface precipitation for the whole domain and the whole simulation time, and the slope of the RSD after 30 min simulation time for cloud A and for cloud B. The slope of the RSD, Λ , is fitted for all LDs in the domain with a diameter $D > 200 \mu\text{m}$ to an exponential function: $n(D) = N_0 \exp(-\Lambda D)$ (Marshall and Palmer, 1948). In the following, we will only briefly mention sensitivities due to the choice of model parameters that are rather small (sensitivity runs 1–6), and discuss model choices that have a stronger impact on the accumulated surface precipitation and on the RSD in Sect. 3.4 in more detail (sensitivity runs 7–12).

We adapt the concept of multiplicity from the super-droplet method, i.e., one LD represents a multiplicity of raindrops of the same size. While the initial multiplicity of an LD is fixed for each run, during the LD’s lifecycle the multiplicity is allowed to change when collision-coalescence takes place. For the control run, we choose an initial multiplicity of $\xi_0 = 5 \times 10^8$. When increasing and decreasing the initial multiplicity (sensitivity runs 1–3 in Table 3.2), the slope of the RSD varies only slightly for cloud A and cloud B. The accumulated surface precipitation varies up to 30 % for cloud A and up to 20 % for the overall less sensitive cloud B.

For the initialisation of the LDs (Sect. 3.3.1) and for the selfcollection among the LDs (Sect. 3.3.4) a Monte-Carlo sampling is applied. Sensitivity runs performed with a different initial seed for the Monte-Carlo processes (sensitivity runs with * in Table 3.2) show deviations in the accumulated surface precipitation and the RSD of a similar magnitude as for the different initial multiplicities. Compared to other uncertainties, e.g., in the treatment of selfcollection (sensitivity runs 7–10), the differences in the accumulated surface precipitation and the slope of the RSD are rather small for different initial multiplicities in the range considered here and for different random seeds. For a field of clouds we expect the overall sensitivities to be smaller than the sensitivities for the isolated clouds shown here.

The initialisation of the LDs, the calculation of their trajectory, which includes inertial effect and the influence of the subgrid-scale velocity, and their mass change due to evaporation, accretion and selfcollection are described in more detail below. In the end some

Table 3.2.: Accumulated surface precipitation (R) and slope of the RSD (Λ) from the control runs and sensitivity runs for the LD model and the bulk rain microphysics scheme.

		cloud A		cloud B	
		R	Λ [mm ⁻¹]	R	Λ [mm ⁻¹]
c	control run	679 kg	14.8	3925 kg	12.2
	bulk: control run	166 %	21.3	63 %	21.3
1	$\xi_0 = 1 \times 10^9$	97 %	14.7	104 %	12.9
1*	$\xi_0 = 1 \times 10^9$	108 %	13.9	119 %	11.3
c	control run, $\xi_0 = 5 \times 10^8$	100 %	14.8	100 %	12.2
c*	$\xi_0 = 5 \times 10^8$	110 %	13.8	111 %	11.6
2	$\xi_0 = 2.5 \times 10^8$	127 %	14.1	118 %	12.0
2*	$\xi_0 = 2.5 \times 10^8$	118 %	14.1	105 %	12.6
3	$\xi_0 = 1.25 \times 10^8$	123 %	14.3	108 %	12.0
3*	$\xi_0 = 1.25 \times 10^8$	113 %	14.6	114 %	12.2
4	initial mass distr. linear decr.	84 %	14.8	95 %	11.1
5	initial mass distr. delta fct.	44 %	15.9	71 %	12.8
6	$r_{\min} = 20 \mu\text{m}$	102 %	14.6	116 %	12.4
7	selfcollection: vert. vel.	21 %	18.3	79 %	12.7
8	selfcollection: S09	118 %	14.2	112 %	11.7
9	no selfcollection	0 %	29.0	26 %	14.3
10	selfcollection: $E_c = 1$	1022 %	8.2	155 %	10.4
11	traj.: no sgs vel.	55 %	15.2	74 %	13.6
12	traj.: no inertia	120 %	14.0	110 %	11.0
I	bulk: RSD: MY05	3128 %	10.2	502 %	11.3
II	bulk: RSD: $\mu = 1$	7084 %	7.6	847 %	9.0
III	bulk: RSD: $\mu = 10$	2 %	36.7	3 %	38.2
IV	bulk: $n_c = 35 \times 10^6 \text{ m}^{-3}$	625 %	20.5	225 %	22.1
V	bulk: $n_c = 105 \times 10^6 \text{ m}^{-3}$	33 %	21.5	3 %	20.3
13	$n_c = 35 \times 10^6 \text{ m}^{-3}$	1978 %	10.5	613 %	9.5
14	$n_c = 105 \times 10^6 \text{ m}^{-3}$	1 %	18.1	8 %	12.4

For the sensitivity runs of the LD model and the bulk scheme the accumulated surface precipitation is given as percentage of the LD control run. Sensitivity runs with a different random seed for the LD model are marked with *. Sensitivity runs 7–12 are discussed in Sect. 3.4. Sensitivity runs I to V, and 13 and 14 are discussed in Sect. 3.5.

details of the technical implementation of the LD model are outlined.

3.3.1. Initialisation

The LDs are initialised proportional to the autoconversion rate given in the bulk microphysics scheme (Seifert and Beheng, 2001) for each grid box and each time step such that the mass of cloud water that is converted to rainwater in the bulk microphysics scheme equals the rainwater mass that is initialised with the LDs. We use a fixed initial multiplicity, ξ_0 , and the initial position of an LD is chosen randomly within the grid box it is

assigned to.

The distribution of the initial mass of raindrops in general depends on the pairs of cloud droplets that coalesce and form a raindrop as well as on the relative importance of condensation for the largest cloud droplets. This distribution could be analysed with the super-droplet method or a spectral bin model but so far has not been investigated to the author's knowledge. The initial mass of a raindrop is restricted between m^* and $2m^*$ where $m^* = 2.6 \times 10^{-10}$ kg is the minimal mass of a raindrop, which corresponds to a drop radius of $40 \mu\text{m}$. In the bulk microphysics scheme of Seifert and Beheng (2001), $40 \mu\text{m}$ is chosen to be the drop radius that separates cloud droplets from raindrops. We decide to use a simple initial mass distribution, and choose a uniform distribution between m^* and $2m^*$. The actual initial mass of an LD, m_0 , is then drawn randomly from this distribution. Using a uniform distribution presumably overestimates the mean initial size of the raindrops and hence underestimates the number of raindrops, which might lead to a slightly too early emergence of large raindrops for the LD model. Two sensitivity runs are performed: one with an initial LD mass distribution that decreases linearly to zero between m^* and $2m^*$ (sensitivity run 4 in Table 3.2) and one with all LDs initialised with m^* (sensitivity run 5). The development of the LD statistics is not very sensitive to the assumed initial mass distribution as long as it is allowed for some variability in the initial mass.

The average number of newly initialised LDs in a grid box is $N = A\Delta V\Delta t/M$, where A is the autoconversion rate, ΔV is the gridbox volume, Δt is the model time step and M is the average total initial mass that an LD represents. For the control run, in which a uniform distribution of the initial mass is assumed, $M = 1.5m^*\xi_0 = 195$ g. Because usually N is not a natural number, the actual number of newly initialised LDs is the largest natural number that is smaller than N , and a Monte-Carlo process is used to determine whether an additional LD is initialised that represents the decimal places of N . For instance, if $N = 5.3$, either 5 or 6 LDs are initialised and the probability that 5 LDs are initialised is 70 %.

Finally, an LD is deactivated as soon as its mass shrinks below m^* or it reaches the ground. The sensitivity for using a smaller minimum mass is small (sensitivity run 6 in Table 3.2).

3.3.2. Trajectory

The momentum equation of an LD in a gravity field is obtained from the balance of the drag force, $F_d = 1/2C_d\rho_a\pi r_{\max}^2|\vec{v}_a - \vec{v}_d|(\vec{v}_a - \vec{v}_d)$, the gravity force, $F_g = 4/3\pi r^3g(\rho_w - \rho_a)$, and the inertial force, $F_i = 4/3\pi r^3\rho_w d\vec{v}_d/dt$, giving

$$\frac{d\vec{v}_d}{dt} = \frac{1}{\tau_d}(\vec{v}_a - \vec{v}_d) - \left(1 - \frac{\rho_a}{\rho_w}\right)g\vec{e}_3 \quad (3.1)$$

$$\text{with } \tau_d = \frac{8\rho_w r^3}{3\rho_a C_d r_{\max}^2} \frac{1}{|\vec{v}_a - \vec{v}_d|} \quad (3.2)$$

Here, \vec{v} is the velocity vector of an LD and its ambient air indicated by the indices d and a , respectively. Then r is the LD's mass equivalent radius, i.e., the radius of the mass equivalent perfect sphere. To account for the flattening of large raindrops that deviate from a perfect sphere we use the approximation from Seifert et al. (2014) to specify the maximum dimension of the drop, r_{\max} . The droplet relaxation time, τ_d , depends on the drag coefficient, C_d , which in turn is a function of the Reynolds number, $N_{\text{Re}} = 2r_{\max} |\vec{v}_a - \vec{v}_d| / \nu$, i.e., depends on the drop's relative speed compared to its environmental air and on the size of the drop. The kinetic viscosity of air, ν , depends on temperature and is given by Sutherland's law (Sutherland, 1893). Furthermore, \vec{e}_3 is the unit vector in vertical direction, g gravity, ρ_w the density of water and ρ_a the density of air.

In equilibrium the LD velocity is $\vec{v}_{d,\infty} = \vec{v}_a - v_t \vec{e}_3$ with v_t being the (equilibrium) terminal fall velocity of the drop relative to the moving fluid,

$$v_t = \tau_{d,\infty} \left(1 - \frac{\rho_a}{\rho_w}\right) g \quad (3.3)$$

Note that $\tau_{d,\infty}$ itself is a function of $\vec{v}_{d,\infty}$ and \vec{v}_a (Eq. 3.2). Inertial effects can be quantified by analysing the deviation of the instantaneous LD velocity, \vec{v}_d , from its equilibrium value, $\vec{v}_{d,\infty}$. Accordingly we also define an instantaneous fall velocity, $v_f = w_a - w_d$, which may differ from the terminal fall velocity, v_t . Here, w is the vertical component of the velocity vector.

Because τ_d is small – mostly much smaller than the model time step, Δt – and slowly varying in time, Eq. 3.1 reveals properties of a stiff system and a third order Runge–Kutta scheme is not appropriate to solve numerically for \vec{v}_d . To ensure that, independent of the time step of the LES model, the momentum equation of the LD is solved robustly, i.e., without spurious oscillations in the LD velocity, we use a procedure related to the idea of an exponential integrator (Certaine, 1960). To predict the LD velocity, we first determine τ_d with a predictor-corrector method and then use the analytical solution of the momentum equation (Eq. 3.1) to predict \vec{v}_d . The momentum equation can be solved analytically assuming that τ_d and \vec{v}_a are constant for one time step and with the initial condition of $\vec{v}_d(t=0) = \vec{v}_{d,0}$ by

$$\vec{v}_d(t) = (\vec{v}_{d,0} - \vec{v}_a + \tau_d \left(1 - \frac{\rho_a}{\rho_w}\right) g \vec{e}_3) \exp\left(-\frac{t}{\tau_d}\right) + \vec{v}_a - \tau_d \left(1 - \frac{\rho_a}{\rho_w}\right) g \vec{e}_3 \quad (3.4)$$

For consistency with the Eulerian model, we update the LD position with a third order Runge–Kutta scheme that considers the variability of \vec{v}_a . For a comparison of numerical methods, see Appendix C.

Such a mixed approach of an analytical solution for the LD velocity with a predictor-

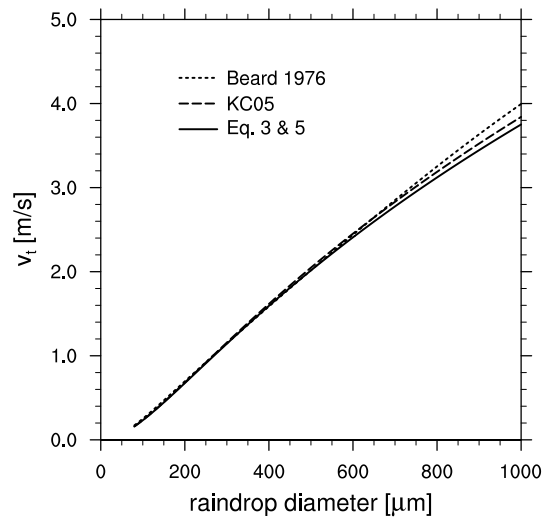


Figure 3.1.: Terminal fall velocity for surface conditions of a standard atmosphere according to Eq. 3.3 and Eq. 3.5, and after Khvorostyanov and Curry (2005, KC05), and Beard (1976).

corrector procedure for τ_d , and a third order Runge–Kutta scheme for the LD position is equal to the analytical solution with the predictor–corrector method if \vec{v}_a is constant during each time step. Asymptotically, if the mass of the drop vanished, τ_d and v_t approach zero and \vec{v}_d is equal to \vec{v}_a , i.e., the result is equal to the third order Runge–Kutta scheme for a massless particle.

Following Abraham (1970), a good approximation of C_d is given by

$$C_d = C_0 \left(1 + \frac{\delta_0}{\sqrt{N_{\text{Re}}}} \right)^2 \quad (3.5)$$

with $C_0 = 0.29$ and $\delta_0 = 9.06$. For small N_{Re} , it follows that $C_d = C_0 \delta_0^2 / N_{\text{Re}} = 24 / N_{\text{Re}}$, which matches the solution for the Stokes regime. For large raindrops, the flattened shape of the raindrop deviating from a perfect sphere and a turbulence correction of C_d should be considered (e.g., Khvorostyanov and Curry, 2002; 2005). For $r = 500 \mu\text{m}$ the difference between the terminal fall velocity according to Eq. 3.3 and Eq. 3.5, and the terminal fall velocity from Khvorostyanov and Curry (2005) is 9 cm/s, i.e., less than 3 % (Fig. 3.1). Compared to the semi-empirical formulas from Beard (1976), the difference is 24 cm/s for $r = 500 \mu\text{m}$, i.e., less than 7 %. Because in this study the raindrops are mostly smaller, we neglect such corrections on \vec{v}_t and use C_d as written in Eq. 3.5. Therefore C_d is used consistently with Eq. 3.1 and Eq. 3.2 and also takes into account deviation from its equilibrium value, which can be caused by the LD velocity deviating from its terminal fall velocity due to inertial effects.

The fluid velocity that an LD feels is composed of two parts, the resolved fluid velocity of the ambient air and the subgrid-scale contribution: $\vec{v}_a = \vec{v}_{\text{res}} + \vec{v}_{\text{sgs}}$. The subgrid-scale velocity is calculated once every time step according to the approach from Weil et al.

(2004), which has been developed for stationary, homogeneous and isotropic turbulence, and non-interacting particles. Weil’s prognostic equation for a Gaussian random subgrid-scale velocity forcing is based on the unresolved turbulent kinetic energy, which in turn is calculated by the Smagorinsky–Lilly model in UCLA-LES.

The Lagrangian subgrid-scale model from Weil et al. (2004) has been applied to massless, non-interacting Lagrangian particles in LES, e.g., to study mixing and entrainment in the convective boundary layer (Heus et al., 2008; Yamaguchi and Randall, 2012). However, the model has limitation when being applied to interacting Lagrangian drops. For a pair of particles Weil’s assumption of a random, uncorrelated subgrid-scale contribution to each particle’s velocity becomes invalid if small separation distances between particles are considered, e.g., for point sources (Bec et al., 2010). In contrast an identical subgrid-scale contribution for particle pairs with a negligible separation distance would neglect inertial effects. Using the concept of multiplicity, the actual LD concentration is lower than the raindrop concentration in a cloud. If the multiplicity was drastically reduced, i.e., the LD concentration increased, neglecting the subgrid-scale velocity correlation of particle pairs possibly alters the convergence behaviour of the LD model.

For the control run, we include the subgrid-scale contribution according to Weil et al. (2004). In addition, we perform a sensitivity run in which the subgrid-scale contribution to the LD’s momentum equation is neglected and we discuss the effect of an uncorrelated subgrid-scale velocity on the collision rate in Sect. 3.4.

3.3.3. Evaporation and accretion

For the calculation of evaporation, we follow Mason (1971, p. 123) and additionally include the effect of ventilation

$$\left. \frac{dm}{dt} \right|_{\text{evap}} = f_v 4\pi r \rho_w \frac{(S - 1)}{(F_h + F_v)} \quad (3.6)$$

where $S - 1$ is supersaturation, F_h describes conduction of heat and F_v describes diffusion of water vapor. The factor f_v represents the effect of ventilation according to Beard and Pruppacher (1971) and Pruppacher and Rasmussen (1979), and depends on N_{Re} and on the Schmidt number for water vapour, $N_{\text{Sc}} = \nu/D_v$, with $D_v = 2.5 \times 10^{-5} \text{ m}^2/\text{s}$ being the diffusivity of water vapour. In this approach the effects of curvature and solution are neglected as well as kinematic and statistical, non-stationary growth effects, which is a reasonable assumption for raindrops of the sizes considered (e.g., Rogers and Yau, 1989, p. 103 and 112). For raindrops the growth rate due to condensation is typically much smaller than the growth rate due to accretion and is not taken into account here.

For accretion a continuous model of collection growth is used (Pruppacher and Klett, 1997, p. 617). For the model to be valid, it is assumed that the collected cloud droplets are much smaller than the collector raindrop, i.e., that the cloud droplet fall velocity is much

smaller than the raindrop fall velocity, and that the raindrop number density (typically $< 1 \text{ cm}^{-3}$) is much smaller than cloud droplet density (typically 100 cm^{-3}). Then the mass gain due to accretion is given by:

$$\left. \frac{dm}{dt} \right|_{\text{accr}} = E_c \pi \rho_a r_{\text{max}}^2 |\vec{v}_d - \vec{v}_a| q_c \quad (3.7)$$

where m is the raindrop mass, q_c is the ambient cloud water mixing ratio and the collision-coalescence efficiency, E_c , is set to unity. For maritime clouds with relatively large cloud droplets $E_c = 1$ is justified but a parametrisation of E_c as a function of the cloud droplet size distribution should to be considered if the typical cloud droplet size is smaller.

3.3.4. Selfcollection

Selfcollection of raindrops is important if the raindrop number density is high. Using a bulk microphysics scheme, Stevens and Seifert (2008) found that also for lightly precipitating shallow cumulus clouds selfcollection has an important effect on the precipitation amount. For a raindrop distribution, selfcollection overall reduces the number of raindrops but conserves the rainwater mass. Hence for the LD model, selfcollection redistributes mass among the LDs and reduces their multiplicity. The formulation of selfcollection for the LD model consists of two steps: first it is defined how a pair of LDs coalesces and second the probability of selfcollection is determined depending on this definition.

Concerning the first step of how LDs coalesce, we closely follow the approach of Shima et al. (2009). For the selfcollection of a pair of LDs (j, k), the LD with the lower multiplicity retains its multiplicity while gaining mass and the LD with the higher multiplicity retains its mass while its multiplicity is lowered. For multiplicities ξ_j and ξ_k , where $\xi_j \neq \xi_k$ and without loss of generality $\xi_j < \xi_k$, the properties of the LDs after a selfcollection event (dashed variables) are

$$\xi'_j = \xi_j, \quad \xi'_k = \xi_k - \xi_j, \quad (3.8)$$

$$m'_j = m_j + m_k, \quad m'_k = m_k \quad (3.9)$$

For $\xi_j = \xi_k$

$$\xi'_j = \text{floor}(\xi_j/2), \quad \xi'_k = \xi_k - \text{floor}(\xi_j/2), \quad (3.10)$$

$$m'_j = m_j + m_k, \quad m'_k = m_j + m_k \quad (3.11)$$

For the second step, to determine the probability of selfcollection of a pair of LDs, we follow the approach of Sölch and Kärcher (2010) who suggest an algorithm for selfcollection that takes into account the vertical position of the LDs. Only if the difference between the vertical velocities of the LDs times the time step is larger than vertical distance between

the LDs, selfcollection may take place. We consider all LD pairs within one grid column, i.e., we consider LDs falling across vertical grid box boundaries, but not across horizontal grid box boundaries. Collisions of a pair of LDs may occur within one model time step, Δt , if

$$0 < \frac{z_j - z_k}{w_{d,k} - w_{d,j}} \leq \Delta t \quad (3.12)$$

where z is the vertical position of the LD and w_d its vertical velocity. If this criteria is met and if a homogeneous distribution of raindrops in the horizontal of one grid box column is assumed, the probability for selfcollection for each pair of LDs (j, k) , P_{jk} , is given by

$$P_{jk}^{\text{CTRL}} = \frac{\max(\xi_j, \xi_k)}{\Delta x \Delta y} E_c \pi (r_j + r_k)^2 \frac{|\vec{v}_{d,j} - \vec{v}_{d,k}|}{|w_{d,j} - w_{d,k}|} \quad (3.13)$$

where Δx and Δy are the horizontal dimensions of a grid box and $\pi(\Delta r)^2 |\Delta \vec{v}_d| / |w_d|$ is the projected sweep area of the raindrops. The last factor of Eq. 3.13, $|\Delta \vec{v}_d| / |\Delta w_d|$, approaches one if the vertical component of the LD velocities dominates the velocity difference of a pair of LDs. We use this formulation of LD selfcollection given in Eq. 3.8–3.13 for our control runs.

Alternatively, it may also be assumed that the raindrops an LD is representing are distributed homogeneously within one grid box not only in the horizontal but also in the vertical. This follows the ideas of Shima et al. (2009, S09) except for their Monte-Carlo sampling of super-droplet pairs, which we do not apply. Then the probability of selfcollection for each pair of LDs (j, k) that is located in the same grid box is

$$P_{jk}^{\text{S09}} = E_c \frac{\max(\xi_j, \xi_k)}{\Delta x \Delta y \Delta z} \pi (r_j + r_k)^2 \Delta t |\vec{v}_{d,j} - \vec{v}_{d,k}| \quad (3.14)$$

where Δz is the vertical size of a grid box and $\pi(\Delta r)^2 \Delta t |\Delta \vec{v}_d|$ is the sweep volume of the raindrops. Again, in case that the vertical velocity difference dominates the velocity difference of a pair of LDs, the last factor, $|\Delta \vec{v}|$, could be replaced by the vertical velocity difference, $|\Delta w|$. The assumption of homogeneously distributed raindrops within each grid box, may overestimate the probability for selfcollection, if due to gravitational sorting and raindrop growth heavier (i.e. larger) drops tend to be positioned lower within a grid box. If heavier drops are positioned lower in a grid box, they are not able to capture the smaller drop above them according to P_{jk}^{CTRL} (Eq. 3.13) but are considered in P_{jk}^{S09} (Eq. 3.14). We will show later in Sect. 3.4, that the horizontal velocity difference of a pair of LDs contributes noticeably to their total velocity difference and that the effect of gravitational sorting in a grid box on the selfcollection can indeed be neglected in the cases considered.

For both approaches, P_{jk}^{CTRL} and P_{jk}^{S09} equal the expected value of the selfcollections of $\min(\xi_j, \xi_k)$ pairs of real drops. However, due to the rather small number of LDs (compared

to the number of raindrops in a real cloud) the variance of the number of coalesced pairs is overestimated by the LD model (for a detailed discussion of the expectation value and variance see Shima et al., 2009).

For selfcollection it is not justified to set the collision-coalescence efficiency, E_c , to unity. Instead the coalescence efficiency depends on the raindrop size and is determined following the measurements of Beard and Ochs (1995). Using such a parametrisation for E_c can also be understood as an attempt to take raindrop breakup into account, i.e., be interpreted as a pair of raindrops rebounding from each other without changing their masses. For raindrops larger than those considered here, filament breakup becomes an important process (Low and List, 1982; Seifert et al., 2005; Straub et al., 2010) but is not taken into account in this study.

We use a Monte-Carlo sampling to determine whether two LDs, that have the probability P_{jk} to collide, do collide in the model.

The position and the velocity of the LDs are assumed to remain unchanged directly after selfcollection.

3.3.5. Implementation

The LDs are implemented as a linked list of particles with several properties. For each processor a maximum length of the list is specified a priori and represents a “reservoir” of LDs. From that reservoir particles are activated as LDs according to the autoconversion rate on that part of the grid that the particular processor represents. When LDs leave the spatial domain of the processor, they are passed to the linked list of the processor they enter. Once an LD is deactivated, because it shrinks below a threshold or reaches the surface, it is passed back to the linked list of its home processor. There, it is available for activation again. To distinguish the former LD (and its trajectory) from the newly activated one, each LD has a property called *drop number*, which is increased by a value of one if a new LD is activated. To find potential pairs of LDs for selfcollection more effectively, the LDs are also sorted and linked on an additional three dimensional variable spanning the spatial grid.

The fixed reservoir size per processor, which is specified before starting the model, has only become necessary due to limitations in the output to NetCDF. Before particle output is written all particles are passed back to their home processor so that the number and order of particles for each output time step is fixed. Using such a static array for writing data ensures an efficient output routine while the usage of a linked list in principle allows for a dynamic internal memory management. Particle properties are written to disk every 15 s of simulation time to be able to analyse an LD’s trajectory and growth history. For each particle 22 variables are saved. Ten of them give properties of the LD: the drop number, the mass and multiplicity, the relaxation timescale, the three components of the

LD position in space, and the three velocity components of the instantaneous LD velocity. In addition 12 properties of the flow at the LDs position are saved: the three components of the fluid velocity and the three components of the subgrid-scale contribution to the fluid velocity, the potential temperature, the virtual potential temperature, the cloud liquid water, the total water, the dissipation rate and the pressure.

The computational overhead of the LD model depends on the number of particles per reservoir and on the number of active LDs. The runs analysed in this chapter are all run on 32 processors and most of them use a reservoir which corresponds to 2 particles per grid box, i.e., depending on the domain size there are about 1.5×10^5 particles available per processor or roughly 5×10^6 particles for the whole domain. For the sensitivity run with quartered initial multiplicity, the number of particles is doubled, i.e., there are 4 particles in the reservoir per grid box. Without the LD model one LES run needs about 1800 CPU hours, for the runs with the LD model and 2 LDs per grid box about 3400 to 3800 CPU hours are consumed and for 4 LDs per grid box 4800 CPU hours are needed. Therefore the computational overhead due to the LD model is typically about 100 % for the runs performed for this chapter. Nevertheless, the limiting factor for these simulations is mostly the available disk space for the output of all LDs, not the actual CPU time consumed for the run. However, the LD model is not coded for optimisation, it might therefore be possible to reduce computational cost rather easily.

3.4. Resolved and subgrid-scale turbulent velocity fluctuations and their effect on collision frequency

While sensitivities to some assumptions of the LD model such as the initial multiplicity, the initial mass distribution or the minimum mass are rather small for a reasonable range of parameters (sensitivity runs 1–6 in Table 3.2), we find that the LD model shows a more pronounced sensitivity to the treatment of selfcollection. Besides the radius and the multiplicity, the selfcollection rate depends on the velocity difference between a pair of LDs (Sect. 3.3.4). Therefore, we first discuss the impact of inertial effects on the LD's velocity, and then expand the discussion on effects that impact the collision probability such as the subgrid-scale velocity.

To analyse the effect of inertia on the instantaneous vertical drop velocity we define the normalised vertical velocity deviation of an LD, $\Delta w/v_t = (w_d - w_a + v_t)/v_t$, which characterises the strength of inertial effects on the raindrop velocity and is zero if inertial effects are negligible, i.e., if the instantaneous fall velocity is equal to the fluid velocity minus the terminal fall velocity. For the control run, the normalised vertical velocity deviation is rarely as large as 20 % and is less than 5 % more than 90 % of the time (Fig. 3.2). Neglecting the subgrid-scale contribution of the fluid velocity on the LD's momentum equation narrows the distribution of the normalised vertical velocity deviation

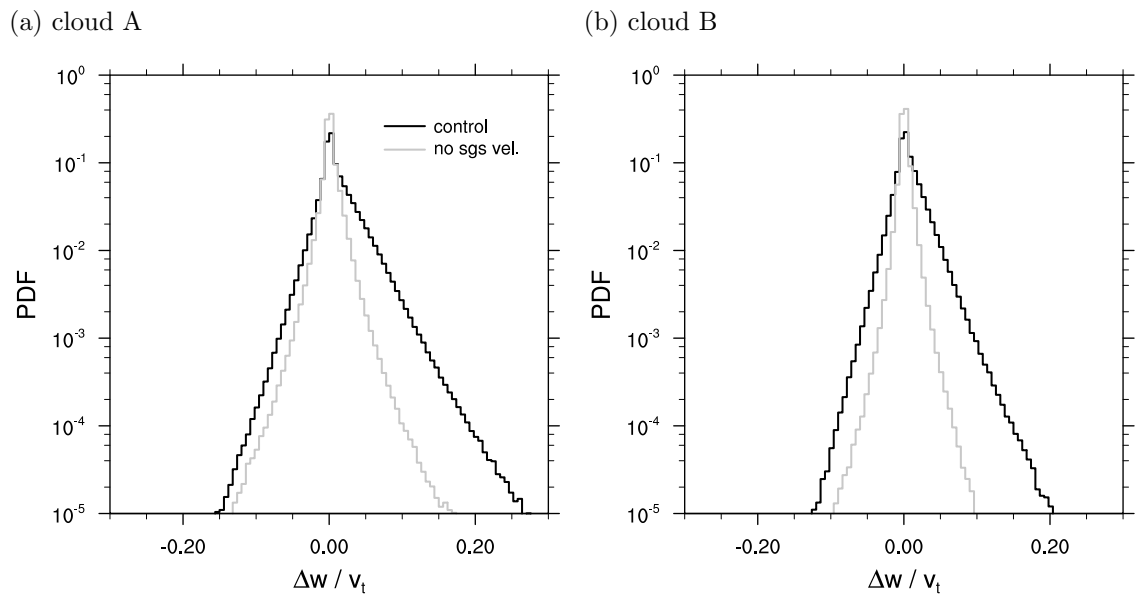


Figure 3.2.: Normalised vertical velocity deviation, $\Delta w/v_t = (w_d - w_a + v_t)/v_t$. Values are positive if the LD is falling down slower than its equilibrium terminal fall velocity would suggest; for negative values the LD is falling faster.

of an LD even further.

Observations of more heavily precipitating cases have found that *superterminal* raindrops, i.e., raindrops that fall faster than their terminal fall velocity ($\Delta w/v_t < 0$), are abundant for raindrop diameters < 1 mm (Montero-Martínez et al., 2009; Larsen et al., 2014). Montero-Martínez et al. (2009) suggest that those superterminal raindrops are caused by the breakup of very large raindrops, whose fragments directly after the breakup event still fall with the higher fall velocity of the original raindrop and then slow down with time by relaxing to their own terminal fall velocity. To be able to investigate the occurrence of such a mechanism with the LD model, a detailed formulation for breakup of large raindrops still has to be included in the LD model. From our current simulations we find no evidence for a large fraction of superterminal raindrops.

The rather small effect of inertia on the LD's velocity observed in this study is consistent with the values of the Stokes number of the LDs, $St = \tau_d/\tau_\eta$, where $\tau_\eta = \sqrt{\nu/\epsilon}$ is the Kolmogorov timescale and ϵ the dissipation rate (calculated as described in Stevens et al., 1999). For large Stokes numbers the LD relaxation timescale, τ_d , is larger than the Kolmogorov timescale, τ_η , and inertial effects are important. The Stokes number is > 1 for 18 % of the LDs in cloud A and for only 6 % of the LDs in cloud B (Fig. 3.3). Stokes numbers > 5 are very rare (0.28 % for cloud A and 0.01 % for cloud B). Although the relaxation timescale is increasing almost linearly with the LD diameter for the range considered, the spread in Stokes numbers is large because LDs of different size do not sample the three-dimensional domain homogeneously. Small LDs dominate regions with

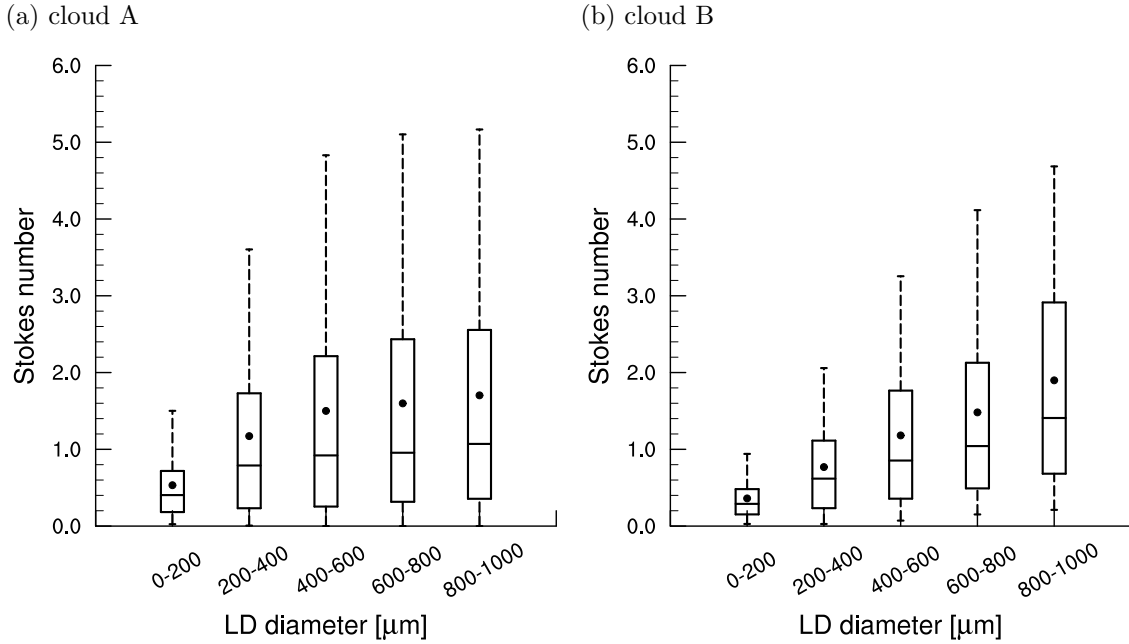


Figure 3.3.: Boxplot of the Stokes number of the LDs as a function of the LD diameter. The whiskers and the boxes mark the 5 %, 25 %, 50 %, 75 % and 95 % percentiles, and the dots mark the mean.

high dissipation rates near cloud top where the autoconversion rate is high. In contrast, large LDs are often located in less turbulent regions with low dissipation rates both inside the cloud and outside the cloud in the environmental air.

To investigate the effects of velocity deviations due to inertial effects in the LD’s momentum equation (Eq. 3.4) on the development of the RSD, we perform a sensitivity run where instead of applying a relaxation timescale, τ_d , the LD’s velocity is simply set to $\vec{v}_d = \vec{v}_a - v_t \vec{e}_3$, i.e., explicit inertial effects are neglected in the momentum equation (“traj.: no inertia” in Fig. 3.4, sensitivity run 12 in Table 3.2). Because the fluid velocity, \vec{v}_a , is the sum of the resolved fluid velocity and a contribution from the Lagrangian subgrid-scale model, this setup still allows for velocity differences between a pair of LDs at the same location due to the subgrid-scale contribution. Compared to the control run, the RSD and the surface precipitation rate do not differ noticeably. This implies that the effect of the vertical velocity deviations as shown in Fig. 3.2 (i.e., the difference between the control run and a delta function at zero) and of the corresponding horizontal velocity deviations on the LD growth is small.

The horizontal velocity difference of two LDs that are located close to each other is increasing with increasing separation distance (Fig. 3.5). This has implication for the representation of selfcollection in the LD model: Using the concept of multiplicity, collision probabilities in the LD model are calculated for all LD pairs that are located within the same grid box (Eq. 3.14; or within the same column and within a vertical distance that

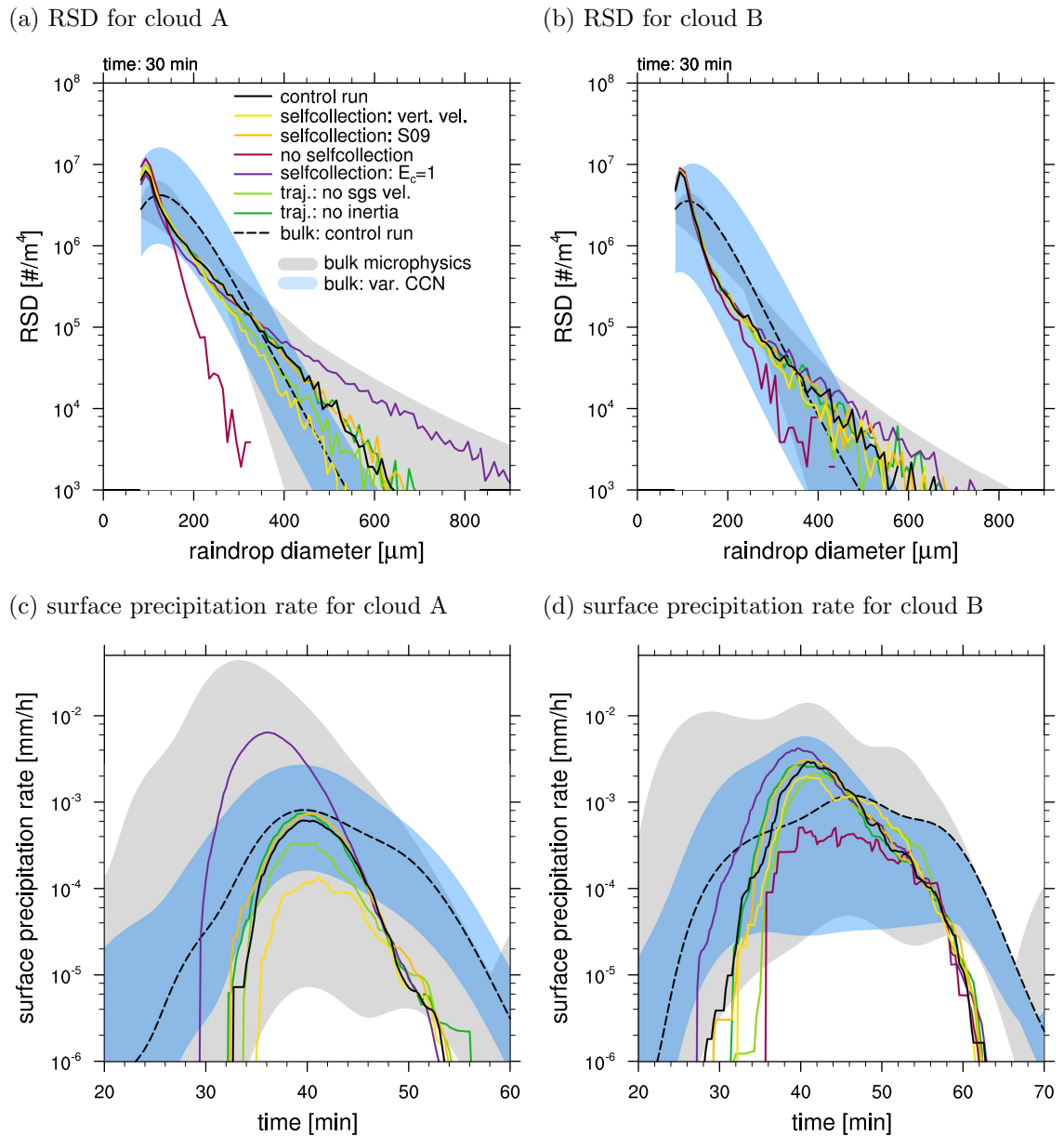


Figure 3.4.: RSD and 2-min running average of the surface precipitation rate for the control run and selected sensitivity runs. The grey area indicates the uncertainties in the bulk rain microphysics scheme due to the choice of the shape parameter of the RSD (see Sect. 3.5 for explanation). The blue area gives the sensitivity of the bulk scheme to decreasing and increasing the cloud droplet density by 50 %.

is defined by their vertical velocity difference, Eq. 3.12 and Eq. 3.13). Real raindrops, however, only collide if they meet at the same position. Because collisions are considered for LD pairs within a grid box regardless of their separation distance, the horizontal velocity difference of a pair of LDs is overestimated for the collision rate in the LD model. However, due to inertial effects we do not expect the horizontal velocity difference to be

zero either.

A second issue concerning the velocity difference of a pair of LDs for the collision rate arises from the use of a Lagrangian subgrid-scale model. The subgrid-scale contribution to the fluid velocity directly influences the LD's trajectory via its momentum equation but also impacts the relative velocity difference between a pair of LDs and therefore the collision rate (Eq. 3.13, Eq. 3.14). Switching off the subgrid-scale contribution for a sensitivity run ("traj.: no sgs vel.", Fig. 3.5 c and d), the average horizontal velocity difference of a pair of LDs is smaller than for the control run that includes the subgrid scale contribution (Fig. 3.5 a and b). Including the subgrid-scale contribution we find that the horizontal velocity difference is higher especially for those pairs of LDs that are located close to each other. Here, the horizontal velocity difference is probably overestimated by the subgrid-scale model from Weil et al. (2004) because the subgrid-scale model neglects velocity correlations among LD pairs (see Sect. 3.3.2 Yang et al., 2008; Wang et al., 2009).

Recent super-droplet studies treat both issues differently. They either neglect the subgrid-scale contribution on the collision rate (Shima et al., 2009; Andrejczuk et al., 2010) or include it in an average sense by using a mean field approach derived from direct numerical simulations rather than a statistical approach for collision-coalescence (Riechelmann et al., 2012). All three studies assume collisions of super-droplets within a certain volume. In the collision kernel Shima et al. (2009) include horizontal velocity differences of a pair of super-droplets and assume that the super-droplet's fall velocity equals its terminal fall velocity. Andrejczuk et al. (2010) consider only the vertical velocity difference of a pair of super-droplets.

To explore both the effect of the subgrid-scale contribution on the collision rate and the effect of the separation distance on the horizontal velocity difference (and thereby on the collision rate), we compare three simulations. In the control simulations, the Lagrangian subgrid-scale model with the uncorrelated velocity differences is used, and the horizontal velocity difference of a pair of LDs contributes to the collision probability. Two sensitivity runs are performed: In the first one the subgrid-scale contribution to the LD velocity is neglected ("traj.: no sgs vel." in Fig. 3.4, sensitivity run 11 in Table 3.2), which underestimates the collision rate in that respect. In the second one the subgrid-scale model is applied, but only the vertical velocity difference of a pair of LDs is considered for the collision rate ("selfcollection: vert. vel.", sensitivity run 7), which also underestimates the collision rate because the contribution of the horizontal velocity difference is neglected. For both sensitivity runs the surface precipitation is notably reduced for cloud A (to 55 % and to 21 %, respectively) and the RSDs are narrower compared to the control simulation.

To quantify these effects in the collision kernel, we analyse the vertical velocity difference of an LD pair normalised by the magnitude of its three-dimensional velocity vector (Fig. 3.6). If the masses of an LD pair differ substantially, the velocity difference of a pair of LDs is dominated by the sedimentation velocity difference, i.e., the normalised verti-

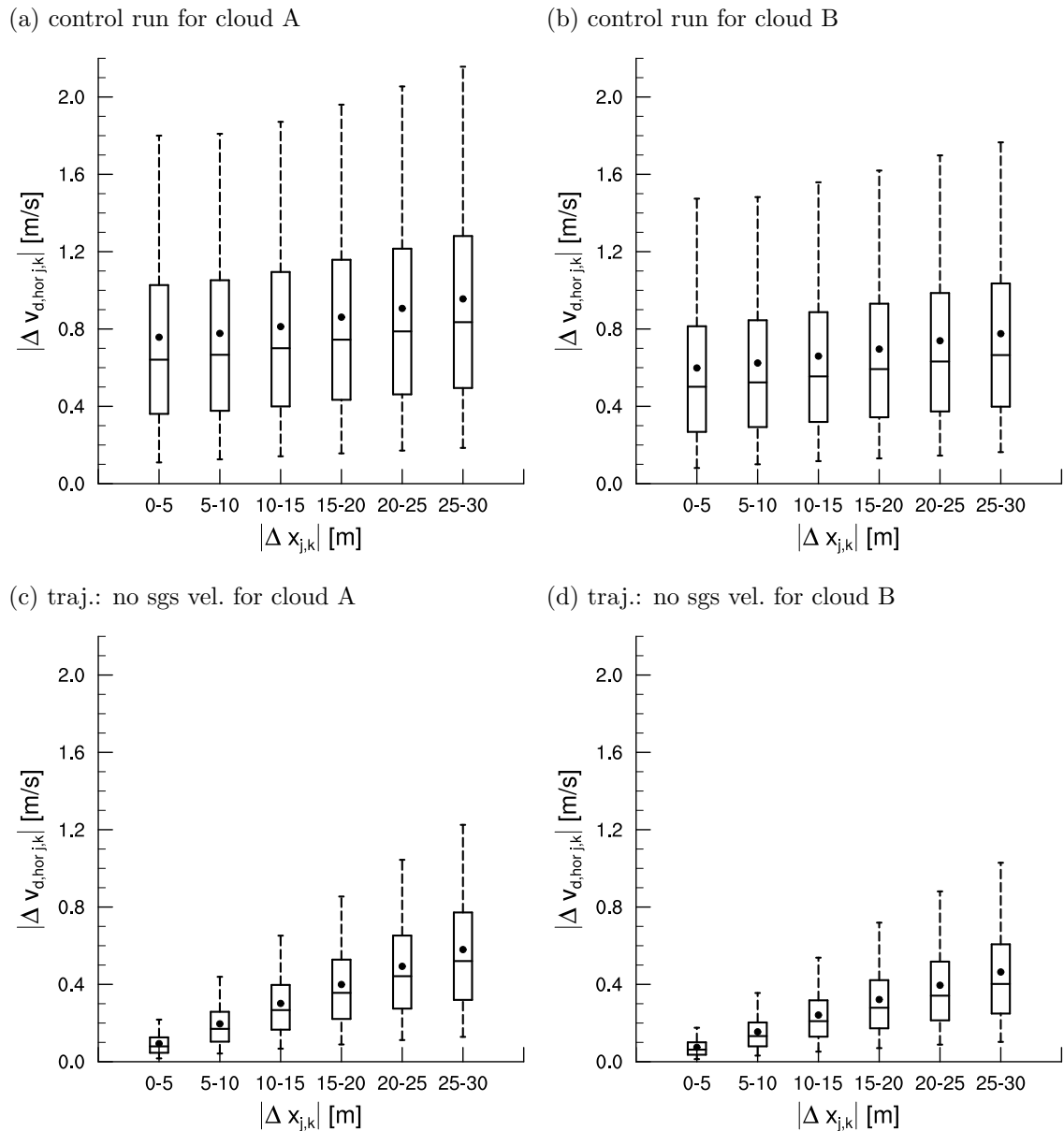


Figure 3.5.: Boxplot for the horizontal velocity difference of pairs of LDs that are located in the same grid box as a function the LD separation distance. The whiskers and the boxes mark the 5 %, 25 %, 50 %, 75 % and 95 % percentiles, and the dots mark the mean.

cal velocity difference is close to one. For small mass differences, the horizontal velocity difference may also contribute noticeably to the three-dimensional velocity difference and therefore the normalised vertical velocity difference is substantially lower.

For both the control run and the sensitivity run without the Lagrangian subgrid-scale model, the spread in normalised vertical velocity difference is high. For the control run the average normalised vertical velocity difference is about 55 %, i.e., using only the vertical velocity difference instead of the three-dimensional one, such as it is done in a classical

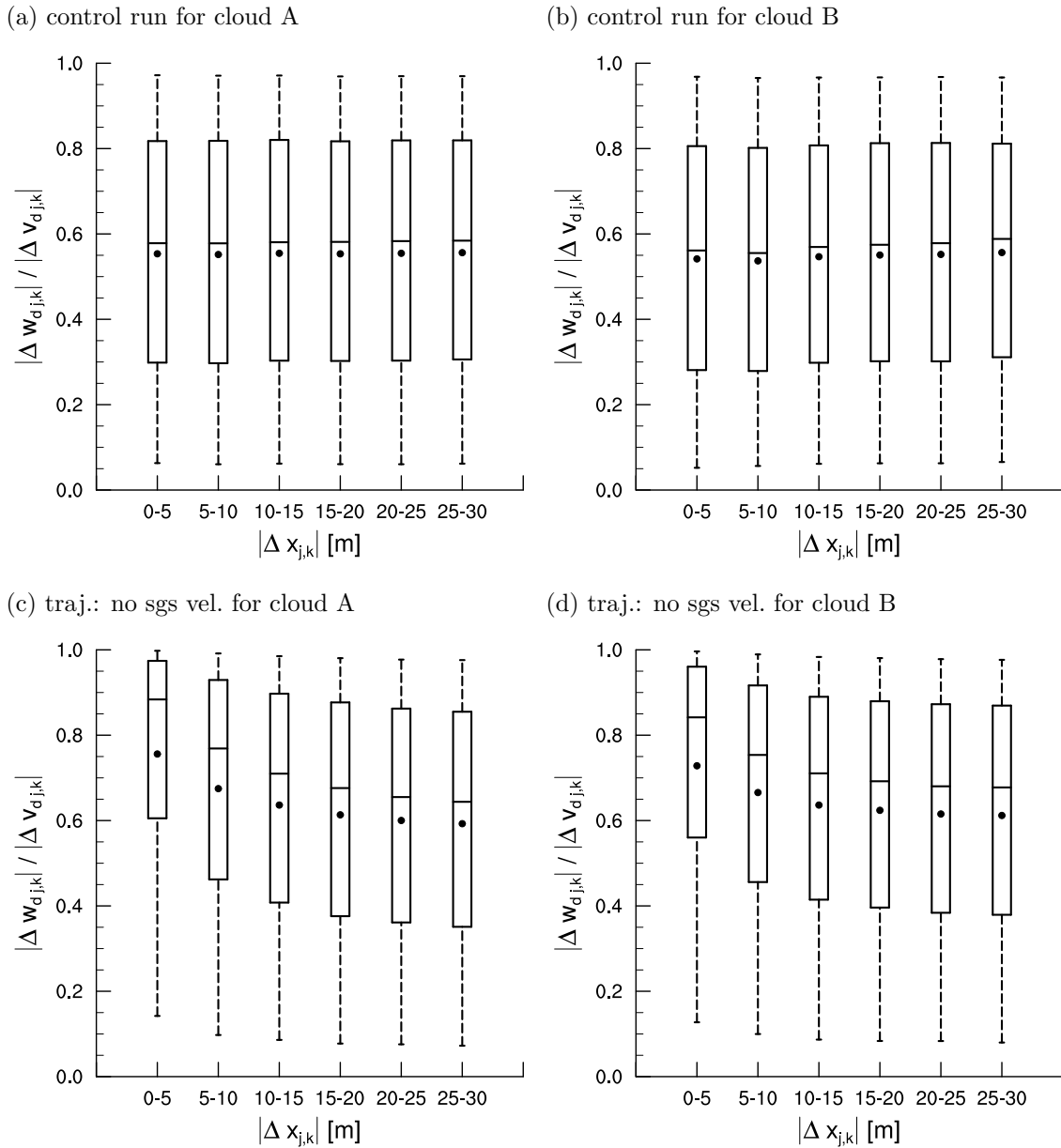


Figure 3.6.: As Fig. 3.5 but for the vertical velocity difference of LD pairs normalised by the magnitude of the three-dimensional velocity vector.

gravitational kernel, on average reduces the collision rate by 45 % compared to the control run. Without the Lagrangian subgrid-scale model the average normalised vertical velocity difference is about 5 % higher than for the control run and increases with decreasing separation distance.

This leads us to the conclusion that both the subgrid-scale contribution of the fluid velocity as well as the horizontal velocity difference, which is connected to the separation distance of a pair of LDs, do have a noticeable effect on the collision rate. All variants

discussed here (the control run, the sensitivity runs “traj.: no sgs vel.” and “selfcollection: vert. vel.”) have their issues and it is not obvious which implementation is most realistic leaving us with a considerable uncertainty in the formulation of the selfcollection of the LDs. Therefore both effects should be explored further, e.g., by using a Lagrangian subgrid-scale model that includes correlation statistics for particles that are located close to each other (Mazzitelli et al., 2014b).

The assumption of a vertically homogeneous distribution of raindrops within one grid box (Shima et al., 2009, “S09”) instead of taking their vertical position into account (Sölch and Kärcher, 2010) does not have a distinct effect for cloud A or cloud B. Therefore gravitational sorting within one grid box is not important for selfcollection in this case.

While all the sensitivity analyses above are physically reasonable and give an estimate of the uncertainty in the LD model, two further sensitivity runs make rather crude simplifications and again highlight the importance of the selfcollection process: neglecting selfcollection altogether (“no selfcollection” in Fig. 3.4, sensitivity run 9 in Table 3.2) results in a very narrow RSD and the absence of surface precipitation for cloud A. A constant collision-coalescence efficiency equal to unity (“selfcollection: $E_c = 1$ ”, sensitivity run 10) results in a very broad RSD and a large increase in surface precipitation.

For cloud B the tested sensitivities are consistent in sign with cloud A but overall lower in magnitude, both for the RSD and for the surface precipitation rate (Fig. 3.4 and Table 3.2). Because cloud B has a more complex and overall longer lifecycle showing features of pulsating growth, we speculate that this less sensitive behaviour is related to a microphysical buffering that compensates for changes, e.g., in selfcollection. Large normalised vertical velocity deviations and large Stokes numbers are even less numerous for cloud B than for cloud A due to an overall less vigorous lifecycle.

3.5. Assessment of the bulk microphysics scheme

For both cloud A and cloud B, the LD statistics show some agreement with the bulk rain microphysics control run, which uses the closure equation of Seifert (2008) for the shape parameter of the RSD (“bulk: control run” in Fig. 3.4 and Table 3.2). In the two-moment bulk microphysics scheme from Seifert and Beheng (2001) the RSD is assumed to follow a gamma distribution in terms of the raindrop diameter. Because the gamma distribution has three free parameters and only two of those can be determined from the prognostic moments of the parametrisation, a closure equation for the third parameter, usually the shape parameter, is needed. To set the sensitivities of the LD model in context to the uncertainties in the bulk rain microphysics scheme, a set of four Eulerian simulations is run. Each simulation has been started from the same initial conditions and with the same Eulerian model setup as described in Sect. 3.2.1 despite a change in the closure equation that determines the shape of the RSD in the bulk scheme. In addition to the control

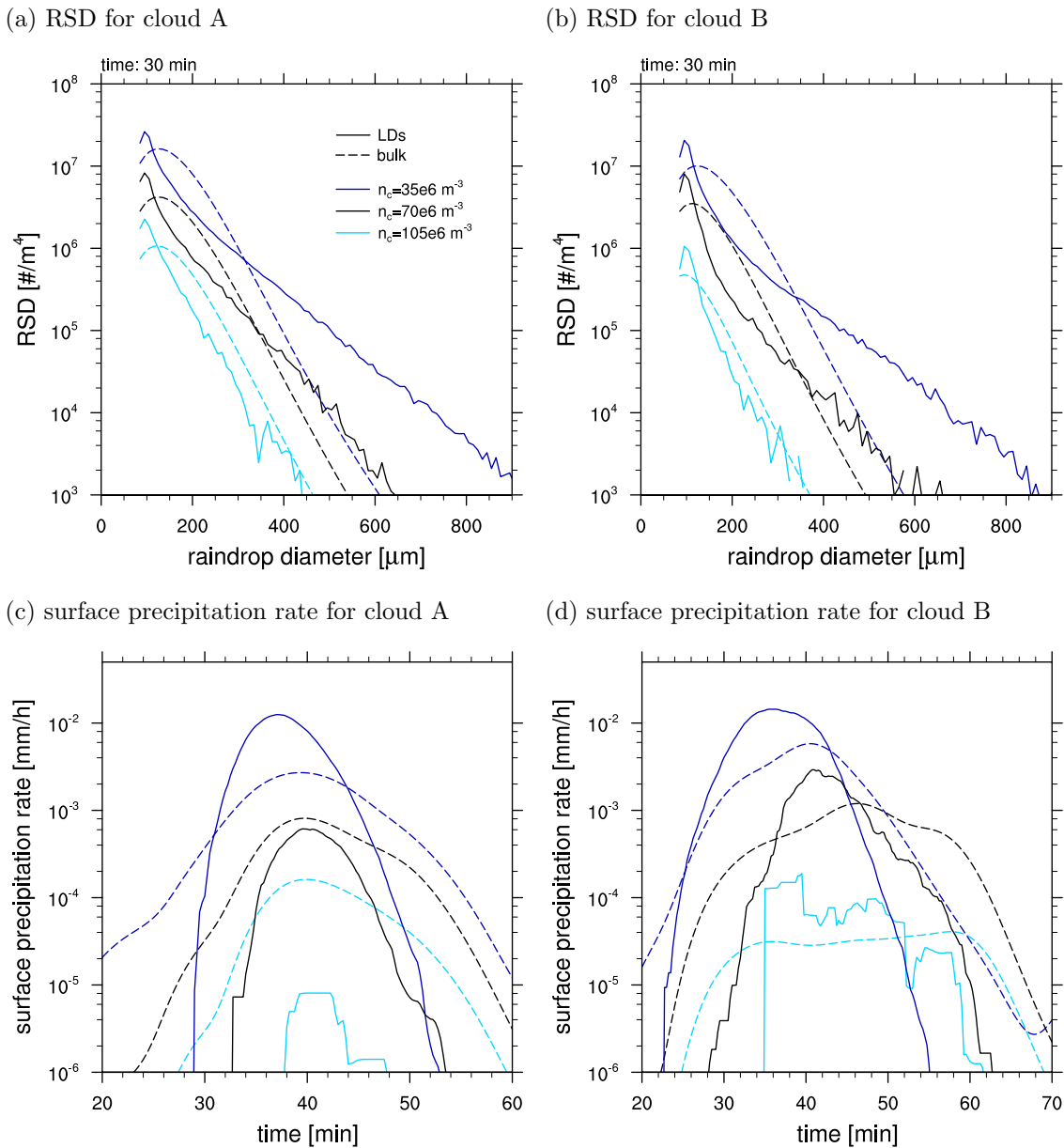


Figure 3.7.: RSD and 2-min running average surface precipitation rate for different assumptions of the cloud droplet number density, n_c .

run, which uses the closure equation from Seifert (2008), three simulation are run: one using the closure equation suggested by Milbrandt and Yau (2005, MY05), one using a constant shape parameter equal to 1 and one using a constant shape parameter equal to 10. Considering the uncertain knowledge about the value of the shape parameter, besides the relations from Seifert (2008) and Milbrandt and Yau (2005) also a constant value of 1 and a constant value of 10 are plausible choices (Stevens and Seifert, 2008). In Fig. 3.4 the uncertainty in the RSD and the surface precipitation rate due to the choice of the shape parameter in the bulk scheme is given as a grey shading and only the control run is shown

explicitly (dashed line). From Fig. 3.4 and Table 3.2 (sensitivity run I–III) it can be seen that the uncertainty range of the bulk scheme due to the choices for the shape parameter of the assumed RSD is much larger than the uncertainty in the LD model.

An additional uncertainty of the bulk scheme lies in the treatment of the cloud droplet number density, n_c . In the bulk scheme n_c is assumed to be constant in space and time, and aerosol effects are often studied by varying n_c (e.g., Savic-Jovicic and Stevens, 2008). If n_c is decreased and to a first order it is assumed that the cloud water content is constant, the mean cloud droplet diameter and the autoconversion rate increase, i.e., more cloud water is converted to rainwater. In our control run $n_c = 70 \times 10^6 \text{ m}^{-3}$ is prescribed in accordance with the RICO case setup (van Zanten et al., 2011). When decreasing n_c by 50 %, the rainwater content is increasing (and vice versa for increasing n_c) but the slope of the RSD in the bulk scheme does not vary much (Fig. 3.7 and sensitivity runs IV–V in Table 3.2). For the LD model, the tail of the RSD flattens with decreasing n_c (sensitivity run 13–14), i.e., with increasing rainwater content the number of large raindrops increases disproportionately strong, probably due to more efficient selfcollection. Therefore with decreasing n_c , the surface rain rate also increases more for the LD model than for the bulk scheme.

Overall, the uncertainty of the LD model, e.g., for the treatment of selfcollection, is smaller than the n_c sensitivity in both the bulk scheme and the LD model. The uncertainty of the bulk scheme due to the choice of the shape parameter of the RSD is at least as large as the impact of n_c .

3.6. Conclusions

We introduced an LD model to study warm rain microphysical processes. The LD model presented here is closely related to the super-droplet method and applies their concept of multiplicity but instead of trying to represent the whole drop size distribution it simulates the raindrop phase only, making the problem computationally more feasible. The LDs are initialised proportional to the autoconversion rate of the bulk microphysics scheme to assure that the same amount of rainwater is initialised in the bulk scheme and in the LD model. All relevant microphysical processes – accretion of bulk cloud water, selfcollection among the LDs and evaporation in subsaturated air – are included so that the mass of an LD develops according to its environment. The momentum equation for each LD includes dynamical effects such as sedimentation and inertia, and a contribution from the parametrised subgrid-scale fluid velocity.

The LD model is intended to be used as a tool to understand warm rain microphysical processes in shallow cumulus on a particle-based level. In the present study, we test whether the model is fit for purpose. We therefore conduct a sensitivity study of two isolated shallow cumulus clouds that are simulated with LES including a bulk microphysics

parametrisation and with the LD model for raindrop growth without feedbacks to the Eulerian fields. We show that the surface precipitation rate and the slope of the RSD are especially sensitive to the treatment of selfcollection in the LD model. Some uncertainty remains in determining the velocity difference of a pair of LDs, which appears as a factor in the collection kernel. On the one hand, a pure gravitational kernel underestimates the collection rate because it neglects the horizontal component of the velocity difference of a pair of LDs. On the other hand, a Lagrangian subgrid-scale model that does not take velocity correlations among particle pairs into account overestimates the collision rate. In contrast gravitational sorting within an LES grid box and other parameters such as the initial mass distribution or the initial multiplicity are found to have no distinct effect on the development of the RSD.

Comparing the LD model to the bulk microphysics scheme, we find that the tail of the RSD is less sensitive to changes in the cloud droplet number density for the bulk scheme than for the LD model. The uncertainties due to assumptions in the LD model – including those in the treatment of selfcollection – are much smaller than uncertainties of the bulk rain microphysics scheme due to assumptions on the shape parameter and the cloud droplet number density. We therefore conclude that the LD model is a valuable tool for further studies to advance understanding of raindrop growth and dynamics.

CHAPTER 4

ON THE DEVELOPMENT OF THE SHAPE OF THE RAINDROP SIZE DISTRIBUTION IN SHALLOW CUMULUS

Rain drops keep fallin' on my head.

(B.J. Thomas)

In this chapter, the growth of raindrops and the development of the raindrop size distribution (RSD) are investigated for two isolated shallow cumulus clouds. Bulk rain microphysics schemes typically assume that the RSD is well represented by a 3-parameter gamma distribution. Hence, for two-moment bulk rain microphysics schemes an additional closure relation has to be established to determine the shape parameter of the RSD. We show that the evolution of the rainwater content, in particular the subcloud layer rainwater amount and the surface precipitation rate, are highly sensitive to the choice of the shape parameter.

To further investigate the shape of the RSD, the Lagrangian drop (LD) model is used to represent warm rain microphysics without a priori assumptions on the RSD. We show that the shape parameter is highly variable in space and time and that existing closure equations, which are established from idealised studies of more heavily precipitating cases, are not appropriate for shallow cumulus. Although a relation of the shape parameter to the mean raindrop diameter is also found for individual shallow cumulus clouds, this

relation differs already for the two clouds considered. We therefore cast doubt on whether a diagnostic parametrisation of the shape parameter, i.e., a local closure in space and time, can be sufficient, especially when being applied across different cloud regimes.

4.1. Introduction

In bulk microphysics schemes, the particle size distribution of each hydrometeor category is approximated by a continuous function with several free parameters. The RSD, $n(D)$, is often assumed to follow the form of a gamma distribution in terms of the raindrop diameter, D ,

$$n(D) = N_0 D^\mu e^{-\lambda D} \quad (4.1)$$

which has three free parameters: N_0 is referred to as the intercept, μ the shape and λ the slope parameter (Ulbrich, 1983, see also Fig. 1.4).

In three-moment bulk rain microphysics schemes, all three parameters of the gamma distribution are determined from the prognostic moments (Milbrandt and Yau, 2005; Milbrandt and McTaggart-Cowan, 2010). Although those schemes are potentially more accurate than single- or two-moment schemes, they still lack accurate parametrisations of, e.g., breakup and evaporation and how these processes modify the higher moments of the RSD. Also, three-moment schemes are computationally considerably more expensive and therefore seldom used in large scale models.

Single- and two-moment schemes are widespread in atmospheric modelling (e.g., Kessler, 1969; Beheng, 1994; Walko et al., 1995; Feingold et al., 1998; Khairoutdinov and Kogan, 2000; Seifert and Beheng, 2001; Morrison et al., 2005). In two-moment schemes, usually N_0 and λ are determined from the prognostic moments while μ , which is related to the width of the distribution, is fixed to a constant or diagnosed as a function of the mean raindrop diameter (Milbrandt and Yau, 2005; Seifert, 2008). In this chapter, we analyse the sensitivity of a two-moment bulk rain microphysics scheme to the choice of μ and investigate the evolution of μ in the course of a cloud's (rainwater) lifecycle using the LD model described in Chapter 3.

Especially in single-moment schemes (e.g. Kessler, 1969), μ is often set to zero, which simplifies the gamma distribution to an inverse-exponential distribution and has been suggested from measurements for raindrop diameters larger than 1.5 mm (Marshall and Palmer, 1948). Because Marshall and Palmer (1948) were only able to measure such large diameters and also had to average over relatively long periods of time, this classical result should not be viewed as evidence for using $\mu = 0$ for all raindrop sizes and instantaneous distributions.

The decisive role of μ in determining microphysical process rates has been discussed

in several idealised modelling studies. By considering sedimentation only (Milbrandt and Yau, 2005; Wacker and Lüpkes, 2009; Milbrandt and McTaggart-Cowan, 2010) as well as taking into account all microphysical processes in a one-dimensional bin microphysics rainshaft model (Seifert, 2008), different relations for μ as a function of the grid box mean volume diameter, \bar{D} , have been suggested. But those studies also show that the μ - \bar{D} relation is variable, which might suggest that an additional dependence or even a non-local closure in time that takes into account the lifecycle of the cloud is necessary to considerably reduce the present uncertainty in determining μ .

Reducing the number of independent parameters for the gamma distribution from three to two is not only of interest for parametrising rain microphysics, but is also necessary in the field of radar meteorology. For the latter, typically two independent remote measurements are obtained, e.g., reflectivity and attenuation for a dual-wavelength radar or reflectivity at horizontal and vertical polarization for a polarimetric radar. To retrieve the RSD, which is again assumed to be well represented by the gamma distribution, a constraining relation is required. Analysing disdrometer measurements, relations expressing μ as a function of λ have been proposed (e.g. by Zhang et al., 2001; 2003; Moisseev and Chandrasekar, 2007; Munchak and Tokay, 2008). Unfortunately, the applicability of those relations for parametrising microphysical processes is limited for two reasons: First, the relation is found to be regionally and seasonally variable (Munchak and Tokay, 2008) and it is not clear what is causing this variation. Second, all measurements are taken at the surface and are therefore not necessarily valid for the whole atmospheric column.

Concerning the second point, Geoffroy et al. (2014) analysed in-situ aircraft observations from a particle measurement system in shallow cumulus. They find that μ is variable over orders of magnitude when related to the height or to different rain properties, such as the mean raindrop diameter. This broad range might be better understood if such data were available for single rain events that are related to particular clouds and their lifecycle rather than for a whole field of clouds. The high spatial and temporal resolution that would be required for such an in-depth analysis is difficult, if not impossible, to obtain from field measurements. Therefore, we will use high resolution modelling to approach the issue in our study.

The goal of this chapter is to investigate the variability of the RSD and the closure problem of a two-moment bulk scheme in a less idealised setup than modelling studies have applied yet (e.g., Milbrandt and Yau, 2005; Seifert, 2008). For our analysis, we use the control run of cloud A and the control run of cloud B from Chapter 3: two isolated, lightly precipitating shallow cumulus clouds simulated with the bulk rain microphysics scheme from Seifert and Beheng (2001) and with the LD model.

The rest of the chapter is structured as follows: In Sect. 4.2, we investigate the lifecycle of the two clouds regarding their rainwater properties and microphysical processes for both the bulk scheme and the LD model. In the following main part Sect. 4.3, we analyse the

RSD and in particular the role of the shape parameter. Finally, in Sect. 4.4 we give some concluding remarks.

4.2. Cloud lifecycle

Snapshots of the rainwater mixing ratio and the precipitation flux show very similar spatial structures for the LD model and the bulk rain microphysics scheme (Fig. 4.1). Good agreement is also found for the temporal development of the profiles of the rainwater mixing ratio and the raindrop number density (Fig. 4.2 a-d and Fig. 4.3 a-d). It seems therefore justified to consider feedbacks to the dynamics only from the bulk scheme and run the LD model without any effect on the thermodynamic fields (see Sect. 3.3). Despite this relatively good overall agreement, some differences between the LD model and the bulk scheme are found, e.g., in the maximum absolute values of the rainwater mixing ratio and the precipitation flux (Fig. 4.1). To better understand those differences, we first analyse the (rainwater) lifecycle of cloud A and cloud B, and then investigate the differences between the rainwater properties from the LD model and the bulk scheme in more detail. The two clouds considered in this study can be seen as random samples from a typical trade wind cumulus clouds ensemble (see Sect. 3.2.2).

The temporal development of cloud A and cloud B with respect to their rainwater amount and the microphysical rates is quite different (Fig. 4.4). While for cloud A the peak overall rainwater amount is twice as high as for cloud B, the period of time that considerable rainwater amount is present in the domain is shorter for cloud A than for cloud B by about 10 min. This is a result of the different dynamics and consequently different microphysical rates in both simulations.

For cloud A we find one main updraft at around 20 min where the cloud water mixing ratio is high near cloud top and where therefore a high autoconversion rate transforms cloud water to rainwater in the bulk scheme (Fig. 4.5 a). Soon after this relatively short initial kick-off from the autoconversion, accretion increases and starts to dominate rainwater gain (Fig. 4.4 a). Because rainwater gain through accretion occurs inside the cloud and rainwater is lost through evaporation outside the cloud, we describe the lifecycle of the cloud in terms of its in-cloud rainwater, its cloud-layer environmental rainwater (i.e., rainwater in the cloud layer but outside the cloud, which is defined by the presence of bulk cloud water) and its subcloud layer rainwater. While most of the rainwater is found inside the cloud in the initial stage, this changes in short order. The rainwater found in the cloud layer environment increases and reduces the in-cloud rainwater. At this point evaporation of rainwater starts to decrease the overall rainwater amount drastically (Fig. 4.4 b).

It is interesting to note that only a very small fraction of the overall rainwater amount in the domain is found in the subcloud layer (Fig. 4.4 a). This implies that almost all rainwater leaves the cloud through its lateral boundaries rather than through cloud base

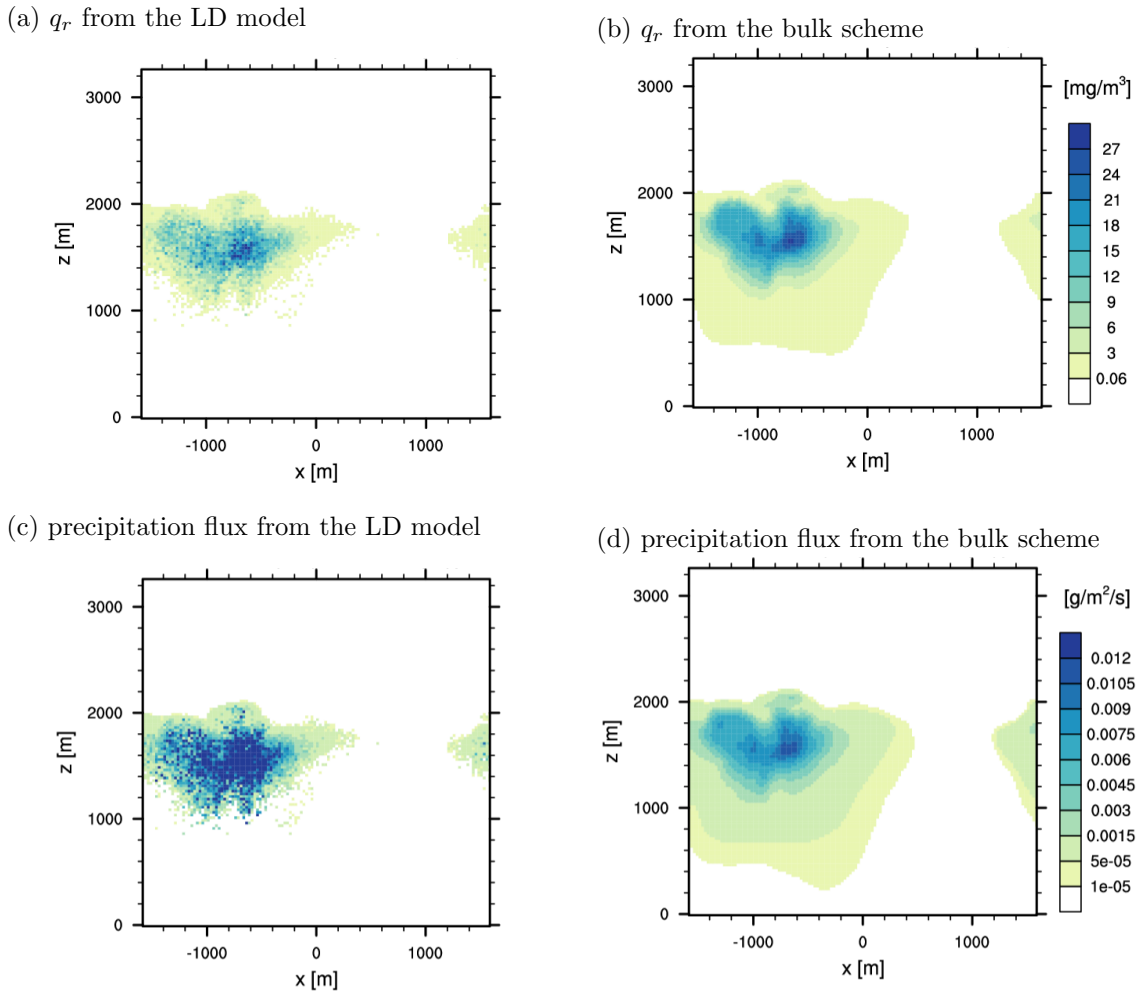
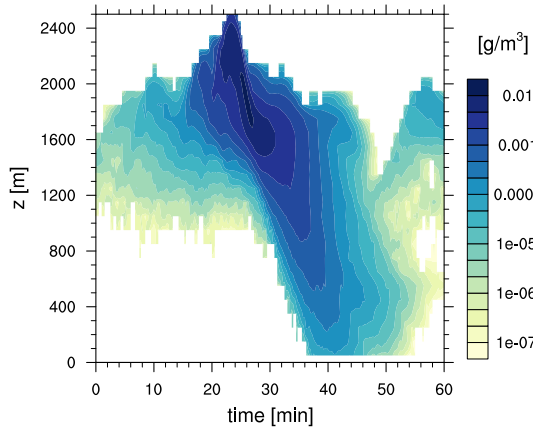


Figure 4.1.: Snapshot at $t = 30$ min averaged in y -direction for the rainwater mixing ratio and the precipitation flux for cloud A.

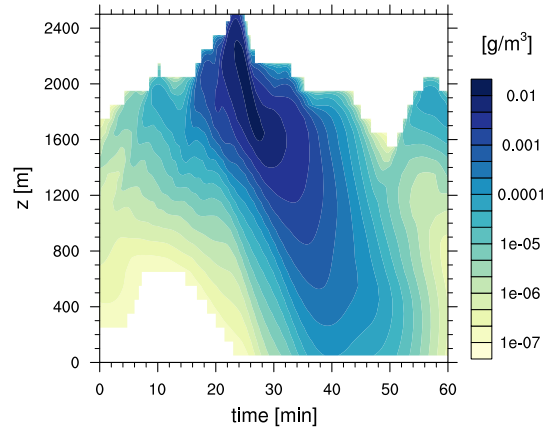
(see also Sect. 5.4.2). The maximum subcloud layer rainwater is found approximately 15 min after the maximum in total rainwater. This delay might be explained by two processes, which are closely related. First, embryo raindrops need time to grow through accretion and selfcollection to become so large that they develop a considerable fall velocity to be able to fall below cloud base. Second, the autoconversion rate is maximum near cloud top between 2000 m and 2500 m and it takes the raindrops some time to cover the distance, whether through cloudy or environmental air, until cloud base level (around 600 m).

While the simple lifecycle of cloud A rather closely depicts our understanding of an idealised precipitating shallow cumulus cloud, the picture is more complex for cloud B. Here, several smaller cloud water maxima in the time evolution of cloud water are found (Fig. 4.5 b). Accordingly, several autoconversion and subsequent accretion and evaporation events take place and have cumulative effects (Fig. 4.4 b, d). For example, the autoconversion rate has five maxima or pulses during the lifetime of cloud B. Such a pulsating growth

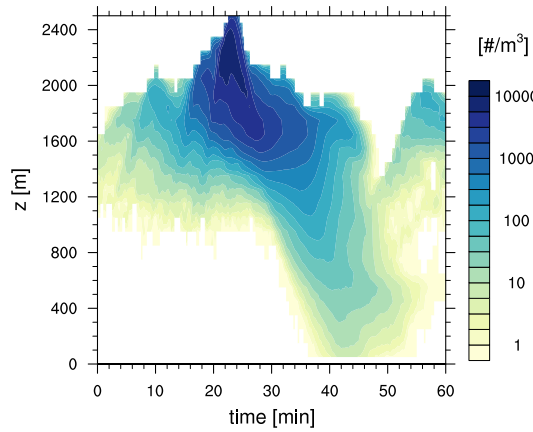
(a) q_r from the LD model



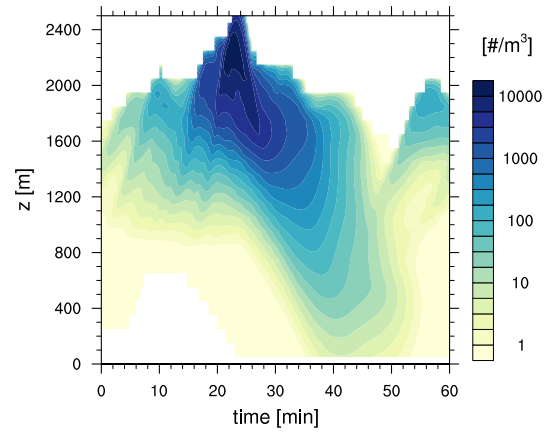
(b) q_r from the bulk scheme



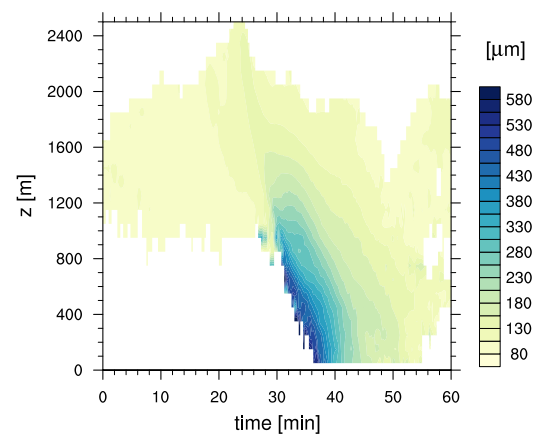
(c) n_r from the LD model



(d) n_r from the bulk scheme



(e) \bar{D} from the LD model



(f) \bar{D} from the bulk scheme

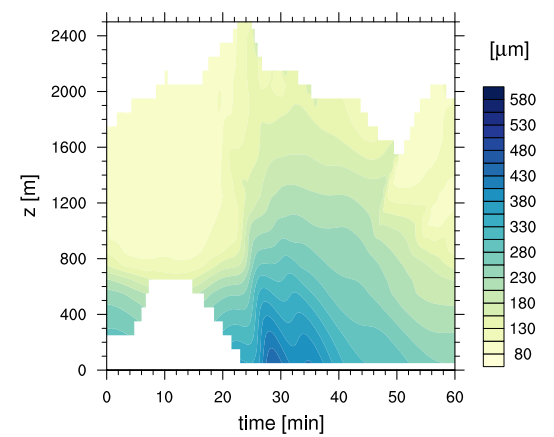
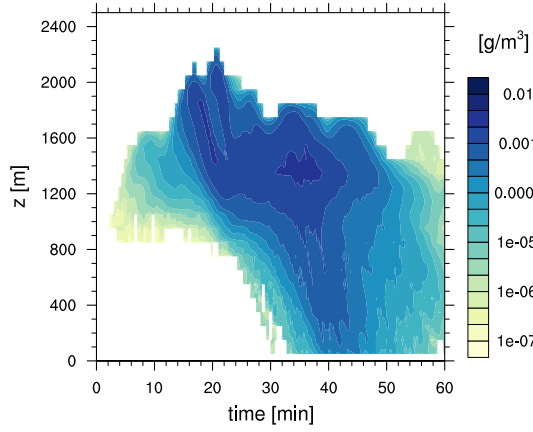
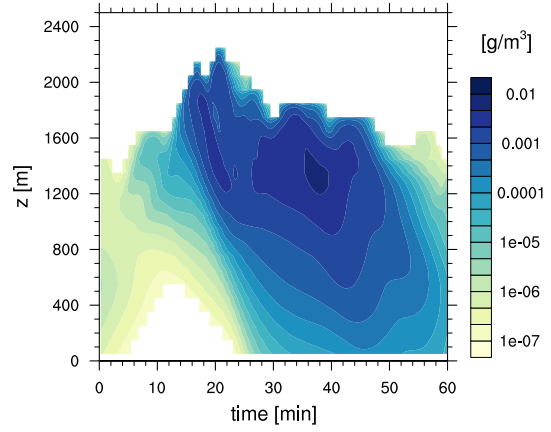


Figure 4.2.: Temporal development of the profiles of domain averaged properties for cloud A. Note the logarithmic scale for (a-d). For the bulk scheme areas with $q_r < 10^{-7}$ g/m³ are blanked out in (b, d, f).

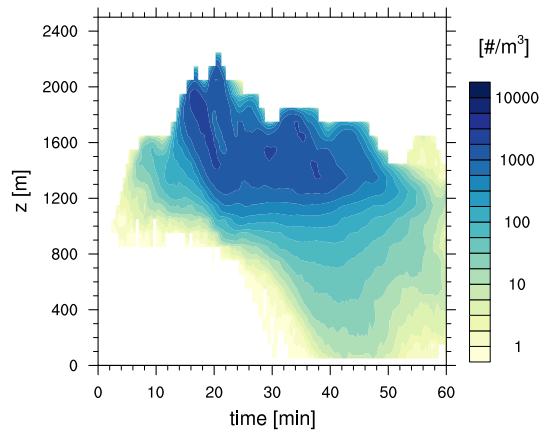
(a) q_r from the LD model



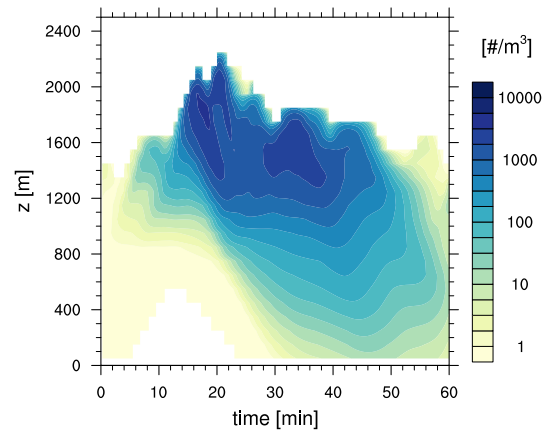
(b) q_r from the bulk scheme



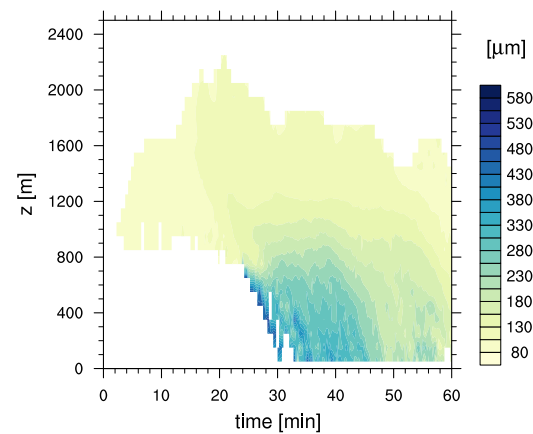
(c) n_r from the LD model



(d) n_r from the bulk scheme



(e) \bar{D} from the LD model



(f) \bar{D} from the bulk scheme

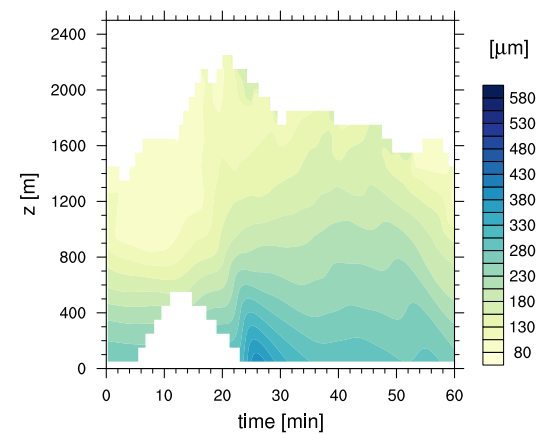


Figure 4.3.: As Fig. 4.2 but for cloud B.

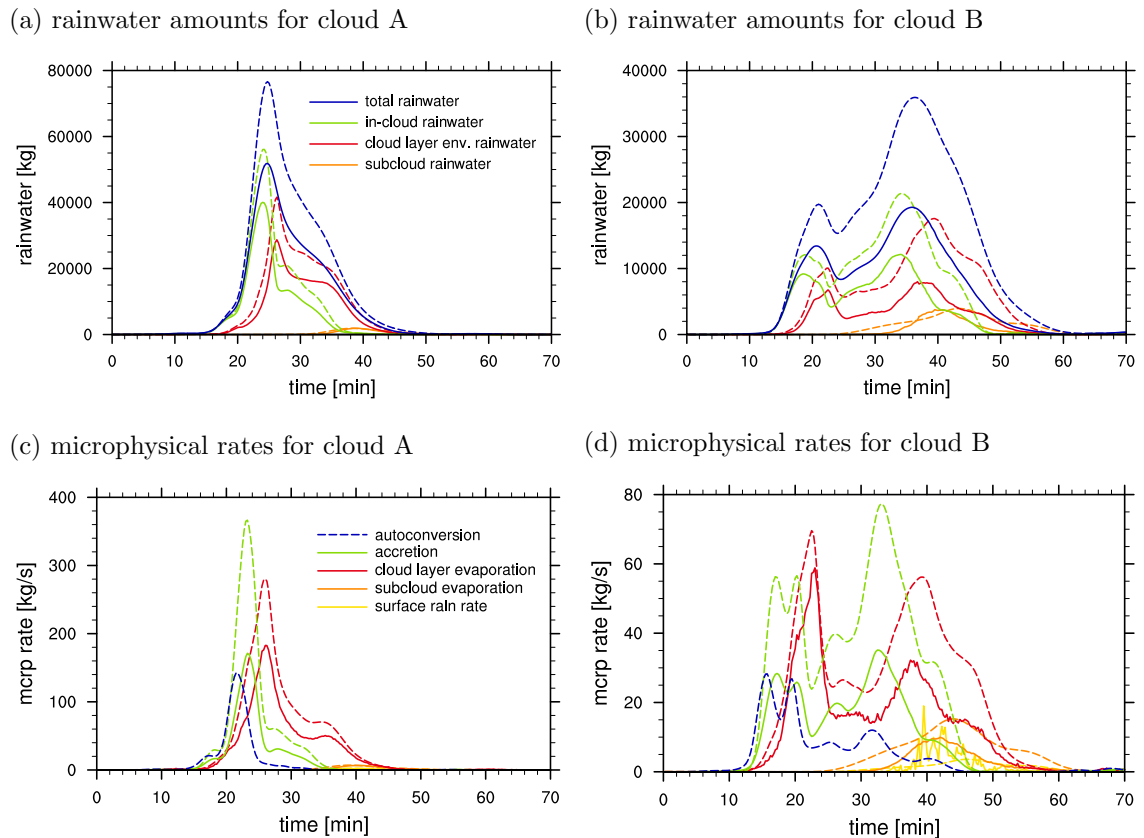


Figure 4.4.: Lifecycle of an isolated shallow cumulus cloud in terms of its rainwater properties. Shown are rainwater amounts and microphysical rates in the whole domain. Solid lines represent results from the LD model and dashed lines from the bulk scheme. Note the different scales on the y-axis.

is a common feature for shallow cumulus clouds (Rauber et al., 2007; Heus et al., 2009). Analysing LES runs of different shallow cumulus cases, Heus et al. (2009) find on average four pulses per cloud. This indicates that cloud B might be more representative for a typical shallow cumulus cloud than cloud A.

Compared to cloud A the occurrence of rainwater in the domain is considerably prolonged for cloud B and rainwater builds up so that the maximum rainwater amount is reached only after 25 min (Fig. 4.4). The total rainwater amount is smaller for cloud B than for cloud A due to weaker updrafts and overall smaller microphysical rates. In contrast to cloud A, the raindrops in cloud B have more time to grow and the amount of rainwater in the subcloud layer relative to the total rainwater amount and also the surface precipitation rate are higher.

Some systematic differences can be found between the rainwater properties from the bulk scheme and from the LD model. While the profiles of the rainwater mixing ratio and the raindrop number density show similar patterns for the bulk scheme and the LD model, differences can be found in the details (Fig. 4.2 and Fig. 4.3). This becomes especially

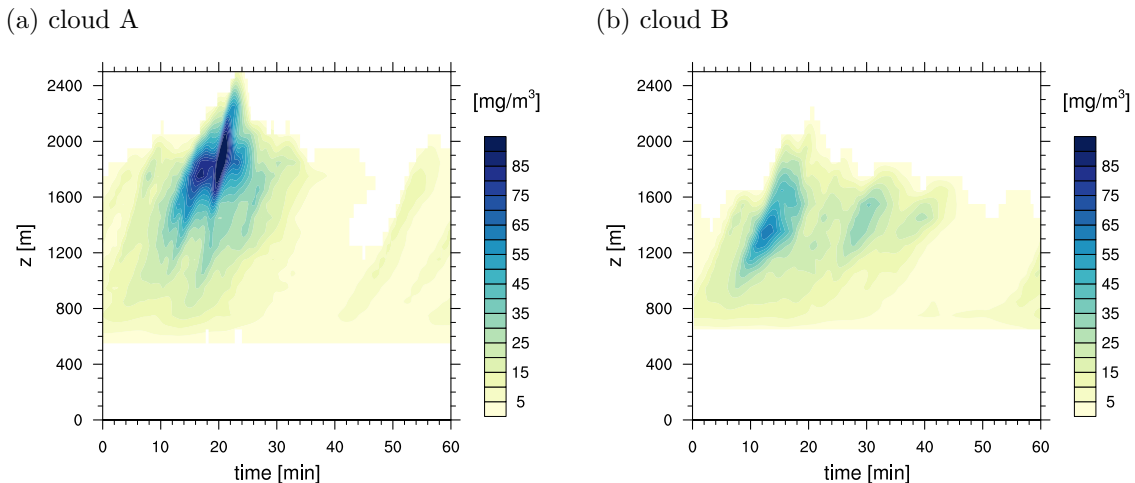


Figure 4.5.: Temporal development of the profiles of the domain averaged cloud water mixing ratio.

apparent for the mean raindrop volume diameter, \bar{D} :

$$\bar{D} = \left(\frac{6}{\pi \rho_w} \frac{q_r}{n_r} \right)^{\frac{1}{3}} \quad (4.2)$$

where q_r is the rainwater mixing ratio, n_r is the raindrop number density and ρ_w is the density of water. In the subcloud layer the rainwater mixing ratio increases earlier in the bulk scheme than in the LD model, while the raindrop number density is still low for both. Therefore, \bar{D} also increases earlier for the bulk scheme than for the LD model. This too early onset of surface precipitation due to too strong gravitational sorting is a known issue of two-moment bulk rain microphysics schemes and will be discussed further in Sect. 4.3.1. Despite the difference in the onset of surface precipitation, also the maximum raindrop diameter is found to be larger for the LD model than for the bulk scheme. In the subsequent period, when the rainwater mixing ratio decreases in the subcloud layer, this decrease is more rapid for the LD model than for the bulk scheme. Accordingly, also \bar{D} decreases faster for the LD model than for the bulk scheme.

Differences between the LD model and the bulk scheme are also found for the microphysical rates (Fig. 4.4 c, d). While by design of our model the autoconversion rate generates bulk rainwater and LD rainwater in same amounts, the accretion rate is smaller for the LDs than for the bulk scheme for both clouds over their whole lifecycle. As a result, the total rainwater and the evaporation rate are larger for the bulk scheme, too.

The cause for these differences can be found in the RSDs (Fig. 4.6). For both clouds when the first rainwater forms, the RSD determined from the LDs is slightly narrower than the one diagnosed and employed in the bulk scheme (Fig. 4.6 a, b). Therefore, the initial production of rainwater mass through accretion is less effective for the LDs and thus

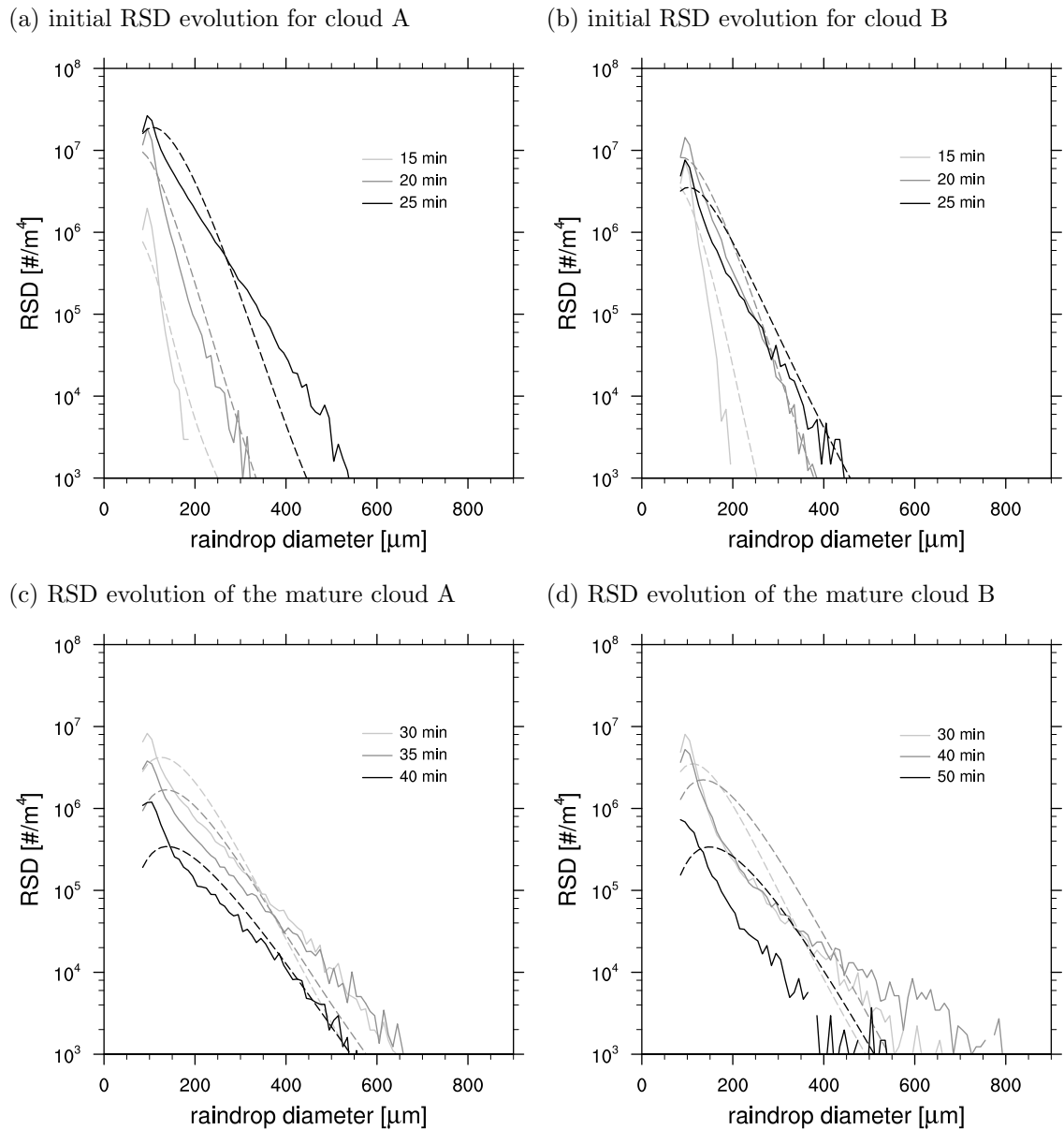


Figure 4.6.: Time evolution of the mean RSD for the whole domain. Solid lines represent results from the LD model and dashed lines from the bulk scheme.

influences the subsequent rainwater evolution. Nevertheless, RSD broadening is stronger for the LDs and the largest raindrops with a diameter larger than $500 \mu\text{m}$ form more frequently than in the bulk scheme (Fig. 4.6 c, d).

Therefore, though the total rainwater amount of the bulk scheme is higher, the subcloud layer rainwater amount and also the surface precipitation rate, which are both sensitive to the largest raindrops, are higher for the LDs (Fig. 4.4). This effect can also be seen in the snapshots of the horizontally averaged, vertical cross sections (Fig. 4.1). Though the maximum absolute value of the rainwater mixing ratio is larger for the bulk scheme, the

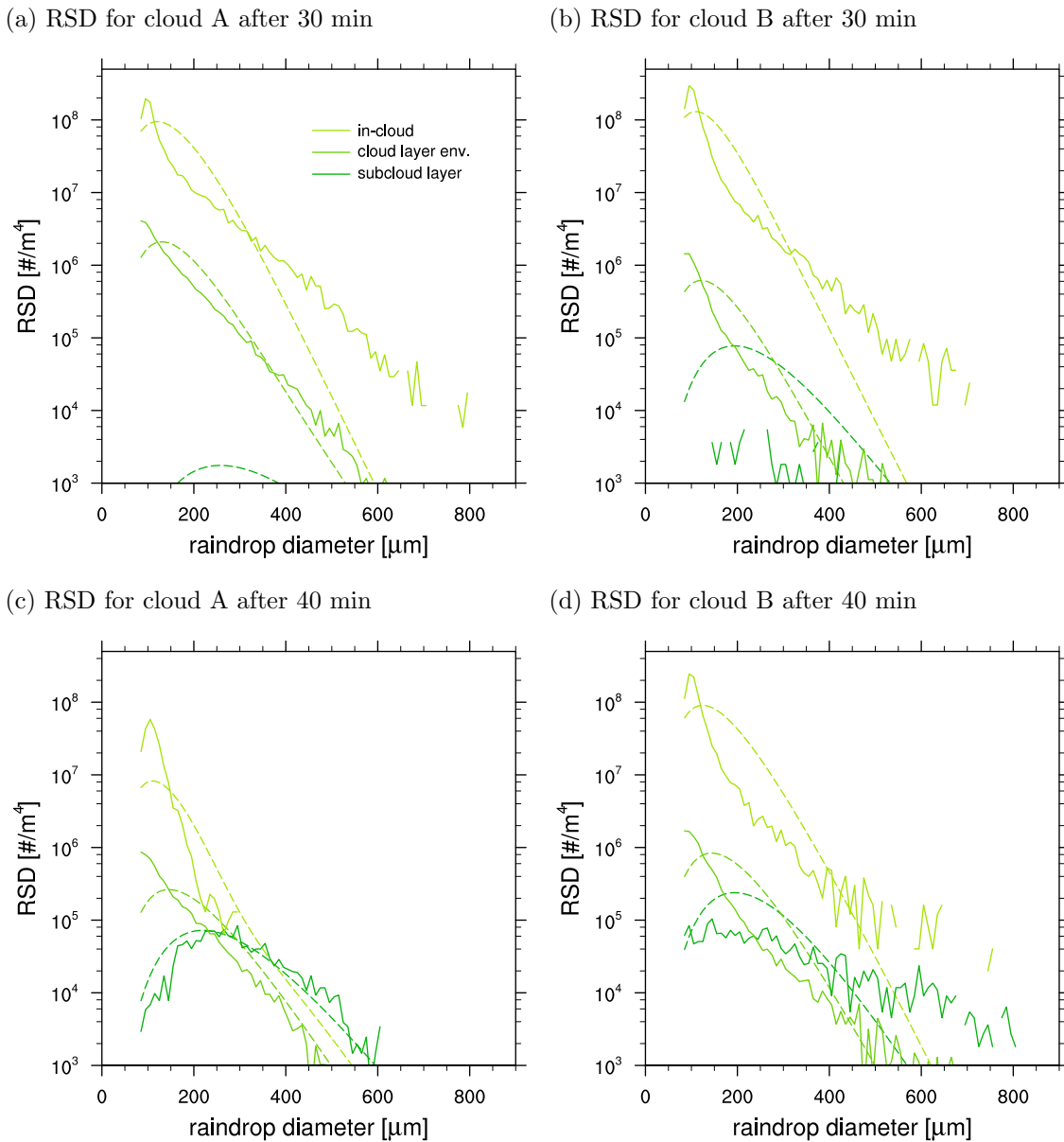


Figure 4.7.: RSD within the cloud, in the environmental cloud layer and in the subcloud layer. Solid lines represent results from the LD model and dashed lines from the bulk scheme.

precipitation flux is larger for the LD model, because it is dominated by the largest drops, which fall fastest.

The difference in the tails of the RSD of the LDs and in the bulk scheme for the whole domain (Fig. 4.6) can be mostly attributed to the in-cloud RSD (Fig. 4.7). For all diameter sizes, the in-cloud RSD shows a decrease in the number density of raindrops with increasing diameter. For the subcloud layer of cloud A, gravitational sorting is strong and the number density of raindrops increases for increasing raindrop diameters $< 250 \mu\text{m}$. There, the RSD of the LDs is in surprisingly good agreement with the RSD in the bulk

scheme. For the subcloud layer of cloud B, the RSD of the LDs is broader than the RSD in the bulk scheme.

4.3. The RSD's shape parameter

As discussed in the introduction (Sect. 4.1), bulk rain microphysics schemes are known to be sensitive to the choice of the shape parameter, μ , if a gamma distribution is assumed for the RSD (see Eq. 4.1). To investigate the role of μ , we approach the topic from two sides. First, we discuss the effect of μ on the rain properties in the bulk rain microphysics scheme. Second, we use the LD statistics to discuss how μ develops over the course of the simulation and what that implies for the parametrisability of μ .

4.3.1. Sensitivity of the bulk scheme to the RSD's shape parameter

While the simulations discussed in Sect. 4.2 use the diagnostic relation of Seifert (2008), another diagnostic relation has been suggested by Milbrandt and Yau (2005). Besides those two variants, we analyse two additional simulations, which have already been introduced in Chapter 3: for the first simulation μ is fixed to 1, for the second simulation μ is fixed to 10. Considering the uncertain knowledge of the value of the shape parameter, also a constant value of 1 or 10 is a plausible choice (Stevens and Seifert, 2008). Because in our simulations \bar{D} is always smaller than $700 \mu\text{m}$ the diagnostic relation from Seifert (2008) corresponds to a constant value of $\mu = 7$.

The smaller the value of μ the broader the RSD becomes, which ultimately leads to a higher surface precipitation rate. If compared to the RSD from the LD model, bulk rain microphysics schemes with large μ , i.e., narrow distributions, perform best during the very first stage of rain formation in the cloud, while bulk rain microphysics schemes with smaller μ seem more reasonable in a later stage (Fig. 4.6 and Fig. 4.8). If μ is chosen too small the amplitude of the surface precipitation rate is considerably overestimated by the bulk scheme compared to the LD approach (Fig. 4.9). Surprisingly, the differences in RSD (Fig. 4.8) and surface precipitation rate (Fig. 4.9) are larger for the simpler cloud A than for the more complex cloud B. We speculate that this is related to a more explosive development of cloud A, which might be less well represented by the bulk schemes.

Please note that the relative differences in surface rain discussed above may appear very large in part because the overall surface precipitation is small for shallow cumulus and because we are looking at an individual cloud instead of averaging over a larger area with a cloud ensemble. Related to this, an intercomparison study, analysing the RICO case with several different LES models using different microphysical parametrisations, showed that while many features of the cloud layer were in good agreement among the models, considerable differences were encountered in the cloud microphysical structure and the surface precipitation rate (van Zanten et al., 2011). This indicates that the RICO case

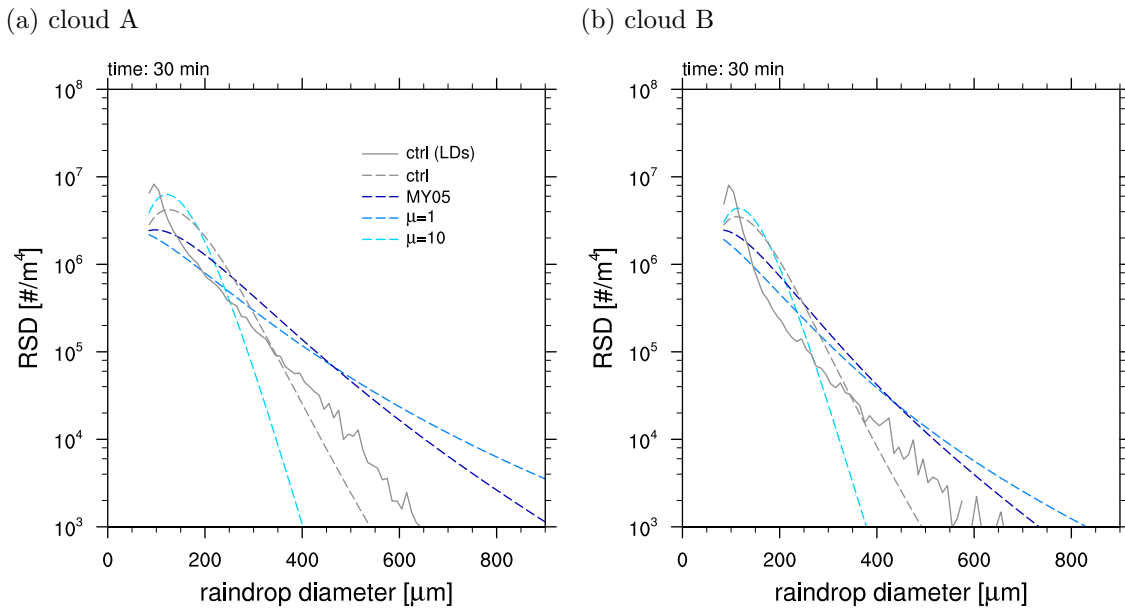


Figure 4.8.: RSD for the whole domain using different values for the shape parameter, μ , in the bulk scheme. Solid lines represent results from the LD model and dashed lines from the bulk scheme. MY05: Closure equation from Milbrandt and Yau (2005).

might be rather sensitive to microphysical choices especially when using small domain sizes as it is usually done. Thus, we expect differences, e.g., in surface precipitation, not to be as pronounced for other, heavier precipitating cases or when using larger domains and averaging over longer time periods.

Regardless of the choice of μ , we find an earlier onset of surface precipitation for the bulk rain microphysics schemes than for the LD model. This is in agreement with other studies, that attribute the too early onset of surface precipitation for two-moment bulk rain microphysics schemes to an overestimation of gravitational sorting in the sedimentation process, which is due to the differences in sedimentation speed for the two moments considered (Wacker and Seifert, 2001; Morrison and Grabowski, 2007; Seifert and Stevens, 2010). This bias is inherent in the two-moment equations and cannot be eliminated by a simple retuning of some parameters, like the shape parameter. As shown by Wacker and Seifert (2001) bulk schemes eliminate the most important variable for size sorting (the size) and by this a non-linear equation emerges from the previously linear sedimentation equation. In one- and two-moment bulk schemes, the RSD does not become narrower when the largest raindrops fall out because the shape is prescribed either as a fixed value or by some diagnostic relation. This leads to an artificial spectral transfer, i.e., the large drops that fall out are immediately created again.

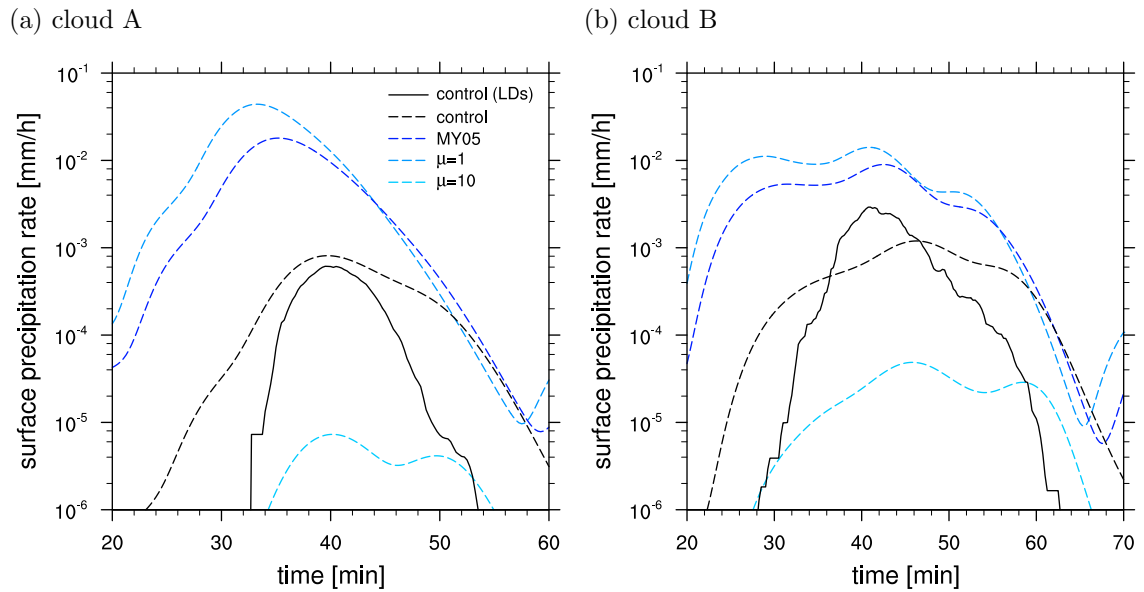


Figure 4.9.: Domain average surface precipitation rate using different values for the shape parameter, μ , in the bulk scheme. Solid lines represent results from the LD model and dashed lines from the bulk scheme. MY05: Closure equation from Milbrandt and Yau (2005). Shown are 2-min running averages of the surface precipitation rate.

4.3.2. Evolution of the RSD's shape parameter in the LD model

For the LDs, the RSD is not bound to a gamma distribution but can evolve freely. Assuming that the LD RSD is well represented by a gamma distribution (Eq. 4.1), the distribution's parameters can be estimated from the first three moments of the RSD. To have a sufficient sample for the RSD, we estimate the distribution's parameter only if there are more than 50 LDs within a vertical layer of 100 m for one output time step. We find that μ is widely varying with time and height, but some more general behaviour can be deduced from the two simulations of lightly precipitating shallow cumulus (Fig. 4.10):

1. Large values for μ , i.e., narrow RSDs, are found near cloud top where raindrops are created by autoconversion at similar sizes and where the mean volume diameter is close to the initial raindrops diameter (Fig. 4.2 e and Fig. 4.3 e). However, note that for the LDs the initial size is set artificially by assuming an initial size distribution as described in Sect. 3.3.1 and that the RSD is truncated below $D = 80 \mu\text{m}$, which both constrains the reliability of the estimate of μ (see Handwerker and Straub, 2011; Johnson et al., 2011, for a discussion of the latter issue). One should therefore be cautious with a physical interpretation of the large values of μ at the initial appearance of rainwater in the cloud layer.
2. In the cloud layer, μ is decreasing with decreasing height and progressing cloud lifetime. The RSD is broadening with time because different trajectories allow for

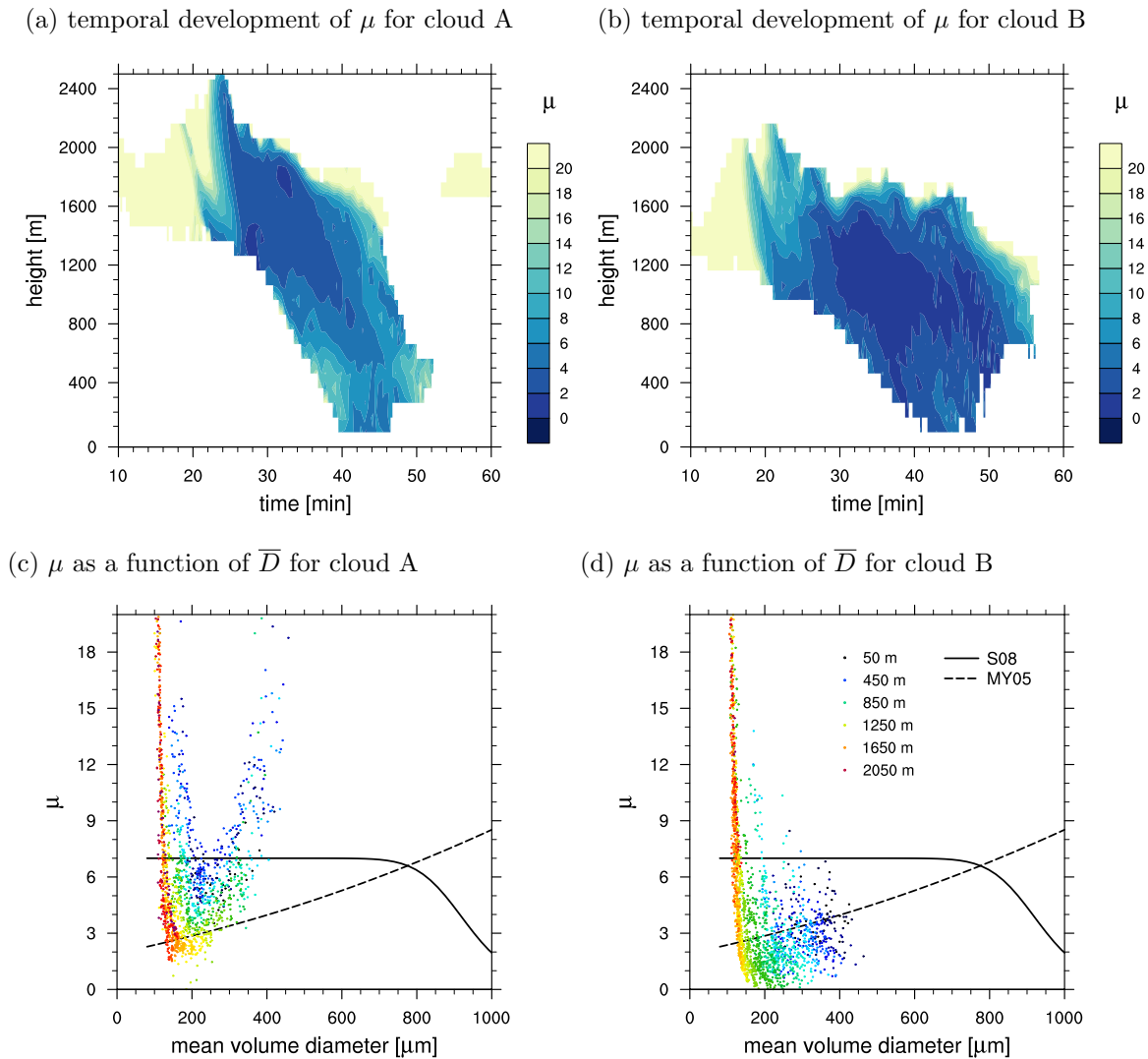


Figure 4.10.: Evolution of the shape parameter: μ as a function of height and time and μ as a function of the mean raindrop diameter colored by height. In (c,d) additionally the closure equations from Seifert (2008, S08) and Milbrandt and Yau (2005, MY05) are plotted.

different growth histories of the raindrops. As most of the LDs originate near cloud top, RSDs in lower cloud layers are typically older and therefore broader.

- For cloud A, three stages can be identified in the subcloud layer that have also been described in more idealised studies (e.g., by Seifert, 2005). First, large values for μ are found when the first raindrops reach the subcloud layer. Due to gravitational sorting the largest raindrops reach the subcloud layer first, which gives a narrow distribution with a large mean diameter. With time μ decreases in the subcloud layer because smaller raindrops eventually follow the first large ones. In this second stage, the RSD becomes broader while the mean raindrop diameter decreases. Finally, μ increases again while the mean diameter still decreases. At this stage the largest

raindrops have already reached the ground while some smaller ones remain in the subcloud layer.

4. For cloud B, which – unlike cloud A – is characterised by several pulses of autoconversion events (see Sect. 4.2), the second and third stage can be identified in a similar manner whereas the first stage of extensive gravitational sorting is not found. This might be explained by the more diverse development of cloud B. Raindrops need to be supported for a relatively long time in the upper part of the cloud layer to grow to the largest sizes. Then moderately large raindrops fall out first (when they are not supported by an updraft anymore) while the largest drops (that “luckily“ had been supported longer and were therefore able to grow most) fall out later but are able to outpace the moderately large raindrops. Therefore, the early RSDs in the subcloud layer are already relatively broad.

Overall, the (truncated) V-shape of the μ - \overline{D} relation seems to be a rather robust feature, which is found in both of our simulations for shallow cumulus clouds (Fig. 4.10). In contrast, the position of the anchor point of the V-shaped μ - \overline{D} relation seems to be rather case dependent, which makes a general parametrisation difficult. It is interesting to note that for the more complex cloud B the right-hand side branch, which is attributed to extensive gravitational sorting, is missing.

4.4. Conclusions

In this chapter, we investigate the lifecycle of shallow cumulus clouds regarding their rainwater properties with a focus on the development of the shape of the RSD. Two isolated shallow cumulus clouds are simulated with LES. The properties of the rainwater field of each cloud are studied, both with a commonly used warm rain bulk microphysics scheme and with an LD model.

While the development of the rainwater for cloud A is characterised by a single autoconversion event and subsequently developing accretion and evaporation rates, the development of cloud B is more complex. Here, several overlapping autoconversion events result in a less distinct temporal separation of the autoconversion, accretion and evaporation phase. For both clouds, the RSD in the LD model is initially narrower than what is assumed in the bulk scheme, but broadens more in the course of time. Therefore, though the overall rainwater mass is less for the LD model than for the bulk scheme, the subcloud layer rainwater mass and the surface precipitation rate are in a similar range.

However, this is only true if the shape parameter, μ , of the RSD in the bulk scheme is diagnosed by the relation suggested by Seifert (2008), which we use for our control runs. Fixing μ to a lower constant value or using the diagnostic relation suggested by Milbrandt and Yau (2005) broadens the RSD and consequently has a quite drastic effect,

e.g., on the surface precipitation rate. Though this rather large effect may be partly due to the relatively low overall precipitation rate in shallow cumulus, it obviously points to the important role of μ in the bulk rain microphysics scheme.

Investigating the development of μ derived from the LD statistics, we find a V-shaped μ - \bar{D} relation for cloud A that can be attributed to different processes and stages of the rainwater development. For the more complex cloud B, the right-hand side ascending branch, that is related to extensive gravitational sorting, is not found. This indicates that for the simple, "single event" cloud A our results are in good agreement with idealised studies that described the V-shape before (e.g., Seifert, 2005), but that for more complex lifecycles the μ - \bar{D} relation has to be modified. A V-shaped relation though shifted substantially towards larger mean diameters has also been found by Seifert (2008) for stronger rain events. In more heavily precipitating clouds larger raindrops are more common due to deeper cloud layers, higher rainwater contents and more vigorous updrafts. Hence, gravitational sorting becomes dominant only at larger diameters and the μ - \bar{D} relation shifts towards those larger diameters. Milbrandt and Yau (2005) also focused on stronger precipitation events just taking into account sedimentation and consequently, only found an ascending branch towards large diameters. Because shallow cumulus precipitation is restricted to relatively small raindrops, both published μ - \bar{D} relations fail to represent our shallow cumulus case.

Our results suggests that parametrising μ solely as a function of \bar{D} is not appropriate if different cloud regimes and different complexities of cloud lifecycles are considered. Though the (truncated) V-shaped μ - \bar{D} relation seems to be a relatively robust feature, the position of the anchor point, the occurrence of the ascending branch and presumably also the slopes of the branches might depend on other variables such as overall precipitation, updraft speed or cloud depth. Rather than the mean raindrop diameter a classification according to the stage of the RSD's evolution could also be useful. Therefore, a non-local closure in time, i.e., a parametrisation that has explicit knowledge about the current state of the clouds relative to its overall lifecycle, might ultimately be needed if the error that arises from a μ - \bar{D} closure is judged to be too large.

CHAPTER 5

RECIRCULATION AND GROWTH OF RAINDROPS IN SHALLOW CUMULUS

Everything is the way it is
because it got that way.

(D'Arcy Wentworth Thompson)

In this chapter, the role of recirculation of raindrops for the formation of precipitation in shallow cumulus is investigated. Two related cases of fields of lightly precipitating shallow cumulus are simulated using Large-Eddy Simulations (LES) combined with the Lagrangian drop (LD) model for raindrop growth and a cloud tracking algorithm. Statistics from the LD model yield that most raindrops leave the cloud laterally and then evaporate in the subsaturated cloud environmental air, but that 1 % to 3 % of the raindrops contribute to surface precipitation. Among this subsample of raindrops that contribute to surface precipitation two growth regimes are identified: those raindrops that are dominated by accretional growth from cloud water, and those raindrops that are dominated by self-collection among raindrops. The mean cloud properties alone are not decisive for the growth of an individual raindrop but the in-cloud variability is crucial. Recirculation of raindrops is found to be common in shallow cumulus, especially for those raindrops that contribute to surface precipitation. The fraction of surface precipitation that is attributed to recircu-

lating raindrops is variable from cloud to cloud but can be larger than 50 %. This implies that too simplified concepts of raindrop growth that neglect the effect of recirculation disregard a substantial portion of raindrop growth in shallow cumulus.

5.1. Introduction

Although shallow cumulus are not producing vast amounts of precipitation, precipitation and especially the evaporation of precipitation are known to influence the boundary layer structure, e.g., by forming cold pools, which are important for the organisation of shallow cumulus (Jensen et al., 2000; Seifert and Heus, 2013). To represent those effects adequately, an appropriate representation of rain microphysical processes is essential. Bulk microphysics parametrisation, especially when applied to models with a coarse resolution, are known to encounter biases if they do not account for subgrid-scale variability (Pincus and Klein, 2000; Chosson et al., 2014). In addition to the subgrid-scale variability of the bulk fields, the microphysical process rates also depend on the raindrop size distribution (RSD) and therefore on the growth history of individual raindrops. Depending on the complexity of the raindrops' growth histories, the development of the RSD is difficult to parametrise from local variables (in space and time). In this chapter, we aim to investigate the growth history of raindrops after the initial cloud droplet phase, and the role of recirculation for the formation of precipitation.

In the last decades most microphysical process studies for warm rain formation have focused on the broadening of the cloud droplet size distribution and on the condensation-coalescence bottleneck of cloud droplet growth, the so-called size gap, which describes the (lack of) growth of cloud droplets in a size range of 10-30 μm in radius, where neither condensation nor collision-coalescence is thought to be very effective (Simpson, 1941; Langmuir, 1948). There is emerging agreement that small-scale turbulence does not enhance condensational growth of cloud droplets significantly but that the onset of precipitation is accelerated through small-scale turbulence by enhancing collision rates of cloud droplets (for reviews on this topic see, e.g., Vaillancourt and Yau, 2000; Shaw, 2003; Grabowski and Wang, 2013). Small-scale turbulence is also essential for large-eddy hopping, i.e., it allows cloud droplets to move from one large eddy to another. Due to large-eddy hopping cloud droplets originally located in the vicinity of a single point experience different condensational growth histories, which broadens the observed droplet size distribution (Cooper, 1989; Lasher-Trapp et al., 2005; Bewley and Lasher-Trapp, 2011; Devenish et al., 2012; Grabowski and Wang, 2013). A detailed discussion of the broad literature on the size gap, cloud droplet size distribution broadening and turbulence-enhanced collision rates is given in Sect. 1.5.

As opposed to cloud droplet growth, raindrop growth beyond the size gap has attracted far less attention, and the role of small-scale turbulence and large-eddy hopping for the

growth history of drizzle drops and raindrops is less clear. For stratocumulus the in-cloud residence time of raindrops is found to be decisive for whether raindrops reach the subcloud layer and subsequently also the surface (Stevens et al., 1996a; Feingold et al., 1996; Kogan, 2006). Using Lagrangian parcels, Pinsky et al. (2008) and Magaritz et al. (2009) find that a certain fraction of lucky parcels, which exceed a threshold in liquid water content, is needed to trigger drizzle and that mixing plays an important role in this process (Magaritz-Ronen et al., 2014). Using an idealised single cloud setup, Cooper et al. (2013) find that also for cumulus, raindrop embryos need favourable cloud water conditions to significantly contribute to precipitation. To trigger precipitation only a small fraction of raindrops has to be statistically fortunate enough to experience such beneficial conditions (Telford, 1955; Kostinski and Shaw, 2005).

In this chapter, we study the growth history of raindrops in a field of shallow cumulus clouds. In particular, we ask two questions: Which microphysical processes are important in the growth history of raindrops reaching the ground? And: What is the role of recirculation of raindrops for the formation of precipitation? To investigate these questions, we combine Eulerian LES of a field of shallow cumulus with the LD model for raindrop growth (Chapter 3). By additionally applying a cloud tracking algorithm on the LES fields, the LD's trajectories are also analysed in the context of the temporal development of the cloud entity they originate from.

The rest of this chapter is structured as follows: In Sect. 5.2, we shortly describe the model setup. In Sect. 5.3, we characterise the behaviour of raindrops in a field of shallow cumulus analysing cloud field statistics and LD statistics. Then in Sect. 5.4, we discuss the growth mechanisms of raindrops focusing first on accretion and selfcollection, and then on the role of recirculation. Finally in Sect. 5.5, we conclude our results.

5.2. Model setup

We use the UCLA-LES, the case description of the standard RICO and the moist RICO setup, and the control run configuration of the LD model as described in Sect. 3.2. But unlike in Chapter 3 and Chapter 4, here we use a larger domain of 12.8^2 km^2 to simulate a field of shallow cumulus clouds rather than a single cloud. Such a field of shallow cumulus clouds allows us to investigate possible interactions between individual clouds and gives more robust statistics in terms of the variability of individual clouds. For both the standard and the moist RICO simulation, the domain height is 3.2 km and the grid spacing is 25 m in all three spatial directions. After a spin-up time of 7 h for the Eulerian LES both simulations are run for 4 h including the LD model, which in total results in 3.9×10^6 LDs for the standard RICO simulation and 10.1×10^6 LDs for the moist RICO simulation.

To analyse the LDs' trajectories and their growth histories, LD properties are saved

every 15 s (as described in Sect. 3.3.5). After each selfcollection event, one of the two LDs that coalesce decreases in multiplicity but retains its mass (see Sect. 3.3.4). Obviously, this LD keeps its trajectory and its growth history also after the selfcollection event. The second LD retains its multiplicity but gains mass from the first LD, i.e., after the selfcollection event this growing LD consists of its original mass plus the mass of the first LD. Therefore it is not per se clear what the history of this growing LD is. In our LD model, we choose to keep the history of the growing LD in analogue to keeping the history of the first LD. Because usually the original mass of the growing LD is larger than the contribution from the first LD, this means that usually the history of an LD is chosen such that it represents the larger fraction of its mass. However the opposite case may occur, too.

In general, other ways to attribute an LD's history after a selfcollection event are possible. For instance, one may attribute the history of that LD that contributes the larger fraction of the new mass to the growing LD. This would imply that sometimes after the selfcollection event the original history of the growing LD is discarded and that both LDs then have the same history. Another possibility might be to calculate an average history of the two original LDs, possibly weighted by their contribution to the growing mass. However, it is not clear what kind of an average history would be meaningful.

To be able to attribute an LD to a particular cloud and to analyse the temporal development of individual clouds, the cloud tracking of Heus and Seifert (2013) is applied to the LES fields. The algorithm is tracking cloudy areas in (horizontal) space and in time using a cloud liquid water path threshold of 5 g/m^2 . A cloud splitting algorithm is necessary to distinguish cloudy objects that are connected in cloud liquid water path at a given time, but that have individual cores and largely keep their own properties. For the splitting, cores are defined as columns where the maximum in-cloud θ_v excess is larger than 0.5 K, and a region growing algorithm is used to allocate a cloudy area to a core. In this study, cloudy areas that are allocated to a cloud core are called *active clouds*. An active cloud can be both a single core cloud or a part of a multicore cloud system. Cloudy regions that are not allocated to a cloud core are called passive clouds or remnants as in Heus and Seifert (2013).

5.3. Characterisation of raindrops in a field of shallow cumulus

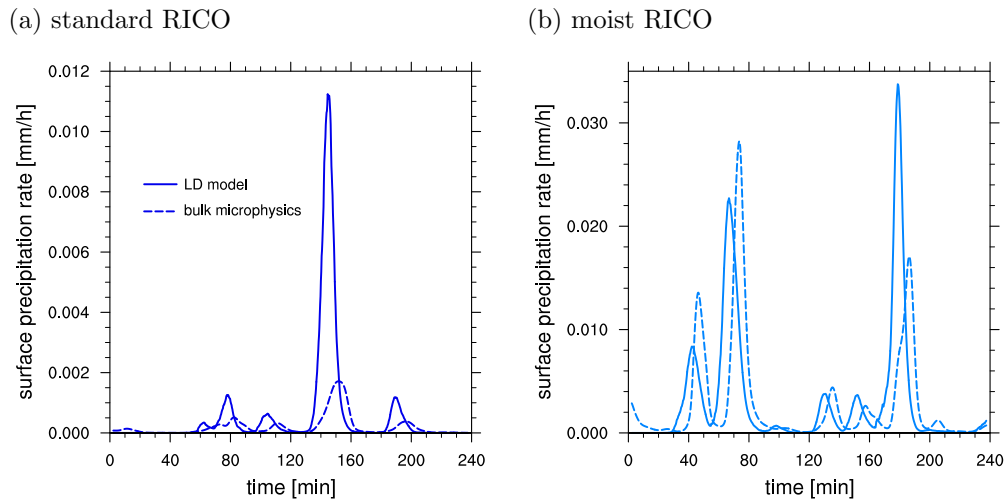
5.3.1. Cloud field statistics

In terms of cloud field properties, the moist RICO simulation is characterised by a higher cloud cover, a higher cloud liquid water path and a higher rainwater path than the standard RICO simulation (Table 5.1). Consequently, also the surface precipitation rate is higher for the moist RICO simulation than for the standard RICO simulation although the absolute

Table 5.1.: Characteristic properties of the cloud field for the standard RICO simulation and the moist RICO simulation.

	C [%]	LWP [g/m ²]	RWP [g/m ²]	R [mm/d]	h_{base} [m]	w_{max} [m/s]
standard RICO	15	11.3	0.8	0.0006	600	7.4
moist RICO	20	19.6	4.0	0.0032	600	7.5

C – cloud cover, LWP – cloud liquid water path, RWP – rainwater path, R surface precipitation rate, h_{base} – cloud base height, w_{max} – maximum vertical velocity. All values are averaged over the 4 h simulation time.

**Figure 5.1.:** Surface precipitation from the bulk rain microphysics scheme and the LD model.

values are low for both simulations (Fig. 5.1). The surface precipitation rate of the bulk rain microphysics scheme compares relatively well with the LD model. The earlier onset of surface precipitation for the LD model is attributed to a broader RSD for the LDs in the mature state of the cloud’s lifecycle, i.e., to more numerous large raindrops that have a high fall speeds and therefore reach the surface earlier (see Sect. 4.3.1).

For the standard RICO simulation, 520 active clouds are tracked in the course of the 4 h simulation excluding those clouds that already exist at the beginning of the simulation and those that still exist at the end of the simulation. Of those 520 clouds only 10 clouds produce surface precipitation. For the moist RICO simulation, there are overall fewer active clouds (308) of which more (23) produce surface precipitation. In particular, the small clouds are more numerous in the standard RICO simulation while there are slightly more of the largest clouds in the moist RICO simulation. For both simulations, only the largest clouds, which are also the ones that live longest and where most of the LDs originate from, produce surface precipitation (Fig. 5.2 a,b,c). The average lifetime of an active cloud is 16 min for the standard RICO simulation and 15 min for the moist RICO simulation. Those short living clouds do not have enough time for a significant broadening of the cloud

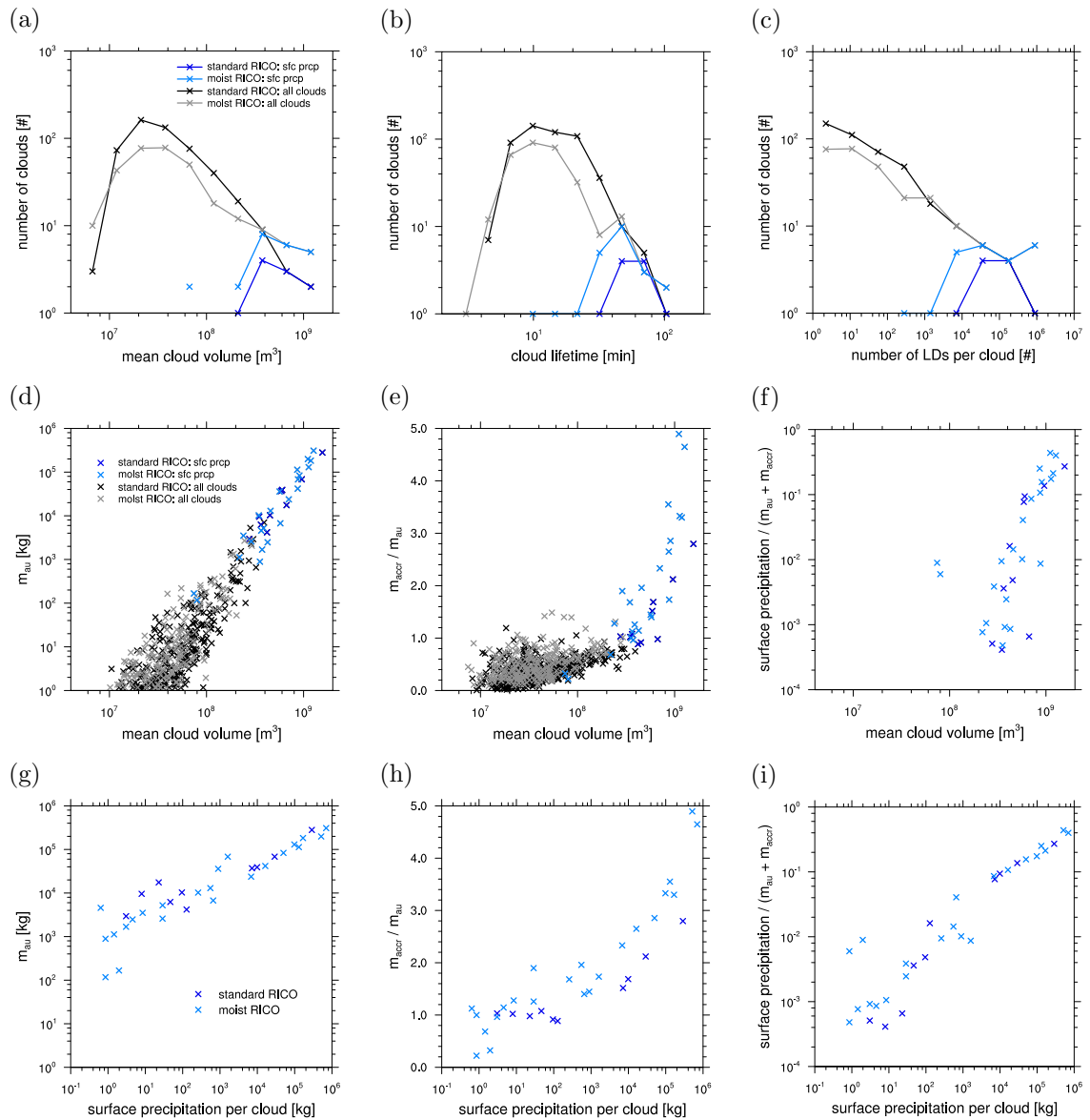


Figure 5.2.: Cloud properties. All statistics are calculated only for active clouds and only for those LDs that are associated with exactly one active cloud. Shown are histograms (a) for the mean cloud volume, (b) for the cloud lifetime and (c) for the number of LDs per cloud, and scatterplots (d,e,f) for the mean cloud volume and (g,h,i) for the amount of surface precipitation per cloud as a function of (d,g) the rainwater mass gained through autoconversion, m_{au} , (e,h) the relative contribution of accretion to autoconversion, $m_{\text{accr}}/m_{\text{au}}$, and (f,i) the efficiency of a cloud to produce surface precipitation from rainwater, surface precipitation $/ (m_{\text{au}} + m_{\text{accr}})$. Note the logarithmic size binning in (a,b,c).

droplet size distribution. Therefore their autoconversion rate remains low and no surface precipitation is produced. In contrast, the subset of those clouds that produce surface precipitation live distinctly longer, on average 62 min in the standard RICO simulation and 48 min in the moist RICO simulation.

As expected, the largest clouds gain the highest rainwater mass through autoconversion, m_{au} , and produce the highest amount of surface precipitation, although the spread is found to be surprisingly large (Fig. 5.2 d,g). This means that the mean cloud volume is a first indicator of the accumulated autoconversion rate of cloud water to rainwater during a cloud's lifetime, and that the accumulated autoconversion rate is a first indicator of the surface precipitation, but both do not determine the surface precipitation fully. Despite m_{au} also the relative contribution of accretion compared to autoconversion ($m_{\text{accr}}/m_{\text{au}}$, Fig. 5.2 e,h) and the efficiency of a cloud to produce surface precipitation from rainwater (surface precipitation/ $(m_{\text{au}}+m_{\text{accr}})$, Fig. 5.2 f,i) increase with increasing cloud volume and increasing surface precipitation. For those clouds that do not produce surface precipitation the rainwater mass gained through accretion is mostly smaller than the rainwater mass gained through autoconversion. Only for those clouds that produce surface precipitation, $m_{\text{accr}}/m_{\text{au}}$ increases rapidly (Fig. 5.2 e). This confirms the increasing importance of accretion over autoconversion as precipitation rates increase, which has also been found, e.g., by Gerber et al. (2008), Stevens and Seifert (2008) and Feingold et al. (2013). Note that the precipitation efficiency shown in Fig. 5.2 (f,i) differs from the usual definition of the precipitation efficiency (i.e., the surface precipitation normalised by the total condensate; e.g., Sui et al., 2007; Seifert and Stevens, 2010).

5.3.2. Lagrangian drop trajectory

A sample trajectory of an LD and some properties of the cloud it originates from are shown in Fig. 5.3. The LD originates near cloud top. After an initial ascent inside the cloud during which the LD's diameter increases, the LD is leaving the cloud near cloud top and descends in the cloud environment, where some of its mass evaporates. Then the LD reenters the cloud again, experiences a second updraft and a second period of diameter growth. During this second period the overall cloud volume and the cloud average cloud liquid water path start to decrease, while the average rainwater path of the projected cloud area increases. After a second height maximum the LD leaves the cloud again well above cloud base and some of its mass is evaporated while the LD is falling towards the subcloud layer and finally to the surface.

For the sample trajectory, the second updraft is essential for the overall growth of the LD and the simplified, conceptual picture of a raindrop that originates near cloud top, and then falls straight through the cloud and to the ground, is not valid in this case. We will show in the following that such an LD trajectory as outlined above with several height maxima and a last in-cloud height well above cloud base is typical in our simulations at least for a large portion of those raindrops that reach the surface.

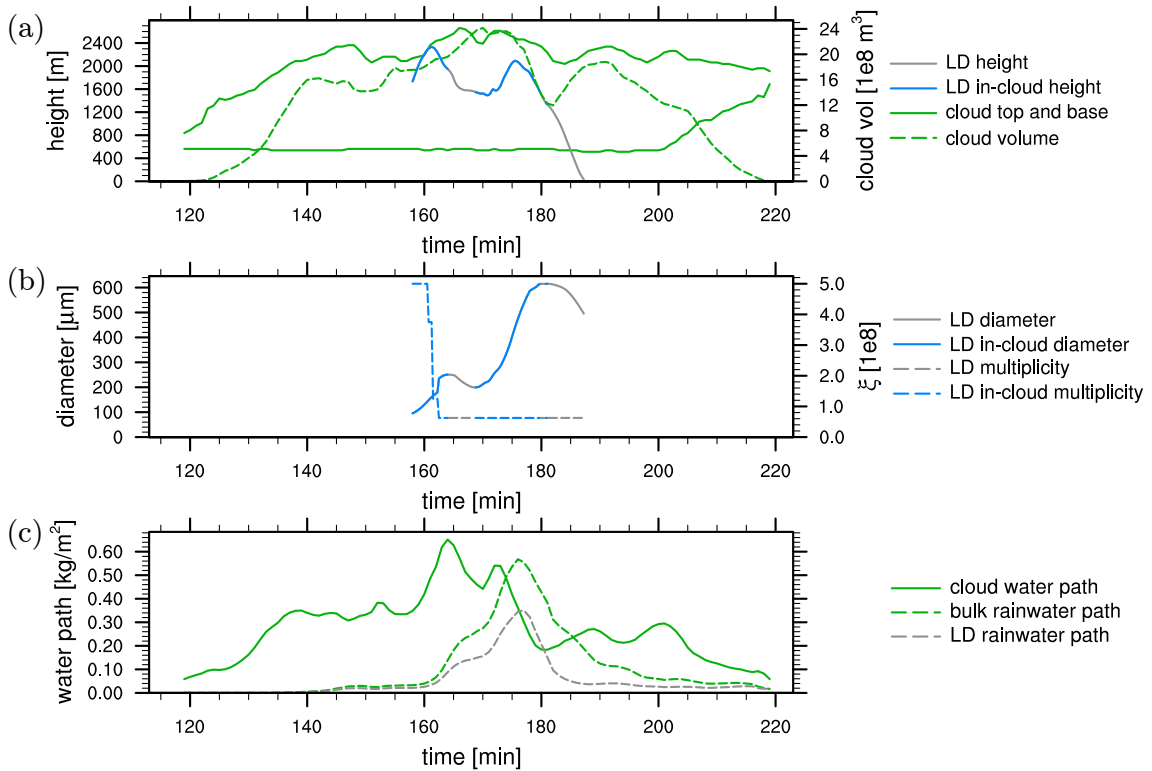


Figure 5.3.: Sample trajectory of an LD that originates from the cloud that is precipitating most in the moist RICO simulation. In addition, properties of that cloud are shown. More sample trajectories are shown in Appendix D.

5.3.3. Lagrangian drop statistics

While for the bulk rain microphysics scheme physical processes such as sedimentation, evaporation, accretion and selfcollection are parametrised in terms of an assumed RSD, in the LD model those processes only depend on the individual LD's velocity and size, and its environmental conditions (Sect. 3.3). In the following we will analyse the growth history of the LDs focusing on growth mechanisms that enable raindrops to reach the surface by comparing those LDs that reach the surface with those that evaporate before.

Most of the simulated LDs have a maximum diameter of less than $500 \mu\text{m}$ during their lifetime (Fig. 5.4 a) and evaporate completely when they leave the cloud. Only 1.2 % of the LDs from the standard RICO simulation and 3.1 % from the moist RICO simulation become so large that they reach the surface before evaporating completely. All LDs with a maximum diameter larger than $600 \mu\text{m}$ in the standard RICO simulations and with a diameter larger than $640 \mu\text{m}$ in the moist RICO simulation contribute to surface precipitation. Because the number of LDs is decreasing with increasing diameter, for both simulations most of the surface precipitation mass originates from rather small LDs with a diameter of less than 1.5 mm (Fig. 5.4 d).

Somewhat counterintuitively, it is not the LDs with the longest lifetime that grow largest

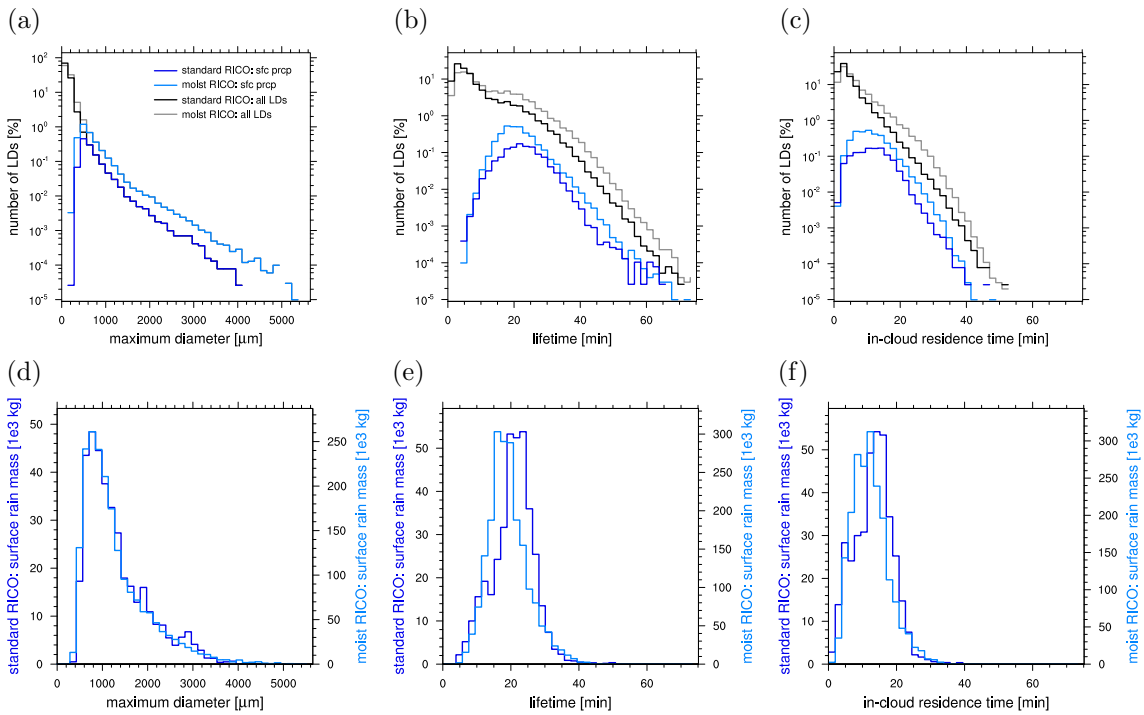


Figure 5.4.: Histograms of LD properties in terms of the number of LDs (upper row) and in terms of their contribution to surface precipitation mass (lower row).

(Fig. 5.4 b, also Fig. 5.7 a,b). Only a few of the LDs live as long as 1 hour, and most of the LDs have a lifetime of less than 10 min. Those that eventually contribute to surface precipitation, mostly reach the surface about 20 min after their initialisation. In general a raindrop can grow the larger the longer it lives, but large raindrops also sediment faster than smaller raindrops, which prevents a long lifetime because the large raindrops reach the surface faster. Although the in-cloud residence time determines the time an LD can grow by accretion, also the in-cloud residence time is not a sufficient criterion for the largest LDs (Fig. 5.4 c) due to vastly different cloud water contents within a cloud. Be reminded, that the LD's lifetime and in-cloud residence time represent the raindrop phase only, i.e., it excludes a prior cloud droplet lifetime, which is not simulated with the LD model.

Compared to the average lifetime of a cloud that produces surface precipitation (50 min to 60 min; Fig. 5.2 b), the average lifetime and in-cloud residence time of an LD that contributes to surface precipitation is distinctly shorter (20 min in Fig. 5.4 e and 15 min in Fig. 5.4 f, respectively). This difference is at least partly explained by the time that is needed for the broadening of the cloud droplet size distribution before the onset of autoconversion, i.e., the formation of raindrops.

The histograms of the LD's maximum diameter, its lifetime and its in-cloud residence time are similar for the standard RICO simulation and the moist RICO simulation but

some difference can be found in the details (Fig. 5.4): for the moist RICO simulation more LDs reach a large maximum diameter (Fig. 5.4 a) and the surface precipitation is contributed from LDs with an average lifetime and an average in-cloud lifetime that is about one minute shorter than for the standard RICO simulation (Fig. 5.4 e,f). We hypothesise that these small differences are related to a small shift in the relative importance of accretion and selfcollection, which we discuss in the following section.

5.4. Raindrop growth

5.4.1. Accretion and selfcollection

The overall growth of a raindrop by accretion can be quantified by

$$\left. \frac{dm}{dt} \right|_{\text{accr}} = E_c \pi \rho_a r_{\text{max}}^2 |\vec{v}_d - \vec{v}_a| q_c \quad (5.1)$$

as discussed in Sect. 3.3.3 (Eq. 3.7). Assuming that an LD is growing only by accretion and is not evaporating, its mass evolution can be described as a function of the cloud liquid water mixing ratio at the LD's position, q_c . To derive such an expression analytically, we approximate the collision-coalescence efficiency, E_c , by unity (as in Sect. 3.3.3), the air density, ρ_a , by the air density at a typical height for a raindrop, $\rho_{a,c} = 1.0 \text{ kg/m}^3$ (at about 2000 m), the maximum dimension of the drop, r_{max} , by its mass equivalent radius, r , i.e., the radius of the mass equivalent perfect sphere, and the difference between the LD velocity and the ambient flow velocity, $|\vec{v}_d - \vec{v}_a|$, by the LD's terminal fall velocity, v_t . For small raindrops with $40 \text{ } \mu\text{m} < r < 600 \text{ } \mu\text{m}$ an approximation of the terminal fall velocity is $v_t = k_v r$ where $k_v = 8 \times 10^3 \text{ s}^{-1}$ (Rogers and Yau, 1989, based on the data of Gunn and Kinzer 1949). Then Eq. 5.1 simplifies to

$$\left. \frac{dm}{dt} \right|_{\text{accr}} = \pi \rho_{a,c} k_v r^3 q_c \quad (5.2)$$

Furthermore, r is related to the LD's mass, m , by $r^3 = 3/(4\pi\rho_w)m$, where ρ_w is the liquid water density. Integrating Eq. 5.2 results in

$$\ln \left(\frac{m_{\text{accr}}}{\bar{m}_0} + 1 \right) = k_m Q_{c,\text{LD}} \quad \text{or} \quad (5.3)$$

$$\bar{r}_0 + r_{\text{accr}} = \bar{r}_0 \exp(k_r Q_{c,\text{LD}}) \quad (5.4)$$

where r_{accr} is the increase in LD radius due to accretion, $\bar{m}_0 = 3.9 \times 10^{-10} \text{ kg}$ is the mean initial mass of an LD and $\bar{r}_0 = 45.3 \text{ } \mu\text{m}$ is the corresponding mean initial mass equivalent radius of an LD. The factors k_m and k_r are $k_m = \frac{3\rho_{a,c}}{4\rho_w} k_v = 6.0 \text{ s}^{-1}$ and $k_r = \frac{1}{3} k_m$. The integral cloud water along the LD's trajectory, $Q_{c,\text{LD}}$, has been discussed by Feingold et al.

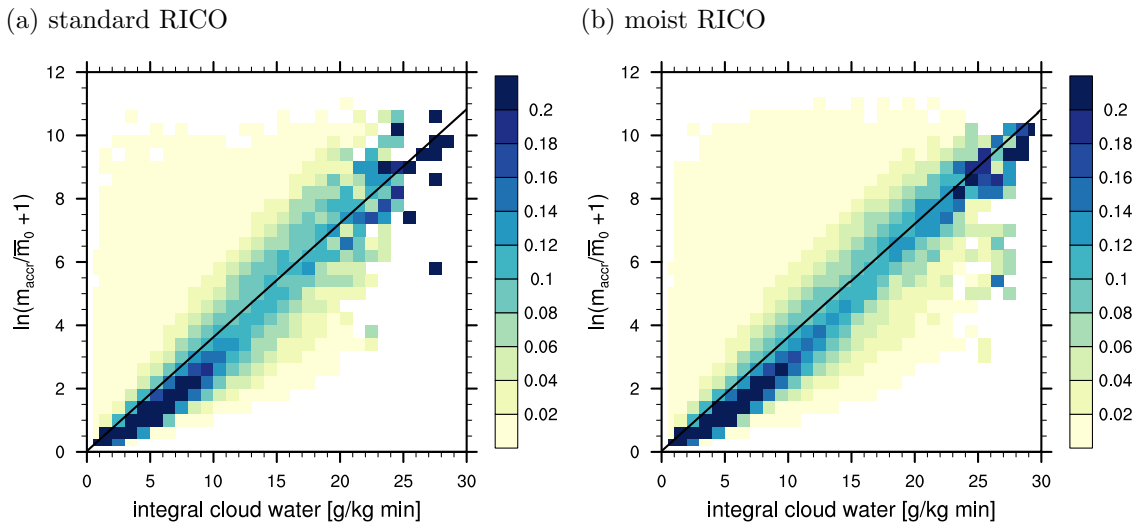


Figure 5.5.: Raindrop mass growth by accretion: PDF of $\ln(m_{\text{accr}}/\bar{m}_0 + 1)$ as a function of the integral cloud water, $Q_{c,\text{LD}}$. The solid line shows the relation from Eq. 5.3.

(2013) as a precipitation-controlling parameter and is defined as

$$Q_{c,\text{LD}} = \int_{t_0}^{t_1} q_c(\vec{x}) dt \quad (5.5)$$

where q_c is integrated over the lifetime of the LD from t_0 to t_1 and \vec{x} is the LD's position.

In Fig. 5.5 the LDs' mass gain by accretion is shown as a function of $Q_{c,\text{LD}}$ together with the relation from Eq. 5.3. For small $Q_{c,\text{LD}}$ the LD growth is slightly smaller than the analytical relation. This overestimation by the analytical relation is (at least partly) caused by the assumed dependence of v_t on r , which overestimates v_t slightly for small raindrops. Overall, $Q_{c,\text{LD}}$ is a good measure for the LD's mass gain through accretion. Consistently, for the standard and the moist RICO simulation all LDs that experience a large $Q_{c,\text{LD}} > 20$ g/kg min eventually contribute to surface precipitation (Fig. 5.6 a).

In addition to accretion, an LD's mass also grows by selfcollection, which is independent of the cloud water content but depends on the number density of LDs in the vicinity of that LD (and on luck). Normalising the LD growth through accretion by the maximum mass of the LD during its lifetime, two groups are found for those LDs that contribute to surface precipitation (Fig. 5.6 b,e): the first group of LDs with values around one gains mass mainly through accretion. The normalised LD growth through accretion can be larger than one if some of the LD's mass is evaporated before new mass is gained again through accretion. The second group with values close to zero dominantly grows from selfcollection. The accretion dominated LDs and the selfcollection dominated LDs seem to contribute about the same amount to the overall surface rain mass for the moist RICO simulation. For the standard RICO simulation a slight shift to the accretion dominated LDs can be found. If the maximum mass is small, the initial mass contributes an increasingly large

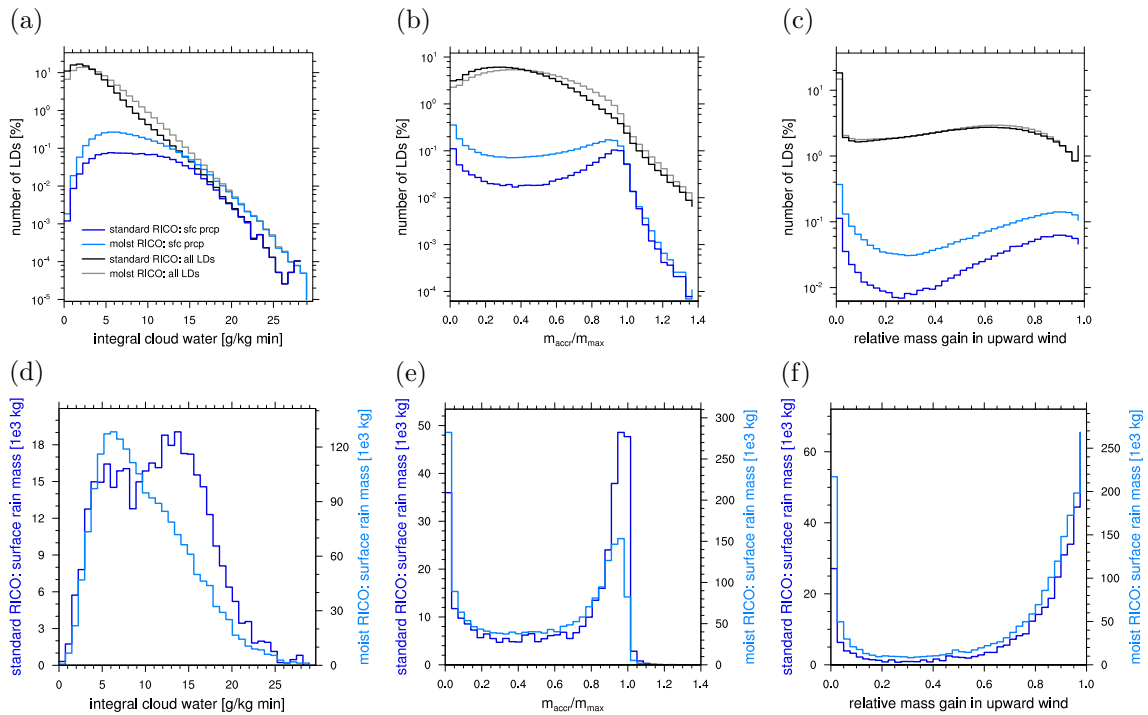


Figure 5.6.: Histograms of LD properties in terms of the number of LDs (upper row) and in terms of their contribution to surface precipitation mass (lower row).

portion to the maximum mass. Because most of the LDs have such a small maximum mass, this explains the relatively broad maximum at low values when all LDs are considered.

The two branches found for the LD lifetime and the integral cloud water for the standard RICO simulation are also associated with the two growth regimes (Fig. 5.7 a,c). For pure accretional growth, the maximum diameter increases with the integral cloud water. Because selfcollection is independent of the integral cloud water, a second branch with low integral cloud water is found for all LD sizes. A corresponding two-branch behaviour can be found for the LD's lifetime. If selfcollection becomes more important for the growth rate, the LD's lifetime can be distinctly reduced. For the moist RICO simulation, the two branches cannot be found and the integral cloud water seems to display the increasing importance of selfcollection compared to the standard RICO simulation (Fig. 5.7 b,d).

For most of those LDs that contribute to surface precipitation, growth predominantly takes place in updraft regions (Fig. 5.6 c,f). In a cloud, liquid water forms in the updraft region and therefore growth through accretion is effective there. However, there is a second peak that contributes to surface precipitation, where LDs only gain a small fraction of their mass in updraft conditions. Here, the individual LD mostly grow from selfcollection.

For a given RSD, the change in the mean raindrop mass, $\bar{m} = q_r/n_r$, can be characterised by the change in rainwater mixing ratio, q_r , and the change in raindrop number density,

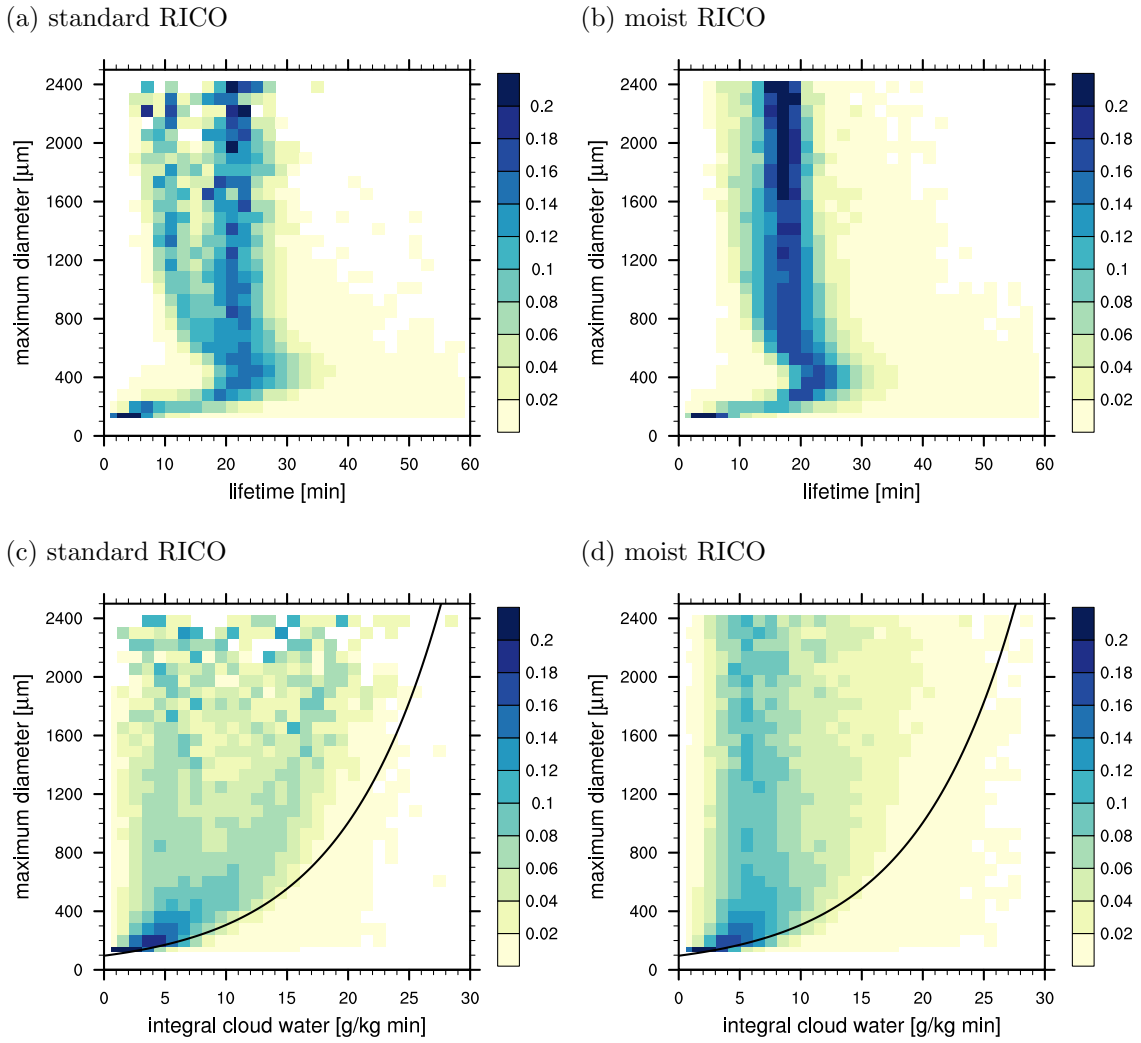


Figure 5.7.: PDFs of the lifetime and of the integral cloud water as a function of the maximum diameter. The solid line in (c,d) shows the relation of Eq. 5.4.

n_r :

$$\frac{\partial \bar{m}}{\partial t} = \frac{\partial}{\partial t} \left(\frac{q_r}{n_r} \right) = \frac{1}{n_r} \frac{\partial q_r}{\partial t} - \frac{q_r}{n_r^2} \frac{\partial n_r}{\partial t} \quad (5.6)$$

Accretion is changing q_r while n_r stays constant. Vice versa, selfcollection is changing n_r while q_r stays constant.

$$\left. \frac{\partial \bar{m}}{\partial t} \right|_{\text{accr}} = \frac{1}{n_r} \left. \frac{\partial q_r}{\partial t} \right|_{\text{accr}} \quad \text{and} \quad \left. \frac{\partial \bar{m}}{\partial t} \right|_{\text{sc}} = - \frac{q_r}{n_r^2} \left. \frac{\partial n_r}{\partial t} \right|_{\text{sc}} \quad (5.7)$$

Using the parametrisation for accretion and selfcollection from Seifert and Beheng (2001), the ratio, $f_{\bar{m}}$, of the mean raindrops mass gain through accretion to the mean raindrop mass gain through selfcollection can be expressed as the ratio of the cloud water mixing

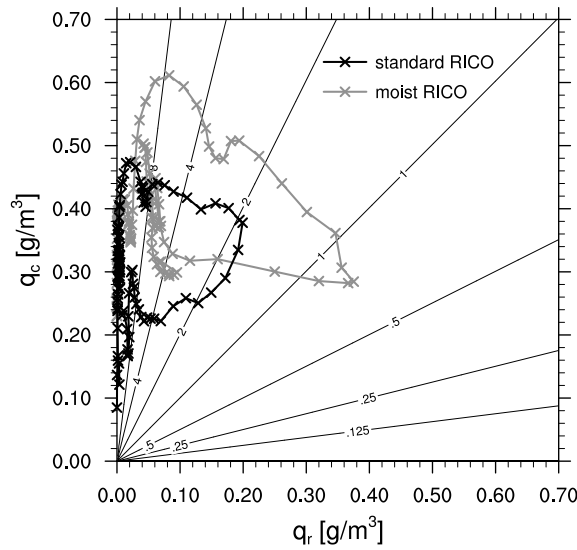


Figure 5.8.: Ratio $f_{\overline{m}}$ according to Eq. 5.8 as a function of q_c and q_r (labelled lines). Cloud mean values of q_c and q_r are shown for two selected clouds: those two clouds that form the most surface precipitation in the standard RICO simulation and in the moist RICO simulation. The temporal resolution for the mean cloud values is one minute and the temporal development is in clockwise direction for both clouds.

ratio to the rainwater mixing ratio:

$$f_{\overline{m}} = \frac{\frac{\partial \overline{m}}{\partial t} \Big|_{\text{accr}}}{\frac{\partial \overline{m}}{\partial t} \Big|_{\text{sc}}} = \frac{q_c}{q_r} \phi_{\text{accr}}(\tau) \quad (5.8)$$

The universal function ϕ_{accr} provides considerable contribution only for very small $\tau = 1 - q_c/(q_c + q_r)$.

Fig. 5.8 shows the temporal development of the cloud mean values of q_c and q_r for those two clouds that produce most surface precipitation in the standard and the moist RICO simulation. For both clouds, q_c increases rapidly when the cloud is forming. Then, as autoconversion and accretion set in, q_r increases at the expense of q_c . At the end of a cloud's lifecycle, both q_c and q_r decrease and the cloud disappears. For the cloud from the standard RICO simulation, q_r is always smaller than q_c , i.e., $f_{\overline{m}}$ is always > 1 . For the moist RICO cloud for about 5 min $f_{\overline{m}} < 1$, i.e., $q_r > q_c$ (compare to Fig. 5.3 c). Although local values at an LD's position may deviate substantially from cloud mean values and selfcollection may also take place outside the cloud, this confirms the more important role of selfcollection in the moist RICO simulation compared to the standard simulation.

5.4.2. The role of recirculation

After discussing the microphysical processes of raindrop growth in the previous section, we now focus on the dynamical aspects of a raindrop's lifecycle. Similar to the LD trajectory

Table 5.2.: Percentage of LDs that recirculate or hop between updrafts at least once.

RICO simulation	all LDs		sfc prcp LDs	
	standard	moist	standard	moist
cloud-edge recirculation	13	16	66	47
200-m recirculation	3	4	38	22
updraft hopping	2	2	1	1

sfc prcp LDs – surface precipitating LDs, i.e., considering only those LDs that eventually contribute to surface precipitation

shown in Fig. 5.3 and those in Appendix D, many of the LDs and in particular those LDs that eventually reach the surface are found to *recirculate* in the cloud layer, i.e., many LDs do not fall straight towards the surface but leave and reenter a cloud, and experience several height maxima during their lifetime. To analyse the *recirculation* of an LD in a quantitative way, we formulate two definitions of recirculation, one highlighting the horizontal displacement of an LD and one highlighting the vertical displacement of an LD:

cloud-edge recirculation An LD is recirculating if during its lifetime it is undergoing the consecutive events of being outside the cloud, having a height maximum within the cloud and being outside the cloud again.

200-m recirculation An LD is recirculating if during its lifetime it is undergoing consecutive periods of descent and ascent, each time achieving a height difference of at least 200 m.

The two definitions of recirculation do not exclude each other and one LD may undergo several recirculations of each type during its lifetime. For the second definition, the threshold of 200 m for the minimum height difference is chosen because a threshold should be reasonably small to include most recirculations but at the same time should be considerably larger than the vertical grid spacing of 25 m. For the LD in Fig. 5.3, these definitions yield one cloud-edge recirculation and one 200-m recirculation, both referring to the height maximum between 170 min and 180 min.

In addition, we define updraft hopping:

updraft hopping An LD is hopping between updrafts if during its lifetime it is found inside two different active clouds, i.e., during its lifetime an LD is switching from the cloudy area that is attributed to one cloud core to the cloudy area that is attributed to another cloud core.

The two active clouds an LD is found in might be single clouds or parts of a multicore cloud system. Defining updraft hopping as switching between cloud cores instead of clouds would be an even more restrictive conditions, which is not applied here.

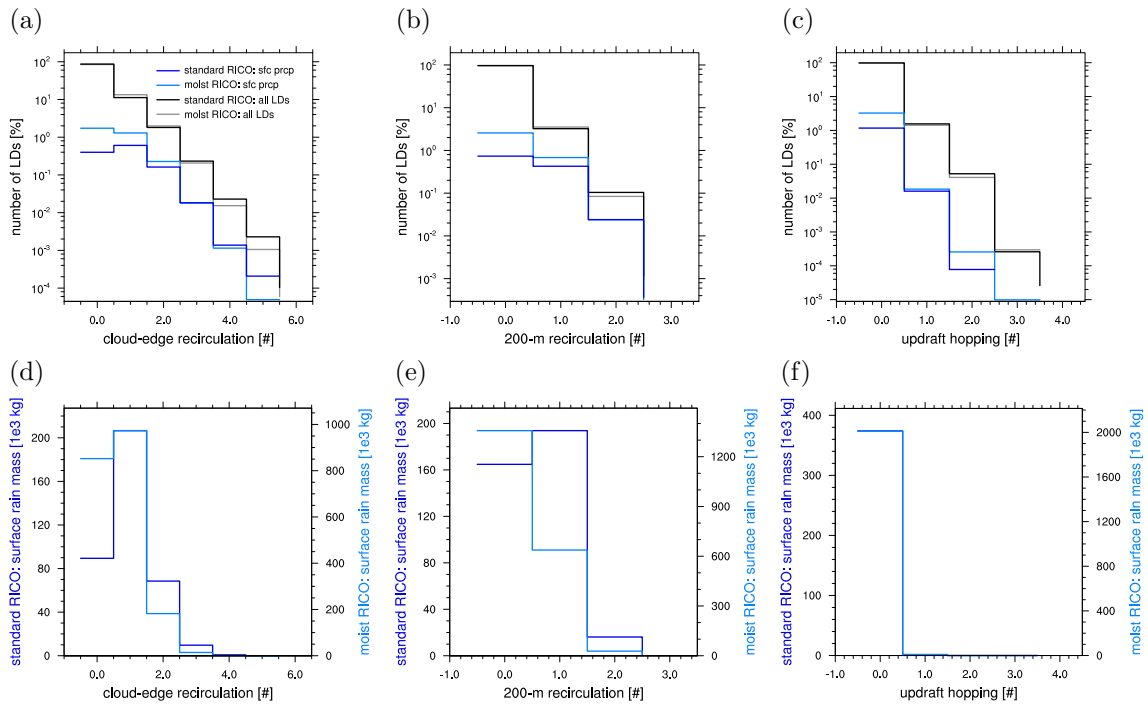


Figure 5.9.: Histograms of LD properties in terms of the number of LDs (upper row) and in terms of their contribution to surface precipitation mass (lower row).

For both definitions of recirculation, we find that considering all LDs the majority of LDs does not recirculate (Table 5.2) and that the percentage of LDs that recirculate is decreasing steadily with increasing number of recirculations at a very similar rate for the standard and the moist RICO simulation (Fig. 5.9 a,b). In contrast, for the subsample of those LDs that eventually reach the surface and for the cloud-edge recirculation, about as many LDs do not recirculate as recirculate at least once (Fig. 5.9 a). For both RICO simulations, those LDs that experience at least one cloud-edge recirculation contribute more to the surface rain mass than those that do not recirculate, though the difference is larger for the standard RICO simulation (Fig. 5.9 d). For the 200-m recirculation the statistics are similar, albeit high numbers of recirculation are less common (Fig. 5.9 b). For the moist RICO simulation, LDs that do not experience a 200-m recirculation contribute more mass to surface precipitation than those that recirculate once or more often (Fig. 5.9 e). The precise numbers differ depending on the definition of recirculation but overall we find that recirculation of raindrops is common in shallow cumulus, especially for those LDs that contribute to surface precipitation.

Applying the cloud tracking, we find that most of the LDs stay in the cloudy updraft region they originate from and do not hop between updrafts, regardless if they contribute to surface precipitation or evaporate before they reach the surface (Table 5.2 and Fig. 5.9 c). This also holds in terms of surface precipitation mass, i.e., those few LDs that make it to a second cloud do not contribute distinctly to the surface precipitation (Fig. 5.9 f).

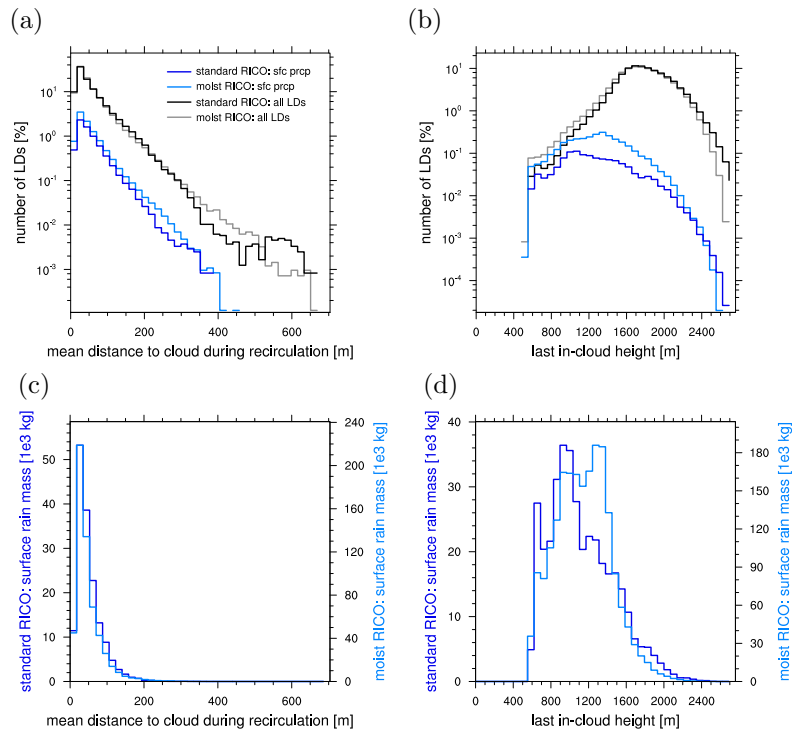


Figure 5.10.: Histograms of LD properties in terms of the number of LDs (upper row) and in terms of their contribution to surface precipitation mass (lower row).

The dynamical aspects of an LD's trajectory can be further characterised by relating the LD's position and flow properties to the cloud it originates from. During a cloud-edge recirculation event the LDs depart from the cloud. For most of the LDs the mean distance to the cloud edge during a cloud-edge recirculation event is less than 50 m for the period that the LD is outside the cloud (Fig. 5.10 a). The portion of LDs is decreasing rapidly with increasing mean distance to the cloud edge. Nevertheless, LDs with mean distances up to 200 m contribute to surface precipitation (Fig. 5.10 c).

While most of the LDs originate near cloud top between 2000 m and 2500 m, the last in-cloud height for most of the LDs is only a couple of hundred meters lower (Fig. 5.10 b). For the subset of LDs that eventually contribute to surface precipitation, the last in-cloud height is typically about 1000 m below their initial height, around 1000 m for the standard RICO simulation and around 1400 m for the moist RICO simulation (Fig. 5.10 d). Only few LDs leave the cloud through cloud base, which for both simulations is at 600 m.

That most LDs leave the cloud laterally and that a portion of them is able to reenter the cloud, suggests that the LD motion is not bound to the cloud structure. The notion of an LD that resides in a cloud core updraft like in an elevator, and ascends and descends as the core is pulsating in strength therefore is not a reasonable explanation of the observed LD recirculation. The vertical velocity of the sample trajectory (introduced in Fig. 5.3) is clearly more variable than the cloud average in-cloud vertical velocity or the

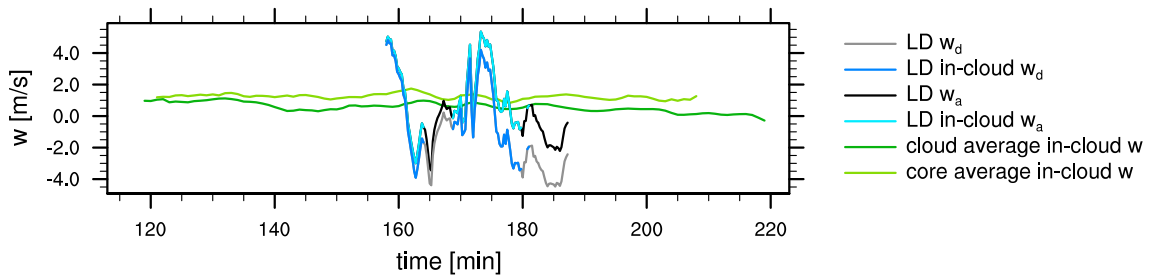


Figure 5.11.: Vertical velocities for the sample trajectory in Fig. 5.3. Shown are the LD’s vertical velocity, w_d , the vertical flow velocity at the LD’s position, w_a , and the column average in-cloud vertical velocity, w , averaged over the cloud area or the core area.

(a) standard RICO

(b) moist RICO

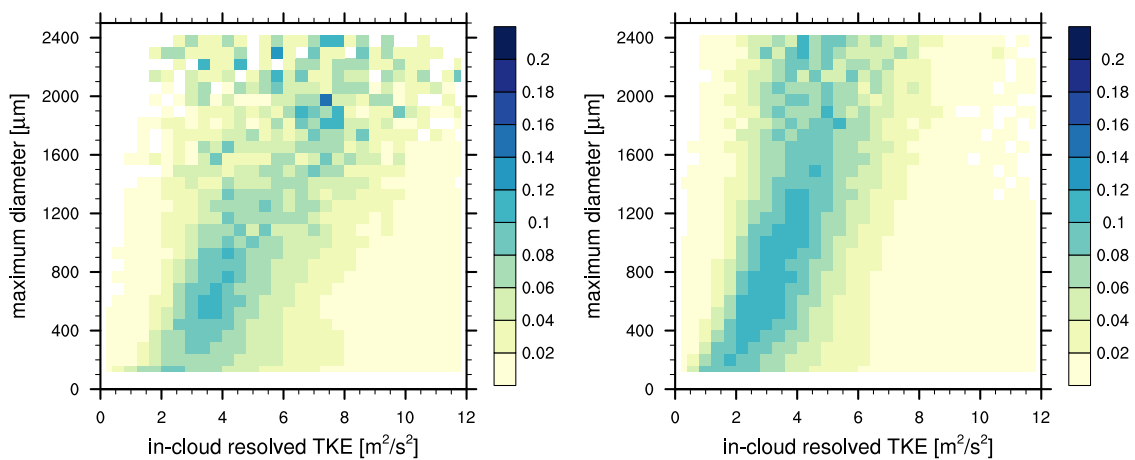


Figure 5.12.: PDFs of the in-cloud resolved TKE along the LD’s trajectory as a function of the maximum diameter.

core average in-cloud vertical velocity, and does not agree well with the cloud average or core average vertical velocity tendencies, maxima or minima (Fig. 5.11). For both RICO simulations, the LD diameter increases with increasing in-cloud TKE along the LD trajectory (Fig. 5.12). This suggests that the LDs are able to switch between different updraft structures on the sub-cloud scale, and that it is not the mean cloud properties alone that determine the raindrops growth but that the in-cloud variability is crucial.

Finding that recirculation is common, it is interesting to analyse how much of the surface precipitation a cloud is producing is actually contributed from those LDs that recirculate and how much those LDs grow during recirculation. To approach this questions, we estimate an upper bound and a lower bound of the surface precipitation contributed by recirculating LDs and compare it to the total precipitation. To estimate an upper bound, we sum the contribution to the surface precipitation from that subsample of LDs that recirculate. However, those LDs that recirculate may be large enough to contribute to surface precipitation already before the (first) recirculation event sets in. To estimate a

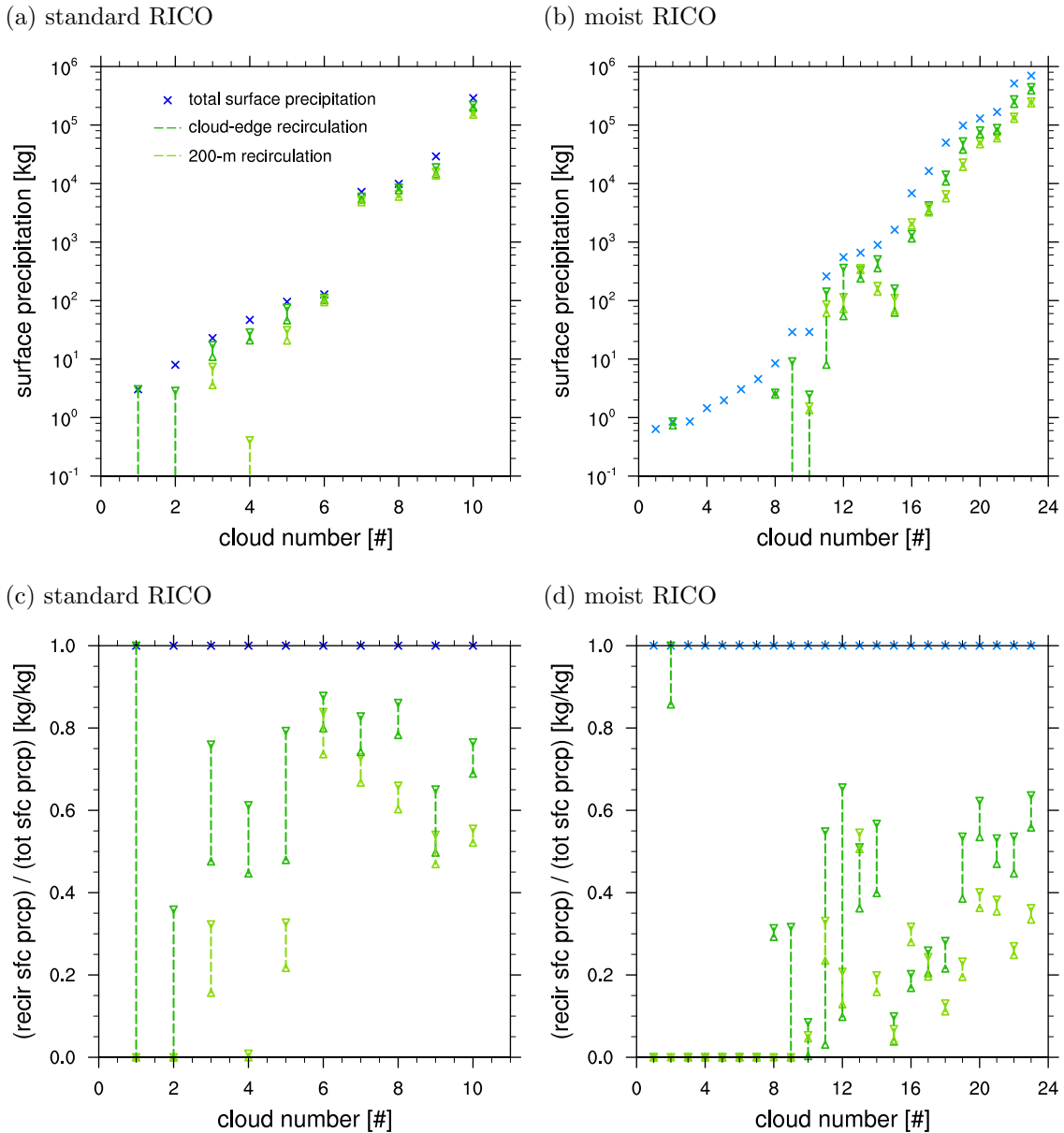


Figure 5.13.: Total surface precipitation per cloud and relative contribution of recirculating LDs to the total precipitation. Triangle top down: contribution to surface precipitation only by those LDs that recirculate. Triangle top up: surface precipitation by those LDs that recirculate minus the mass of those LDs that recirculate at their height minimum before the recirculation.

lower bound, we therefore subtract from the upper bound estimate the mass of those LDs that recirculate at the moment they reach the last height minimum before the recirculation event. This lower estimate is not in every case a true lower bound because without a recirculation a raindrop could still grow while falling further through the cloud if the height minimum is inside a cloud. We suspect this growth effect to be very small because the descent before the recirculation is often outside the cloud (Fig. 5.9) and

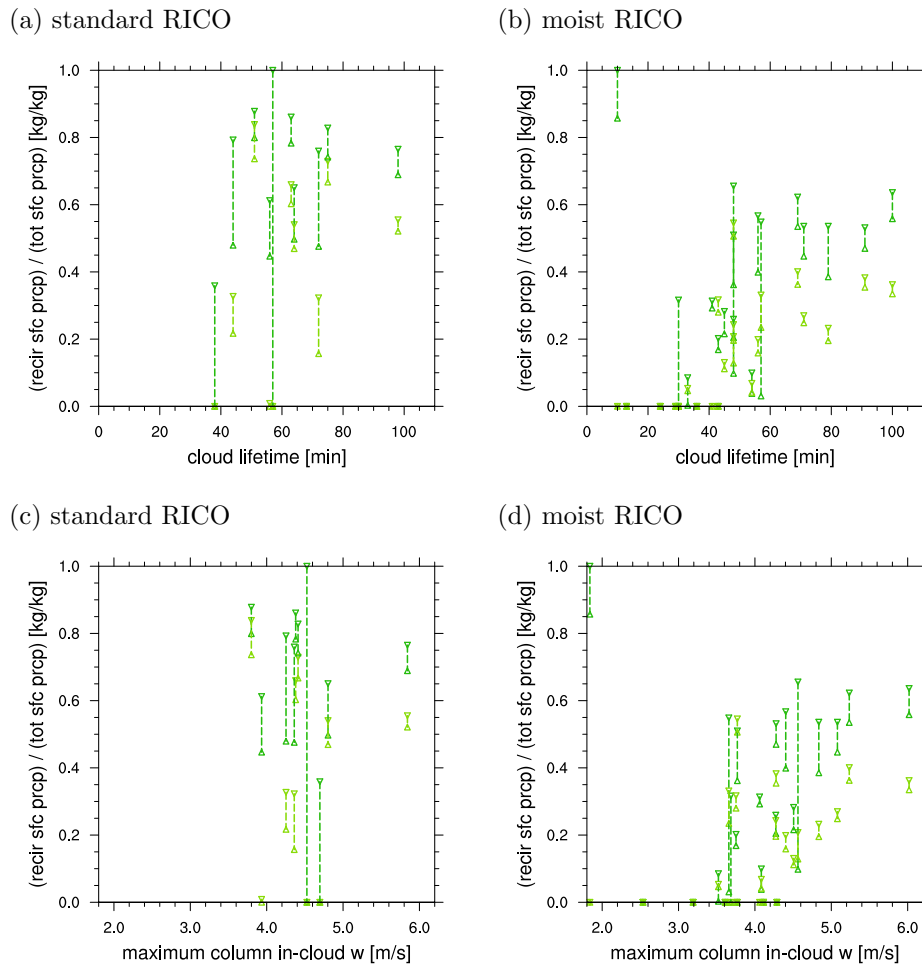


Figure 5.14.: The relative contribution of recirculating LDs to the total precipitation as a function of the cloud lifetime and the maximum of the column average in-cloud vertical velocity. Meaning of markers and colors as in Fig. 5.13.

because as the last in-cloud height is rarely close to cloud base the potential growth path is short (Fig. 5.10). In addition, evaporation in the cloud environmental air and in the subcloud layer, which is not considered in the estimate, decreases the LD's mass rather than increasing it.

Using those estimates for the upper and the lower bound, we find that the difference between the upper and lower bound for most clouds is much smaller than the difference between different clouds (Fig. 5.13). For the cloud-edge recirculation, the contribution of the recirculating LDs to the surface precipitation is slightly higher than for the 200-m recirculation, which is reasonable because the cloud-edge recirculation is more frequent. For both definitions of recirculation and especially for the moist RICO simulation, the surface precipitation amount per cloud is the higher, the higher the contribution of the recirculating LDs is. For the most precipitating clouds, the LDs that recirculate can contribute more than 50 % to the total surface precipitation (Fig. 5.13 d). For the whole

cloud field, the contribution of recirculating LDs to the overall surface precipitation rate is dominated by those clouds that produce the highest amount of surface precipitation (Fig. 5.13 a,b): for the standard RICO simulation, the contribution of the recirculating raindrops to the total surface precipitation is 72 % for the cloud-edge recirculation and 54 % for the 200-m recirculation; for the moist RICO simulation, it is 53 % for the cloud-edge recirculation and 31 % for the 200-m recirculation. This implies that coarse resolution models that do not resolve those eddies that cause recirculation of raindrops omit a relevant process of rain formation in shallow cumulus. It might also be one reason for the slow convergence of LES for precipitating shallow convection.

Comparing both RICO simulations, the contribution of recirculating LDs to the total surface precipitation is smaller for the moist RICO simulation (Fig. 5.13 c,d), which is characterised by a higher mean surface precipitation rate than the standard RICO simulation (Table 5.1). This is somewhat surprising because, as discussed above, the contribution of recirculating LDs to the total surface precipitating per cloud is increasing with increasing surface precipitation per cloud. We speculate that the smaller contribution for the moist RICO simulation is related to the larger relative contribution of selfcollection compared to accretion for the moist RICO simulation and the slightly longer LD lifetime for the standard RICO case.

For a parametrisation of the effect of recirculation, a relation of the contribution of the recirculating raindrops to some model parameter is needed. We find no hint for such a relation for the spatial extent of the cloud, e.g., for the cloud height or the cloud volume, which might be related to the rather small cloud height differences in the simulations. But the contribution of the recirculating raindrops to the overall precipitation roughly increases with increasing cloud lifetime and with increasing maximum of the column average in-cloud vertical velocity for the moist RICO simulation (Fig. 5.14 b,d). For the standard RICO simulation, the relations are less marked (Fig. 5.14 a,c). Overall, the development of a parametrisation that takes into account the effect of recirculation needs further investigation but a relation to the cloud lifetime or to the cloud updraft strength seems to be a useful starting point.

5.5. Conclusions

In this chapter, we investigate the growth history of raindrops in lightly precipitating shallow cumulus. Two related cases of fields of shallow cumulus are simulated using an LES combined with an LD model for raindrop growth and a cloud tracking algorithm. Overall 1.4×10^7 LDs are simulated and more than 800 clouds are tracked of which 33 produce surface precipitation. We find that a first estimate of the amount of surface precipitation per cloud can be inferred from the accumulated autoconversion rate during a cloud's lifetime but the accumulated autoconversion rate does not determine the surface

precipitation fully. Instead, we find considerable spread among individual clouds.

In our simulations, 1 % to 3 % of the LDs but all of those with a maximum diameter larger than $640 \mu\text{m}$ reach the ground as surface precipitation. Most of the LDs have a lifetime of less than 10 min. The subsample of those LDs that contribute to surface precipitation live considerably longer, on average about 20 min. The largest LDs do not have the longest lifetime or longest in-cloud residence time because larger raindrops sediment faster and therefore also reach the ground faster.

Two processes determine raindrop growth: accretion of bulk cloud water and selfcollection among raindrops. For the standard RICO simulation, the two regimes can be clearly identified: in the first regime, growth is dominated by accretional growth and the size of the LDs is closely related to the integral cloud water along their trajectory. In the second regime, selfcollection has a more important role, the size of the LDs is independent of the integral cloud water and the LDs have a shorter lifetime compared to the accretional growth regime.

We find that raindrop trajectories in shallow cumulus can be quite complex. The LDs typically leave the cloud well above cloud base, and a substantial part especially of those LDs that contribute to surface precipitation leave and then reenter the same cloud for an additional updraft period. Accordingly, those trajectories often feature several height maxima, and the LD properties are less influenced by cloud-mean properties but the in-cloud variability is crucial. The fraction of surface precipitation that can be attributed to such recirculating LDs is variable from cloud to cloud but seems to increase with increasing surface precipitation amount and can be larger than 50 % per cloud. This implies that the traditional, conceptual picture of a raindrop that originates near cloud top, that then gains mass while it falls straight through the cloud without any recirculation and that finally leaves the cloud at cloud base falling further to the ground, is too simplified especially for those raindrops that eventually contribute to surface precipitation. Highly idealised one-dimensional models of rain formation that neglect the recirculation of raindrops and models with coarse resolution that do not resolve those eddies that cause recirculation of raindrops therefore omit a relevant process that contributes distinctly to surface precipitation.

CHAPTER 6

CONCLUSIONS

If we are all the same,
we'd go out there and make rain.

(Super700)

6.1. Developed models and methods

This thesis employs high-resolution numerical modelling to investigate the representation of shallow clouds in large-scale atmospheric models and the processes that lead to formation of precipitation.

Based on two LES case studies of different shallow cloud regimes and observational data from aircraft measurements in shallow cumulus, we identify deficiencies in existing PDF-based cloud parametrisations to represent the shallow cumulus regime adequately. Starting from the parametrisation scheme of Larson et al. (2001a), we suggest a revised set of closure equations that correctly captures the cloud structure of both the stratocumulus and the shallow cumulus regime. Simulations of two additional LES case studies are used as perfect input data to the cloud scheme for a priori testing of the modified closure equation and those originally proposed by Larson et al. (2001a).

To investigate the particle-kinetic processes of rain formation in shallow cumulus, a Lagrangian drop (LD) model is developed that includes all relevant processes for rain-

drop growth such as accretional growth from cloud water, selfcollection among raindrops, evaporation and sedimentation. The LD model is related to the super-droplet method (Andrejczuk et al., 2008; 2010; Shima et al., 2009; Riechelmann et al., 2012) but adapted to better represent the raindrop phase by two major differences: First, instead of focusing on the early cloud droplet growth, the LD model simulates only raindrop growth after autoconversion from cloud droplets. For the super-droplet method, an adequate representation of the tail of the drop size distribution, which is decisive for precipitation characteristics, is challenging because cloud droplets are orders of magnitude more numerous than raindrops. With the LD model we specifically target to analyse the growth history of raindrops after the initial formation of drizzle drops. Second, the LD model is not implemented to replace the Eulerian bulk rain microphysics scheme but the Eulerian LES is run including all microphysics, which allows for a consistent comparison of the bulk rain microphysics and the LD statistics.

The LD model is intended to be used as a tool to understand warm rain microphysical processes on a particle-based level. To test whether the LD model is fit for purpose and to examine uncertainties related to the formulation of the dynamical and microphysical processes in the LD model, a sensitivity study is conducted for two isolated shallow cumulus clouds. In addition, the uncertainties of the LD model are compared to uncertainties inherent in a common bulk microphysics scheme.

The LD model is then applied to study the RSD in isolated shallow cumulus clouds. The development of the shape of the RSD is analysed in relation to the cloud's lifecycle and findings are compared to the assumed shape of the RSD in bulk rain microphysics schemes.

Finally, the growth history of raindrops, the relative importance of accretion and self-collection, and the role of recirculation are studied by analysing the trajectories of LDs in a field of shallow cumulus. We are the first to combine a Lagrangian microphysics model with a cloud tracking algorithm (Heus and Seifert, 2013). In this way we are able to study the growth history of LDs in relation to the lifecycles of individual clouds, which the LDs are attributed to.

6.2. Results

In the following the results of this thesis are summarised by answering the research questions raised in the introduction (Chapter 1).

How can the characteristics of different cloud regimes be taken into account in the parametrisation of the cloud fraction?

We find that the PDF of the extended liquid water mixing ratio has a heavier tail for positively skewed PDFs representing shallow cumulus than for negatively skewed PDFs representing stratocumulus. This characteristic behaviour of the PDFs depicts the more

vigorous nature of updrafts in shallow cumulus compared to the weaker downdrafts in stratocumulus and is taken into account in a cloud parametrisation by introducing a break in the antisymmetric closure equations suggested by Larson et al. (2001a). The new set of closure equations represent the updrafts in shallow cumulus more adequately and a priori tests of the cloud parametrisation show that the errors in cloud fraction and liquid water mixing ratio are reduced in the shallow cumulus regime compared to the original formulation.

Can PDF-based parametrisations be extended to diagnose microphysical process rates?

If a microphysical process rate is well described as a function of a bulk variable such as the liquid water mixing ratio, a PDF-based parametrisation is a sensible approach to take into account the effect of the subgrid-scale variability of the bulk variable on the microphysical process rate. For instance, the autoconversion rate is often parametrised as a function of the bulk liquid water mixing ratio (Kessler, 1969; Khairoutdinov and Kogan, 2000; Seifert and Beheng, 2001) but depends (at least) also on the cloud droplet size distribution. Using different parametrisations of the dependence of the autoconversion rate on the liquid water mixing ratio, a PDF-based parametrisation is able to reproduce profiles of the mean autoconversion rate adequately. But the differences between the different parametrisations of the autoconversion rate are substantial. Even for relatively simple parametrisations of the autoconversion rate, which in addition to the dependence on the liquid water mixing ratio take into account a dependence on the cloud droplet number density, the joint PDF of those two variables would be needed.

How sensitive is the LD model to the representation of dynamical and microphysical processes and how do the uncertainties in the LD model compare to uncertainties in a bulk rain microphysics scheme?

The surface precipitation rate and the slope of the RSD simulated by the LD model are especially sensitive to the treatment of selfcollection in the LD model. Some uncertainty remains for the contribution of the subgrid-scale turbulence to the relative velocity difference of a pair of LDs, which appears as a factor in the collision rate. Sensitivities to other model parameters such as the initial multiplicity or the initial mass distribution are small for the two shallow cumulus clouds simulated ($< 30\%$ in terms of the amount of surface precipitation). The uncertainties in the formulation of the LD model are clearly smaller than uncertainties inherent in the bulk rain microphysics due to the assumption on the shape of the RSD or due to the prescribed cloud droplet number density (up to an order of magnitude in terms of the amount of surface precipitation). Therefore, we conclude that the LD model introduced in Chapter 3 is a valuable tool to understand raindrop growth and dynamics in shallow cumulus.

How does the RSD develop in the course of the lifecycle of a shallow cumulus cloud?

With the LD model the development of the RSD can be studied in a less idealised setup than previous studies have applied (Milbrandt and Yau, 2005; Seifert, 2008). The first raindrops in the course of a cloud's lifecycle appear near cloud top and the initial RSD is narrow, which is quantified by large values of the shape parameter of a gamma distribution representing the RSD ($\mu > 10$). With time and with decreasing height, the RSD is ageing and broadening ($\mu < 3$), and the mean raindrop diameter is increasing in the LD model. For a simple single-pulse shallow cumulus cloud, we find that the RSD in the subcloud layer is initially narrow because the largest raindrops reach the subcloud layer first due to gravitational sorting. With time the RSD broadens and the mean raindrop diameter decreases in the subcloud layer. For a more complex multi-pulse cloud, no extensive gravitational sorting in the subcloud layer is found, which is related to a more diverse development of the multi-pulse cloud.

Is the development of the shape of the RSD in shallow cumulus well represented in the closure equation of a two-moment bulk rain microphysics scheme?

No. For more heavily precipitating cases Seifert (2008) also found a V-shaped behaviour, but for shallow cumulus the position of the V-shape is substantially shifted towards smaller mean raindrop diameters in the LD model. Therefore, commonly used closure equations such as those suggested by Milbrandt and Yau (2005) or by Seifert (2008) are not appropriate for shallow cumulus clouds. The differences found for the development of the shape of the RSD for individual shallow cumulus clouds and the clear dependence on the cloud's lifecycle shows that a parametrisation of the shape of the RSD as a function of the mean raindrop diameter is not sufficient, especially if different cloud regimes and different complexities of cloud lifecycles are considered. Instead, the stage of the cloud's lifecycle should be taken into account in a closure equation that describes the development of the shape of the RSD.

Is recirculation and updraft hopping of raindrops common in shallow cumulus and how much do recirculating raindrops contribute to surface precipitation?

Simulations of a field of shallow cumulus clouds with the LD model show that raindrops mostly stay in the cloudy updraft region they originate from and do not hop between different updrafts. In contrast, recirculation of raindrops associated with the same cloudy region is common, especially for those raindrops that contribute to surface precipitation. The fraction of surface precipitation per cloud that is contributed by recirculating raindrops increases with increasing surface precipitation up to roughly 50 %. Depending on the definition of recirculation and on the relative importance of accretion and selfcollection for the raindrop growth, the contribution of recirculating raindrops to the total surface precipitation of a field of shallow cumulus varies between 30 % and 70 %. To our knowledge

this is the first quantitative estimate for the effect of recirculating raindrops in shallow cumulus. It implies that models with coarse resolution that do not resolve those eddies that cause recirculation of raindrops omit a relevant process of rain formation.

6.3. The next steps

A posteriori testing of the cloud scheme

For the proposed refinement of the closure equations of a PDF-based cloud parametrisation a posteriori tests in the target model – an NWP model or a GCM – are the natural next step. To apply the proposed refined cloud parametrisation (or the original parametrisation by Larson et al., 2001a) in a large-scale model, the first three moments of the PDF of the extended liquid water mixing ratio have to be predicted or diagnosed for each grid box. While the first two moments are commonly available in NWP models and GCMs, especially the third moment is difficult to obtain (Gryanik and Hartmann, 2002; Gryanik et al., 2005; Mironov, 2009; Machulskaya and Mironov, 2013; Schemann, 2014).

A priori tests as done in Chapter 2 are useful to understand the behaviour of the parametrisation in simple idealised conditions and with perfect input data. In contrast, a posteriori tests are essential for an understanding of the parametrisation when it is coupled to the full model and exposed to more complicated real-case meteorological situation. A final parametrisation selection should only be done by taking a priori tests and a posteriori tests into account.

Extension of the LD model

The LD model introduced in Chapter 3 provides a framework for rain microphysical studies on a particle based level. Four extensions of the framework are discussed in the following.

As described in Chapter 3 the LD model does not feed back on the Eulerian temperature, humidity and momentum fields. A first extension of this thesis therefore is to include a two-way coupling of the LD model to the Eulerian LES. Similar to the super-droplet method, which replaces the bulk cloud and rain microphysics scheme (Andrejczuk et al., 2008; 2010; Shima et al., 2009; Riechelmann et al., 2012), a two-way coupled LD model replaces the bulk rain microphysics scheme of the Eulerian LES. With a two-way coupled LD model thermodynamical feedbacks can be investigated, e.g., cold pool formation and the subsequent organisation of cumulus convection due to evaporative cooling in the subcloud layer.

We show in Chapter 3 that some uncertainty remains for the effect of the subgrid-scale velocity on the collision rates because the applied Lagrangian subgrid-scale model from Weil et al. (2004) does not take into account subgrid-scale velocity correlations among LD in close vicinity. This uncertainty can be investigated by implementing a Lagrangian

subgrid-scale model that takes into account temporal and spatial correlations for multiple particles such as the Lagrangian subgrid-scale model developed by Mazzitelli et al. (2014b).

Third, in the current implementation of the LD model neither hydrodynamic drop breakup nor drop breakup following the collision of two raindrops other than simple drop rebounding are taken into account. While hydrodynamic drop breakup only takes place for very large raindrop (with diameters > 8 mm), drop breakup following a collision event can be important already for medium sized raindrops, e.g., in mixed-phase deep convective clouds (Low and List, 1982; Seifert et al., 2005; Straub et al., 2010). A detailed implementation of raindrop breakup in the LD model is not straightforward, because fragments after a breakup event can be numerous and have vastly different sizes. Hence, the number of LDs may increase substantially, which increases the computational cost of the LD model.

Fourth, an extension of the LD model to include ice microphysics seems promising. Ice microphysics are much less well understood than warm rain formation. The fragmentation of freezing raindrops is suggested to support glaciation of cumulus cloud tops (Rangno, 2008) and particle-based simulations might help to quantify the effect. The LD model can also be extended by adding different ice categories to analyse deep convective clouds including their cirrus outflow regions (Sölch and Kärcher, 2010) or the effect of melting of ice particles on precipitation characteristics (Phillips et al., 2007; Frick et al., 2013). Especially for processes that lead to changes in particle shape or density, a Lagrangian particle approach, which takes into account the history of individual particles, has clear advantages over classic bin or bulk methods.

Comparison to observational data

By providing variables at high spatial and temporal resolution, numerical simulations offer a great opportunity to develop ideas and understanding of atmospheric processes. But even very high resolution models have several limitations mostly due to subgrid-scale processes that have to be parametrised such as radiation, turbulence and microphysics. Therefore, it is essential to test ideas and understanding gained from numerical modelling outside the modelling framework.

The shape of the RSD has been studied frequently with observational data, but those studies are often limited to the surface (Marshall and Palmer, 1948; Zhang et al., 2001; 2003; Munchak and Tokay, 2008). Geoffroy et al. (2014) analysed in-situ measurements of the RSD from aircraft flights that transected shallow cumulus clouds and found a large variability of the shape parameter. We speculate that this large variability reported by Geoffroy et al. (2014) might be caused by the typical sampling strategy of aircraft research flights probing a field of shallow cumulus clouds, i.e., clouds in different stages of their lifecycle. Our analyses in Chapter 4 shows a clear dependence of the shape parameter

of the RSD on the cloud lifecycle and on the height. We therefore suggest to analyse in-situ observations of RSDs in a cloud as well as in the subcloud layer with respect to the lifecycle of the cloud and the height of the measurement. To do so, measurements need an additional information indicating the stage of a clouds lifecycle, which is not straightforward to obtain but different ideas have been discussed recently (Witte et al., 2014; Schmeissner et al., 2015). One possibility is to obtain measurements of the RSD from helicopter-borne observations such as ACTOS (Airborne Cloud Turbulence Observation System), which probe individual clouds during different stages of their lifecycle (Siebert et al., 2006; Katzwinkel et al., 2014; Schmeissner et al., 2015).

Indications of recirculation of raindrops are probably much harder to obtain from observations because to our knowledge there exists no measurement devise that can follow the trajectory of individual raindrops to observe their lifecycles or that can estimate the age of a raindrop. Effects of recirculating raindrops such as a broadening of the RSD do not prove the occurrence of recirculating raindrops, since a broadening of the RSD can also be caused by other mechanisms than recirculation, e.g., by entrainment of environmental air into the cloud.

If a prove for the occurrence of recirculating raindrops from observational data is not possible, another strategy is to ask the negating question: Which observation can rule out the recirculation of raindrops? Here, we suggest to compare observed rainwater characteristics in the cloud environment of shallow cumulus, i.e., outside the cloud but within the cloud layer, with those simulated by the LD model, possibly as a function of distance from cloud edge. In Chapter 5 we find that most raindrops leave the cloud laterally rather than through cloud base, that cloud-edge recirculation is common, i.e., that raindrops leave and reenter the cloud, and that the mean distance to the cloud edge during the recirculation period can be as large as 200 m. Using aircraft measurements, Geoffroy et al. (2014) report on the height dependent distribution of, e.g., the raindrop number density, the rainwater mixing ratio and the mean raindrop diameter in environmental air of shallow cumulus clouds. If recirculation of raindrops is a common phenomena in nature, observed raindrop characteristics in the environmental air of shallow cumulus clouds should match those simulated with the LD model. Vice versa: If observed raindrop characteristics in the environmental air of shallow cumulus clouds differ distinctly from those simulated, recirculation of raindrops as simulated with the LD model can be ruled out.

6.4. Conclusions

In this thesis, small-scale variability is found to be crucial for the parametrisation of the cloud fraction and for particle-kinetic processes that lead to the formation of precipitation. For the parametrisation of the cloud fraction, the subgrid-scale variability is considered by applying a PDF-based approach that accounts for the characteristic cloud structures

of different shallow cloud regimes. For the closure equation of a bulk rain microphysics scheme, which determines the shape parameter of the RSD, the relation differs between individual clouds of the same regime and even more so between different cloud regimes when being related to a local variable, the mean raindrop diameter. Instead the shape of the RSD shows a clear dependence on the stage of the cloud's lifecycle, which shows that a non-local closure in time, i.e., a parametrisation that has explicit knowledge about the current state of the clouds relative to its overall lifecycle, is more appropriate.

One reason for the failure of a local closure in time for the shape of the RSD is related to the occurrence of recirculating raindrops, which contribute substantially to the surface precipitation of lightly precipitating shallow cumulus clouds. Complex trajectories and growth histories of raindrops that recirculate are neglected in highly idealised one-dimensional models of rain formation, which are often used to rationalise approximations or closure equations for parametrisations. Similarly, coarse resolution models that do not resolve the eddies that cause recirculation of raindrops omit a relevant process. Therefore, the effect of recirculating raindrops on the surface precipitation of shallow cumulus should be implemented in microphysics parametrisations of NWP models and GCMs.

A. Derivation of the assumed PDF

The distribution $P(s) = P_S(s)$ in Eq. 2.2 for a given region (e.g., the LES domain) is a marginal of a joint PDF, $P_{SI}(s, i)$,

$$P_S(s) = \int P_{SI}(s, i) di . \quad (\text{A.1})$$

The discrete random variable I , which is commonly used in turbulent flows to introduce conditional statistics (e.g., Pope, 2000), is defined to take different values in different subregions. As subregions we choose to distinguish between thermal areas ($I = 1$) and its well-mixed environment ($I = 2$) in case of shallow cumulus or between the well-mixed environment ($I = 1$) and downdrafts ($I = 2$) in case of stratocumulus. Then the distribution of I can be written as

$$P_I(i) = a\delta(i - 1) + (1 - a)\delta(i - 2), \quad (\text{A.2})$$

where δ is the Dirac delta function and a is the area fraction of the thermals in a shallow cumulus regime or the area fraction of the well-mixed environment in a stratocumulus regime.

For the joint PDF Bayes' theorem gives

$$P_{SI}(s, i) = P_{S|I}(s|I = i) P_I(i), \quad (\text{A.3})$$

where $P_{S|I}(s|I = i)$ is the conditional PDF of s in the subregion i . Inserting Eqs. A.2 and

A.3 in Eq. A.1, we arrive at

$$\begin{aligned} P_S(s) &= \int P_{S|I}(s|I=i)(a\delta(i-1) + (1-a)\delta(i-2))di \\ &= aP_{S|I}(s|I=1) + (1-a)P_{S|I}(s|I=2) \\ &= aP_1(s) + (1-a)P_2(s) \end{aligned} \tag{A.4}$$

Assuming that the PDFs of s in the subregions, P_1 and P_2 , are Gaussian distributed, Eq. A.4 is equal to Eq. 2.2. Therefore, in the shallow cumulus regime a , the relative amplitude of the two single-Gaussian distributions, can be directly interpreted as the area fraction of the thermals while in the stratocumulus regime $(1-a)$ is the area fraction of the downdrafts.

B. Density dependence of the terminal fall velocity

The terminal fall velocity of a raindrop is not solely determined by its mass but also depends on the air density. For the LD model this is taken into account via the temperature dependency of the air viscosity. (The pressure dependence is much smaller and thus neglected.) For a bulk rain microphysics scheme, the deceleration of a raindrop with increasing density, i.e., decreasing height, is usually considered by applying a density correction to the terminal fall velocity that is valid for sea level conditions, $v_{t,0}$. The terminal fall velocity at any height, v_t , is then given by Beard (1985)

$$\frac{v_t}{v_{t,0}} = \left(\frac{\rho_{a,0}}{\rho_a} \right)^m \quad (\text{B.1})$$

where $\rho_{a,0}$ is the air density at sea level, ρ_a is the actual air density and m is the air density exponent. When taking the temperature dependence of the air viscosity into account (Sutherland, 1893), using the approach of Abraham (1970) to calculate the drag coefficient (Eq. 3.5) and assuming a standard atmosphere to relate the air density and the temperature, m is increasing from about 0.2 for cloud droplets to 0.5 for large raindrops, i.e., small droplets decelerate less with decreasing height than large raindrops (Fig. B.1). Very similar values of m are obtained using the temperature and pressure correction from Khvorostyanov and Curry (2005). In contrast, neglecting the temperature dependence of the air viscosity results in increasing values of m with decreasing drop radius, i.e., an erroneous dependence of m on drop size. Because for large raindrops it is well established that m approaches 0.5, bulk rain microphysics schemes typically assume $m = 0.5$ when accounting for the density dependence of the terminal fall velocities of raindrops. In this study raindrops have a typical radius of 100 μm to 200 μm and therefore we choose to use a lower, more appropriate value of $m = 0.35$ in the bulk rain microphysics scheme (raindrop sedimentation and accretion).

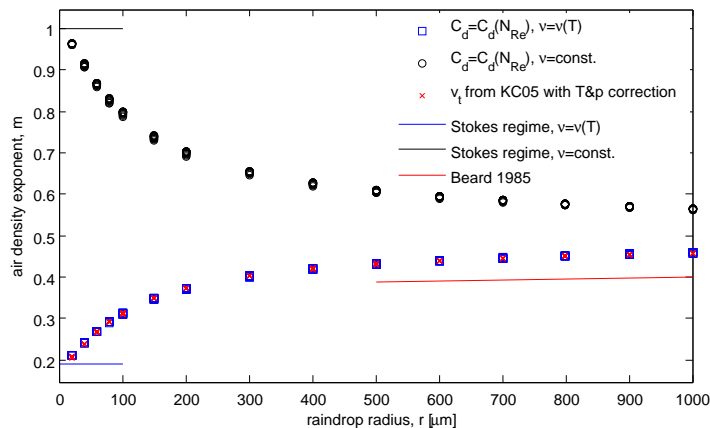


Figure B.1.: Air density exponent, m , as a function of the raindrop radius for different assumptions of the air viscosity.

C. Numerical integration of the LD's momentum equation

The development of the LD's velocity and the LD's position are given by Eq. 3.1 and

$$\frac{d\vec{x}}{dt} = \vec{v}_d \quad (\text{C.1})$$

respectively, where \vec{x} is the LD's position. Both equations have to be solved numerically in the LD model. Because the relaxation time scale, τ_d , is small, especially for small LDs, the numerical integration with an explicit Euler scheme and also with a third order Runge–Kutta scheme becomes unstable for the momentum equation for small drop sizes. In this study, we therefore use a mixed approach of the analytical solution (Eq. 3.4) for the LD velocity (with a predictor-corrector method for τ_d), and a third order Runge–Kutta scheme for the LD position. This mixed approach is stable also for small drops and gives more accurate results than the explicit Euler method or the third order Runge–Kutta scheme for large drops (Fig. C.1).

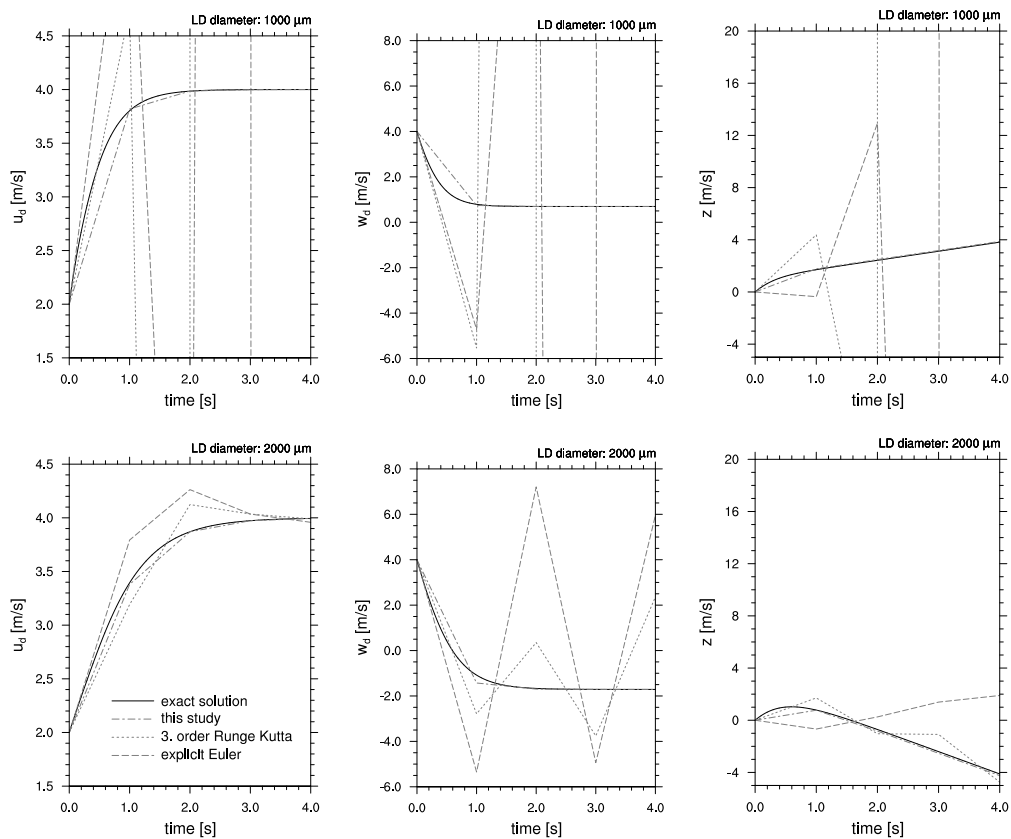


Figure C.1.: Comparison of three different numerical schemes for LDs with diameters $D = 1000 \mu\text{m}$ (upper row) and $D = 2000 \mu\text{m}$ (lower row). The initial LD velocity is $\vec{v}_{d,0} = (2, 2, 4) \text{ m/s}$. The flow velocity is assumed to be constant, $\vec{v}_a = (4, 4, 4.5) \text{ m/s}$. For smaller drop sizes the numerical solutions with the explicit Euler scheme and the third order Runge–Kutta scheme become immediately unstable and are therefore not shown.

D. Additional sample trajectories

To give an impression of different LD trajectories and their lifecycles in the context of the cloud they originate from we show a few sample trajectories in addition to Fig. 5.3 and Fig. 5.11.

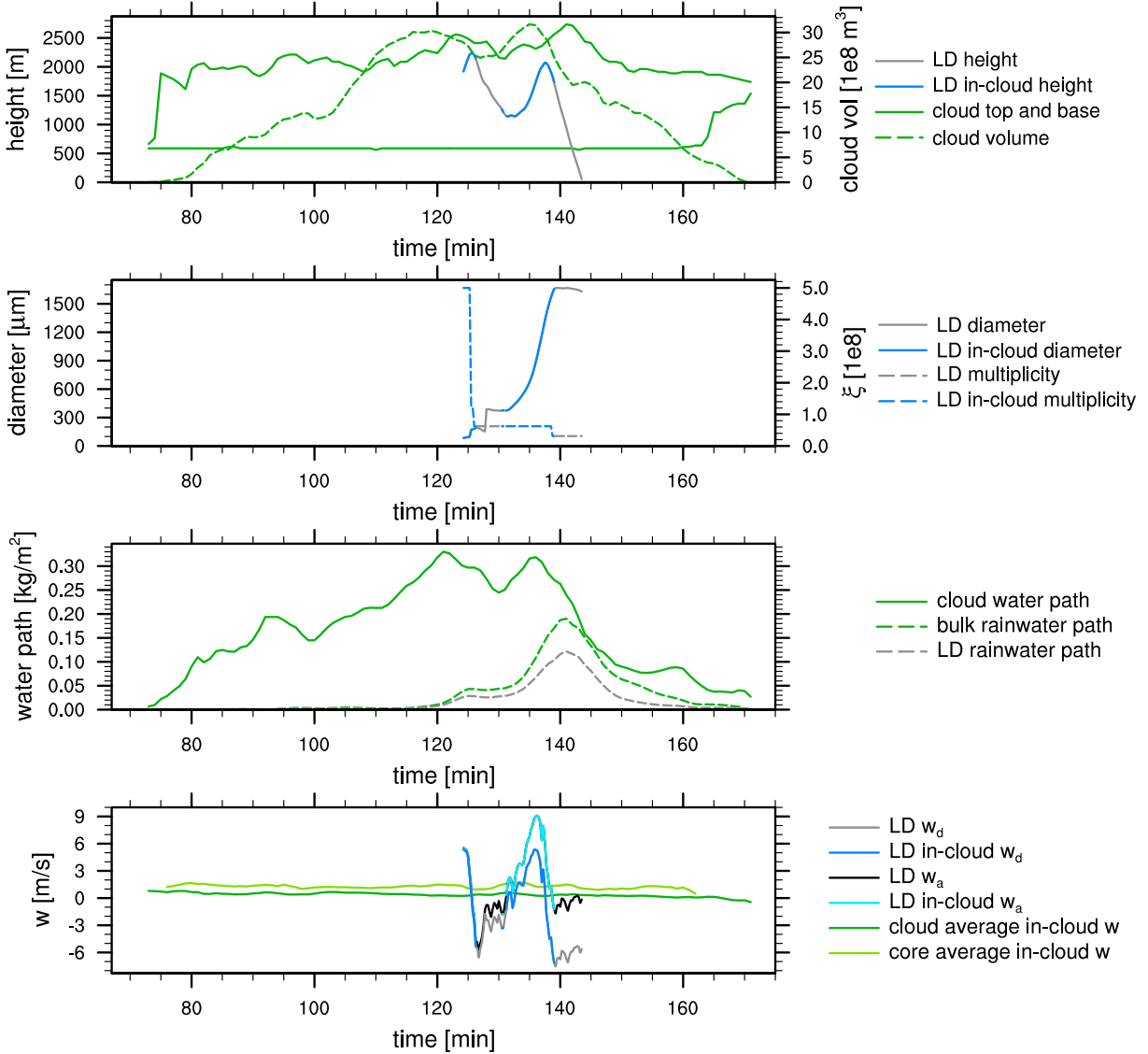


Figure D.1.: Sample trajectory of an LD that originates from the cloud that is precipitating most in the standard RICO simulation. In addition, properties of that cloud are shown. The LD shown experiences one cloud-edge recirculation and one 200-m recirculation.

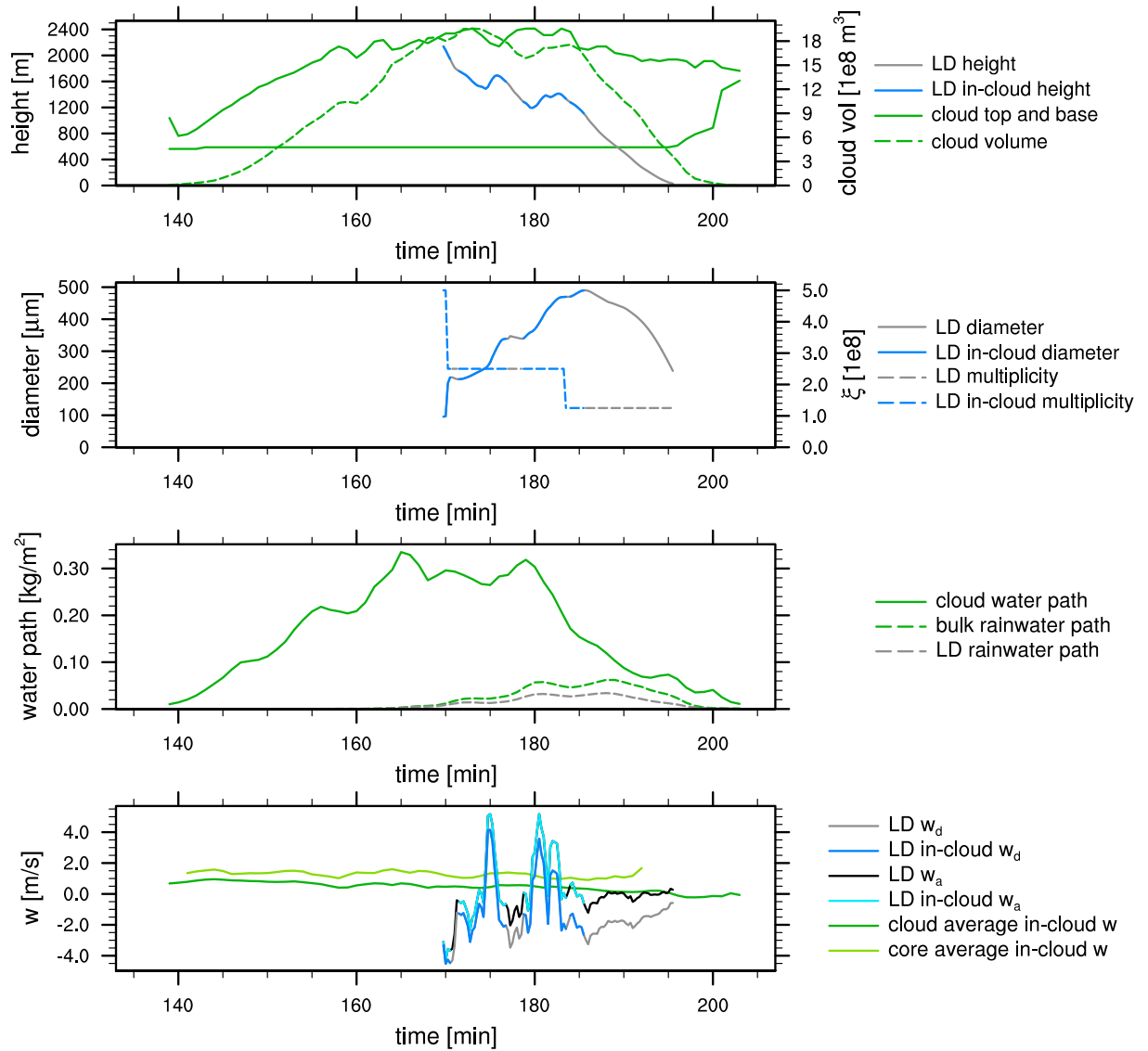


Figure D.2.: Sample trajectory of an LD from the standard RICO simulation and properties of the cloud it originates from. The LD shown experiences two cloud-edge recirculation and two 200-m recirculation.

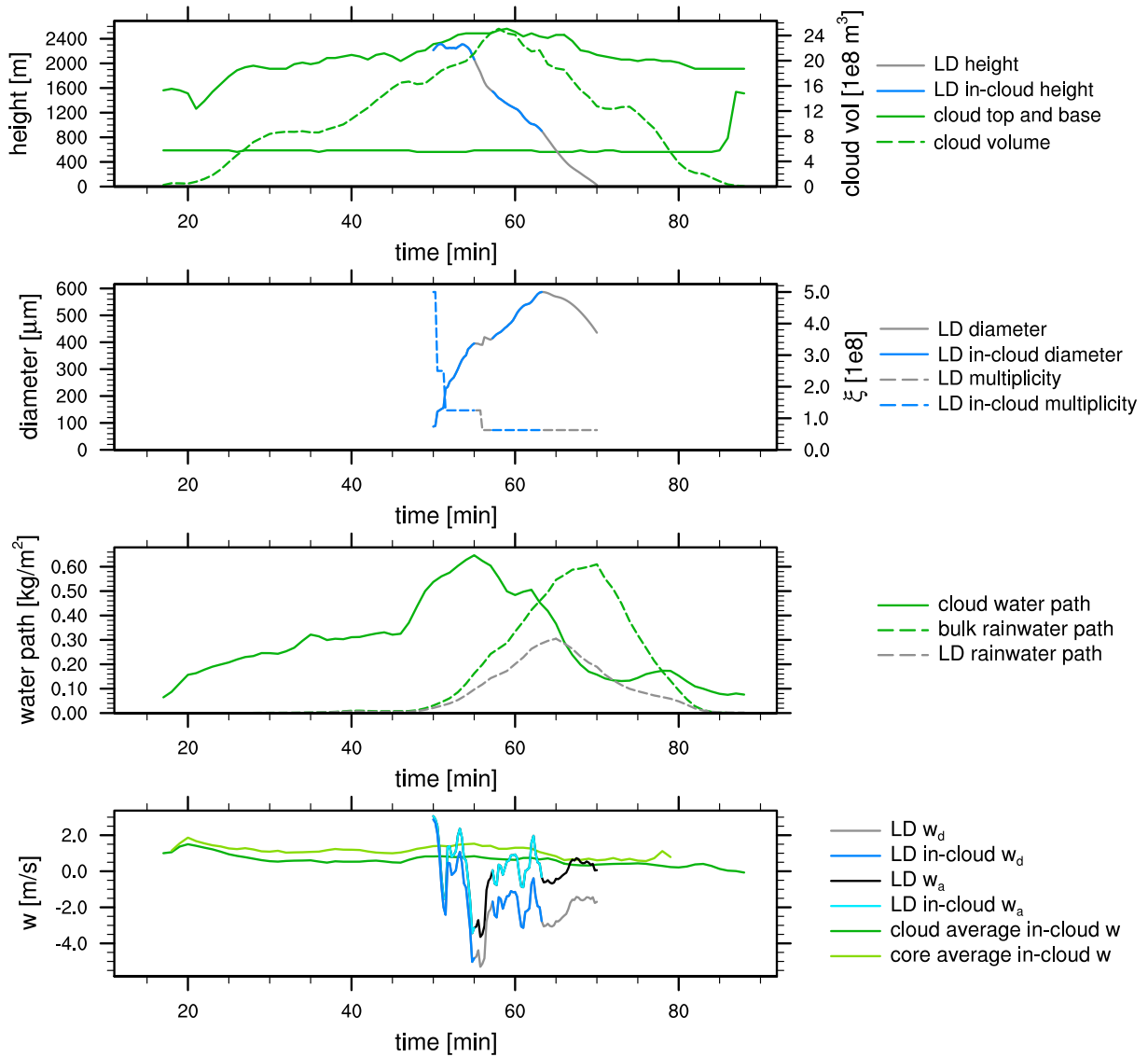


Figure D.3.: Sample trajectory of an LD from the moist RICO simulation and properties of the cloud it originates from. The LD shown experiences no cloud-edge recirculation and no 200-m recirculation.

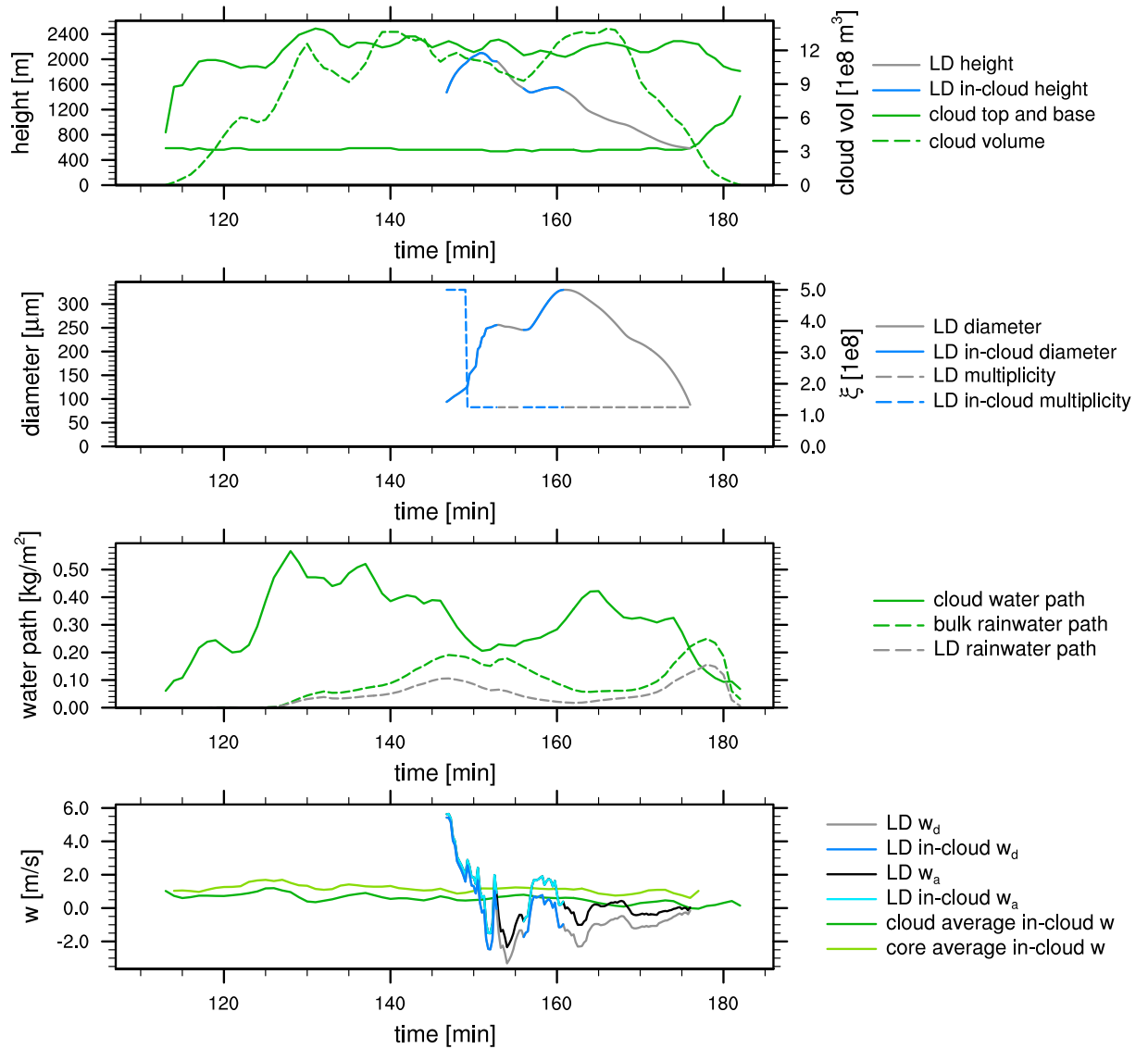


Figure D.4.: Sample trajectory of an LD from the moist RICO simulation and properties of the cloud it originates from. The LD shown experiences one cloud-edge recirculation but no 200-m recirculation.

BIBLIOGRAPHY

- Abraham, F. F., 1970: Functional dependence of drag coefficient of a sphere on Reynolds number. *Phys. Fluids*, **13**, 2194–2195.
- Albrecht, B. A., C. S. Bretherton, D. Johnson, W. H. Schubert, and A. S. Frisch, 1995: The Atlantic stratocumulus transition experiment – ASTEX. *Bull. Am. Met. Soc.*, **76**, 889–903.
- Andrejczuk, M., W. W. Grabowski, J. Reisner, and A. Gadian, 2010: Cloud-aerosol interactions for boundary layer stratocumulus in the Lagrangian cloud model. *J. Geophys. Res.*, **115**, doi:10.1029/2010JD014248.
- Andrejczuk, M., J. M. Reisner, B. Henson, M. K. Dubey, and C. A. Jeffery, 2008: The potential impacts of pollution on a nondrizzling stratus deck: Does aerosol number matter more than type? *J. Geophys. Res.*, **113**, doi:10.1029/2007JD009445.
- Ayala, O., B. Rosa, and L.-P. Wang, 2008: Effects of turbulence on the geometric collision rate of sedimenting droplets. Part 2: Theory and parameterization. *New J. Phys.*, **10**, 075016.
- Baldauf, M., A. Seifert, J. Förstner, D. Majewski, M. Raschendorfer, and T. Reinhardt, 2011: Operational convective-scale numerical weather prediction with the COSMO model: Description and sensitivities. *Mon. Wea. Rev.*, **139**, 3887–3905, doi:10.1175/MWR-D-10-05013.1.
- Beard, K. V., 1976: Terminal velocity and shape of cloud and precipitation drops aloft. *J. Atmos. Sci.*, **33**, 851–864.

- 1985: Simple altitude adjustments to raindrop velocities for Doppler radar analysis. *J. Atmos. Ocean. Tech.*, **2**, 468–471.
- Beard, K. V. and H. T. Ochs, 1995: Collisions between small precipitation drops. Part II: Formulas for coalescence, temporary coalescence, and satellites. *J. Atmos. Sci.*, **52**, 3977–3996.
- Beard, K. V. and H. R. Pruppacher, 1971: A wind tunnel investigation of the rate of evaporation of small water drops falling at terminal velocity in air. *J. Atmos. Sci.*, **28**, 1455–1464.
- Bec, J., L. Biferale, A. S. Lanotte, A. Scagliarini, and F. Toschi, 2010: Turbulent dispersion of inertial particles. *J. Fluid Mech.*, **645**, 497–528.
- Beheng, K. D., 1994: A parameterization of warm cloud microphysical conversion processes. *Atmos. Res.*, **33**, 193–206.
- Bewley, J. L. and S. Lasher-Trapp, 2011: Progress on predicting the breadth of droplet size distributions observed in small cumuli. *J. Atmos. Sci.*, **68**, 2921–2929, doi:10.1175/JAS-D-11-0153.1.
- Bogenschutz, P. A., A. Gettelman, H. Morrison, V. E. Larson, C. Craig, and D. P. Schanen, 2013: Higher-order turbulence closure and its impact on climate simulations in the community atmosphere model. *J. Climate*, **26**, 9655–9676.
- Bony, S. and J.-L. Dufresne, 2005: Marine boundary layer clouds at the heart of tropical cloud feedback uncertainties in climate models. *Geophys. Res. Lett.*, **32**.
- Boucher, O., D. Randall, P. Artaxo, C. Bretherton, G. Feingold, P. Forster, V.-M. Kerminen, Y. Kondo, H. Liao, U. Lohmann, P. Rasch, S. Satheesh, S. Sherwood, B. Stevens, and X. Zhang: 2013, Clouds and aerosols. *Climate Change 2013: The Physical Science Basis. Contribution of Working Group I to the Fifth Assessment Report of the Intergovernmental Panel on Climate Change*, T. Stocker, D. Qin, G.-K. Plattner, M. Tignor, S. Allen, J. Boschung, A. Nauels, Y. Xia, V. Bex, and P. Midgley, eds., Cambridge University Press, Cambridge, United Kingdom and New York, NY, USA.
- Bougeault, P., 1982a: Cloud-ensemble relations based on the gamma probability distribution for the higher-order models of the planetary boundary layer. *J. Atmos. Sci.*, **39**, 2691–2700.
- 1982b: Modeling the trade-wind cumulus boundary layer. Part I: Testing the ensemble cloud relations against numerical data. *J. Atmos. Sci.*, **38**, 2414–2428.

-
- Brenguier, J.-L. and W. W. Grabowski, 1993: Cumulus entrainment and cloud droplet spectra: A numerical model within a two-dimensional dynamical framework. *J. Atmos. Sci.*, **50**, 120–136.
- Bretherton, C. S., S. K. Krueger, M. C. Wyant, P. Bechtold, E. van Meijgaard, and J. Teixeira, 1999: A GCSS boundary-layer cloud model intercomparison study of the first ASTEX Lagrangian experiment. *Boundary-Layer Meteorol.*, **93**, 341–380.
- Brown, A. R., R. T. Cederwall, A. Chlond, P. G. Duynkerke, J.-C. Golaz, M. Khairoutdinov, D. C. Lewellen, A. P. Lock, M. K. MacVean, C.-H. Moeng, R. A. J. Neggers, A. P. Siebesma, and B. Stevens, 2002: Large-eddy simulation of the diurnal cycle of shallow cumulus convection over land. *Quart. J. Roy. Met. Soc.*, **128**, 1075–1093, doi:10.1256/003590002320373210.
- Byers, H. R. and R. K. Hall, 1955: A census of cumulus-cloud height versus precipitation in the vicinity of Puerto Rico during the winter and spring of 1953-1954. *J. Meteor.*, **12**, 176–178.
- Certaine, J.: 1960, The solution of ordinary differential equations with large time constants. *Mathematical methods for digital computers*, Wiley, 128–132.
- Chosson, F., P. A. Vaillancourt, J. A. Milbrandt, M. Yau, and A. Zadra, 2014: Adapting two-moment microphysics schemes across model resolutions: Subgrid cloud and precipitation fraction and microphysical sub-time step. *J. Atmos. Sci.*, **71**, 2635–2653.
- Cooper, W. A., 1989: Effects of variable droplet growth histories on droplet size distributions. Part I: Theory. *J. Atmos. Sci.*, **46**, 1301–1311.
- Cooper, W. A., S. G. Lasher-Trapp, and A. M. Blyth, 2013: The influence of entrainment and mixing on the initial formation of rain in a warm cumulus cloud. *J. Atmos. Sci.*, **70**, 1727–1743.
- Cuijpers, J. W. M. and P. Bechtold, 1995: A simple parametrization of cloud water related variables for use in boundary layer models. *J. Atmos. Sci.*, **52**, 2486–2490.
- Devenish, B., P. Bartello, J.-L. Brenguier, L. Collins, W. Grabowski, R. IJzermans, S. Malinowski, M. Reeks, J. Vassilicos, L.-P. Wang, et al., 2012: Droplet growth in warm turbulent clouds. *Quart. J. Roy. Met. Soc.*, **138**, 1401–1429.
- Dufresne, J.-L. and S. Bony, 2008: An assessment of the primary sources of spread of global warming estimates from coupled atmosphere-ocean models. *J. Climate*, **21**, 5135–5144.
- Dussen, J., S. Roode, A. Ackerman, P. Blossey, C. Bretherton, M. Kurowski, A. Lock, R. Neggers, I. Sandu, and A. Siebesma, 2013: The GASS/EUCLIPSE model inter-

- comparison of the stratocumulus transition as observed during ASTEX: LES results. *J. Adv. Model. Earth Syst.*, **5**, 483–499.
- Eaton, J. K. and J. Fessler, 1994: Preferential concentration of particles by turbulence. *Int. J. Multiphase Flow*, **20**, 169–209.
- Falkovich, G., A. Fouxon, and M. Stepanov, 2002: Acceleration of rain initiation by cloud turbulence. *Nature*, **419**, 151–154.
- Falkovich, G. and A. Pumir, 2007: Sling effect in collisions of water droplets in turbulent clouds. *J. Atmos. Sci.*, **64**, 4497–4505.
- Feingold, G., I. Koren, T. Yamaguchi, and J. Kazil, 2015: On the reversibility of transitions between closed and open cellular convection. *Atmos. Chem. Phys. Discuss.*, **15**, 5553–5588, doi:10.5194/acpd-15-5553-2015.
- Feingold, G., A. McComiskey, D. Rosenfeld, and A. Sorooshian, 2013: On the relationship between cloud contact time and precipitation susceptibility to aerosol. *J. Geophys. Res.*, **118**, 10–544.
- Feingold, G., B. Stevens, W. R. Cotton, and A. S. Frisch, 1996: The relationship between drop in-cloud residence time and drizzle production in numerically simulated stratocumulus clouds. *J. Atmos. Sci.*, **53**, 1108–1122.
- Feingold, G., R. L. Walko, B. Stevens, and W. R. Cotton, 1998: Simulations of marine stratocumulus using a new microphysical parameterization scheme. *Atmos. Res.*, **47-48**, 505–528.
- Franklin, C. N., 2014: The effects of turbulent collision–coalescence on precipitation formation and precipitation-dynamical feedbacks in simulations of stratocumulus and shallow cumulus convection. *Atmos. Chem. Phys.*, **14**, 6557–6570.
- Franklin, C. N., P. A. Vaillancourt, and M. K. Yau, 2007: Statistics and parameterizations of the effect of turbulence on the geometric collision kernel of cloud droplets. *J. Atmos. Sci.*, **64**, 938–954.
- Frick, C., A. Seifert, and H. Wernli, 2013: A bulk parametrization of melting snowflakes with explicit liquid water fraction for the COSMO model. *Geosci. Model Dev.*, **6**, 1925–1939.
- Geoffroy, O., A. P. Siebesma, and F. Burnet, 2014: Characteristics of the raindrop distribution in RICO shallow cumulus. *Atmos. Chem. Phys.*, **14**, 10897–10909, doi:10.5194/acp-14-10897-2014.

-
- Gerber, H. E., G. M. Frick, J. B. Jensen, and J. G. Hudson, 2008: Entrainment, mixing, and microphysics in trade-wind cumulus. *J. Meteorol. Soc. Jpn. A*, **86**, 87–106.
- Gillespie, D. T., 1975: Three models for the coalescence growth of cloud drops. *J. Atmos. Sci.*, **32**, 600–607.
- Grabowski, W., 2014: Extracting microphysical impacts in large-eddy simulations of shallow cumulus. *J. Atmos. Sci.*, **71**, 4493–4499.
- Grabowski, W. W. and P. Vaillancourt, 1999: Comments on “Preferential concentration of cloud droplets by turbulence: Effects on the early evolution of cumulus cloud droplet spectra”. *J. Atmos. Sci.*, **56**, 1433–1436.
- Grabowski, W. W. and L.-P. Wang, 2013: Growth of cloud droplets in a turbulent environment. *Annu. Rev. Fluid Mech.*, **45**, 293–324, doi:10.1146/annurev-fluid-011212-140750.
- Gryanik, V. M. and J. Hartmann, 2002: A turbulence closure for the convective boundary layer based on a two-scale mass-flux approach. *J. Atmos. Sci.*, **59**, 2729–2744.
- Gryanik, V. M., J. Hartmann, S. Raasch, and M. Schröter, 2005: A refinement of the Millionshchikov quasi-normality hypothesis for convective boundary layer turbulence. *J. Atmos. Sci.*, **62**, 2632–2638.
- Gunn, R. and G. D. Kinzer, 1949: The terminal velocity of fall for water droplets in stagnant air. *J. Meteor.*, **6**, 243–248.
- Handwerker, J. and W. Straub, 2011: Optimal determination of parameters for gamma-type drop size distributions based on moments. *J. Atmos. Ocean. Tech.*, **28**, 513–529.
- Hawkins, E. and R. Sutton, 2011: The potential to narrow uncertainty in projections of regional precipitation change. *Clim. Dynam.*, **37**, 407–418.
- Helfand, H. M. and E. Kalnay, 1983: A model to determine open or closed cellular convection. *J. Atmos. Sci.*, **40**, 631–650.
- Heus, T. and H. J. J. Jonker, 2008: Subsiding shells around shallow cumulus clouds. *J. Atmos. Sci.*, **65**, 1003–1018, doi:10.1175/2007JAS2322.1.
- Heus, T., H. J. J. Jonker, H. E. A. V. den Akker, E. J. Griffith, M. Koutek, and F. H. Post, 2009: A statistical approach to the life cycle analysis of cumulus clouds selected in a virtual reality environment. *J. Geophys. Res.*, **114**, D06208, doi:10.1029/2008JD010917.
- Heus, T. and A. Seifert, 2013: Automated tracking of shallow cumulus clouds in large domain, long duration large eddy simulations. *Geosci. Model Dev.*, **6**, 1261–1273.

- Heus, T., G. van Dijk, H. J. J. Jonker, and H. E. A. V. den Akker, 2008: Mixing in shallow cumulus clouds studied by Lagrangian particle tracking. *J. Atmos. Sci.*, **65**, doi:10.1175/2008JAS2572.1.
- Jakob, C., 2014: Going back to basics. *Nature Climate Change*, **4**, 1024–1027.
- Jasper, K., J. Gurtz, and H. Lang, 2002: Advanced flood forecasting in alpine watersheds by coupling meteorological observations and forecasts with a distributed hydrological model. *J. Hydrol.*, **267**, 40–52.
- Jensen, J. B., S. Lee, P. B. Krummel, J. Katzfey, and D. Gogoasa, 2000: Precipitation in marine cumulus and stratocumulus. Part I: Thermodynamic and dynamic observations of closed cell circulations and cumulus bands. *Atmos. Res.*, **54**, 117–155.
- Johnson, R. W., D. V. Kliche, and P. L. Smith, 2011: Comparison of estimators for parameters of gamma distributions with left-truncated samples. *J. Appl. Meteorol. Climatol.*, **50**, 296–310.
- Katzwinkel, J., H. Siebert, T. Heus, and R. A. Shaw, 2014: Measurements of turbulent mixing and subsiding shells in trade wind cumuli. *J. Atmos. Sci.*, **71**, 2810–2822.
- Kessler, E., 1969: *On the distribution and continuity of water substance in atmospheric circulations*. Meteor. Monogr. 32, Amer. Meteor. Soc., Boston.
- Khairoutdinov, M. and Y. Kogan, 2000: A new cloud physics parameterization in a large-eddy simulation model of marine stratocumulus. *Mon. Wea. Rev.*, **128**, 229–243.
- Khvorostyanov, V. I. and J. A. Curry, 2002: Terminal fall velocities of droplets and crystals: Power laws with continuous parameters over the size spectrum. *J. Atmos. Sci.*, **59**, 1872–1884.
- 2005: Fall velocities of hydrometeors in the atmosphere: Refinements to a continuous analytical power law. *J. Atmos. Sci.*, **62**, 4343–4357.
- Kogan, Y. L., 2006: Large-eddy simulation of air parcels in stratocumulus clouds: Time scales and spatial variability. *J. Atmos. Sci.*, **63**, 952–967.
- Kostinski, A. B. and R. A. Shaw, 2005: Fluctuations and luck in droplet growth by coalescence. *Bull. Am. Met. Soc.*, 235–244.
- La Porta, A., G. A. Voth, A. M. Crawford, J. Alexander, and E. Bodenschatz, 2001: Fluid particle accelerations in fully developed turbulence. *Nature*, **409**, 1017–1019.
- Langmuir, I., 1948: The production of rain by a chain reaction in cumulus clouds at temperatures above freezing. *J. Meteor.*, **5**, 175–192.

-
- Larsen, M. L., A. B. Kostinski, and A. R. Jameson, 2014: Further evidence for superterminal raindrops. *Geophys. Res. Lett.*, **41**, 6914–6918, doi:10.1002/2014GL061397.
- Larson, V., J. Golaz, and W. Cotton, 2002: Small-scale and mesoscale variability in cloudy boundary layers: Joint probability density functions. *J. Atmos. Sci.*, **59**, 3519–3539.
- Larson, V. E., R. Wood, P. Field, J. Golaz, T. H. V. Haar, and W. Cotton, 2001a: Small-scale and mesoscale variability of scalars in cloudy boundary layers: One-dimensional probability density functions. *J. Atmos. Sci.*, **58**, 1978–1994.
- 2001b: Systematic biases in the microphysics and thermodynamics of numerical models that ignore subgrid-scale variability. *J. Atmos. Sci.*, **58**, 1117–1128.
- Lasher-Trapp, S., W. A. Cooper, and A. M. Blyth, 2005: Broadening of droplet size distribution from entrainment and mixing in a cumulus cloud. *Quart. J. Roy. Met. Soc.*, **131**, 195–220, doi:10.1256/qj.03.199.
- Lasher-Trapp, S., C. A. Knight, and J. M. Straka, 2001: Early radar echos from ultragrantic aerosol in cumulus congestus: Modeling and observations. *J. Atmos. Sci.*, **158**, 3545–3562.
- Lau, K. M. and H. T. Wu, 2003: Warm rain processes over tropical oceans and climate implications. *Geophys. Res. Lett.*, **30**, 2290.
- Lazo, J. K., M. Lawson, P. H. Larsen, and D. M. Waldman, 2011: US economic sensitivity to weather variability. *Bull. Am. Met. Soc.*, 709.
- Lewellen, W. S. and S. Yoh, 1993: Binormal model of ensemble partial cloudiness. *J. Atmos. Sci.*, **50**, 1228–1237.
- Low, T. B. and R. List, 1982: Collision, coalescence and breakup of raindrops. Part I: Experimentally established coalescence efficiencies and fragment size distributions in breakup. *J. Atmos. Sci.*, **39**, 1591–1606.
- Machulskaya, E. and D. Mironov, 2013: Implementation of TKE-scalar variance mixing scheme into COSMO. *COSMO newsletter*, **13**, 25–33.
- Magaritz, L., M. Pinsky, O. Krasnov, and A. Khain, 2009: Investigation of droplet size distributions and drizzle formation using a new trajectory ensemble model. Part II: Lucky parcels. *J. Atmos. Sci.*, **66**, 781–805.
- Magaritz-Ronen, L., M. Pinsky, and A. Khain, 2014: Effects of turbulent mixing on the structure and macroscopic properties of stratocumulus clouds demonstrated by a Lagrangian trajectory model. *J. Atmos. Sci.*, **71**, 1843–1862.

- Mansell, E. R., 2010: On sedimentation and advection in multimoment bulk microphysics. *J. Atmos. Sci.*, **67**, 3084–3094.
- Marshall, J. S. and W. M. K. Palmer, 1948: The distribution of raindrops with size. *J. Meteor.*, **5**, 165–166.
- Mason, B. J., 1971: *The Physics of Clouds*. Oxford University Press, second edition.
- Mazzitelli, I. M., F. Fornarelli, A. S. Lanotte, and P. Oresta, 2014a: Pair and multi-particle dispersion in numerical simulations of convective boundary layer turbulence. *Phys. Fluids*, **26**.
- Mazzitelli, I. M., F. Toschi, and A. S. Lanotte, 2014b: An accurate and efficient Lagrangian sub-grid model. *Phys. Fluids*, **26**.
- Mellado, J. P., B. Stevens, H. Schmidt, and N. Peters, 2010: Probability density functions in the cloud-top mixing layer. *New J. Phys.*, **12**, doi:10.1088/1367-2630/12/8/085010.
- Mellor, G. L., 1977: The Gaussian cloud model relations. *J. Atmos. Sci.*, **34**, 356–358.
- Milbrandt, J. and M. Yau, 2005: A multimoment bulk microphysics parameterization. Part I: Analysis of the role of the spectral shape parameter. *J. Atmos. Sci.*, **62**, 3051–3064.
- Milbrandt, J. A. and R. McTaggart-Cowan, 2010: Sedimentation-induced errors in bulk microphysics schemes. *J. Atmos. Sci.*, **67**, 3931–3948.
- Mironov, D.: 2009, Turbulence in the lower troposphere: Second-order closure and mass-flux modelling frameworks. *Interdisciplinary Aspects of Turbulence*, W. Hillebrandt and F. Kupka, eds., Springer Berlin Heidelberg, volume 756, 1–61.
- Moeng, C.-H. and R. Rotunno, 1990: Vertical-velocity skewness in the buoyancy-driven boundary layer. *J. Atmos. Sci.*, **47**, 1149–1162.
- Moisseev, D. N. and V. Chandrasekar, 2007: Examination of the μ - γ relation suggested for drop size distribution parameters. *J. Atmos. Ocean. Tech.*, **24**, 847–855.
- Montero-Martínez, G., A. B. Kostinski, R. A. Shaw, and F. García-García, 2009: Do all raindrops fall at terminal speed? *Geophys. Res. Lett.*, **36**, doi:10.1029/2008GL037111.
- Morrison, H., J. A. Curry, and V. I. Khvorostyanov, 2005: A new double-moment microphysics parameterization for application in cloud and climate models. Part I: Description. *J. Atmos. Sci.*, **62**, 1665–1677.
- Morrison, H. and W. W. Grabowski, 2007: Comparison of bulk and bin warm-rain microphysics models using a kinematic framework. *J. Atmos. Sci.*, **64**, 2839 – 2861.

-
- Munchak, S. J. and A. Tokay, 2008: Retrieval of raindrop size distribution from simulated dual-frequency radar measurements. *J. Appl. Meteorol. Climatol.*, **47**, 223–241.
- Neggers, R. A. J., M. Köhler, and A. C. M. Beljaars, 2009: A dual mass flux framework for boundary layer convection. Part I: Transport. *J. Atmos. Sci.*, **66**, 1465–1487.
- Olson, D. A., N. W. Junker, and B. Korty, 1995: Evaluation of 33 years of quantitative precipitation forecasting at the NMC. *Wea. Forecasting*, **10**, 498–511.
- Park, Y. and C. Lee, 2014: Gravity-driven clustering of inertial particles in turbulence. *Phys. Rev. E Stat. Nonlin. Soft Matter Phys.*, **89**, 061004(R).
- Perraud, E., F. Couvreux, S. Malardel, C. Lac, V. Masson, and O. Thouron, 2011: Evaluation of statistical distributions for the parametrization of subgrid boundary-layer clouds. *Boundary-Layer Meteorol.*, **140**, 263–294, doi:10.1007/s10546-011-9607-3.
- Phillips, V. T. J., A. Pokrovsky, and A. Khain, 2007: The influence of time-dependent melting on the dynamics and precipitation production in maritime and continental storm clouds. *J. Atmos. Sci.*, **64**, 338–359.
- Pielke, R. A., Jr and M. W. Downton, 2000: Precipitation and damaging floods: Trends in the United States, 1932–97. *J. Climate*, **13**, 3625–3637.
- Pimentel, D., C. Harvey, P. Resosudarmo, K. Sinclair, D. Kurz, M. McNair, S. Crist, L. Shpritz, L. Fitton, R. Saffouri, et al., 1995: Environmental and economic costs of soil erosion and conservation benefits. *Science*, **267**, 1117–1122.
- Pincus, R. and S. A. Klein, 2000: Unresolved spatial variability and microphysical process rates in large-scale models. *J. Geophys. Res.*, **105**, 27059–27065.
- Pinsky, M. and A. Khain, 1997a: Turbulence effects on the collision kernel. Part I: Formation of velocity deviations of drops falling within a turbulent three-dimensional flow. *Quart. J. Roy. Met. Soc.*, **123**, 1517–1542.
- 1997b: Turbulence effects on the collision kernel. Part II: Increase of swept volume of colliding drops. *Quart. J. Roy. Met. Soc.*, **123**, 1543–1560.
- Pinsky, M., L. Magaritz, A. Khain, O. Krasnov, and A. Sterkin, 2008: Investigation of droplet size distributions and drizzle formation using a new trajectory ensemble model. Part I: Model description and first results in a nonmixing limit. *J. Atmos. Sci.*, **65**, 2046–2086.
- Pinsky, M. B. and A. P. Khain, 2004: Collisions of small drops in a turbulent flow. Part II: Effects of flow accelerations. *J. Atmos. Sci.*, **61**, 1926–1939.

- Pinsky, M. B., A. P. Khain, B. Grits, and M. Shapiro, 2006: Collisions of small drops in a turbulent flow. Part III: Relative droplet fluxes and swept volumes. *J. Atmos. Sci.*, **63**, 2123–2139.
- Pope, S. B., 2000: *Turbulent flows*. Cambridge Univ. Press.
- Press, W. H., S. A. Teukolsky, W. T. Vetterling, and B. P. Flannery, 1992: *Numerical Recipes in FORTRAN*. Cambridge University Press, Cambridge.
- Pruppacher, H. R. and J. D. Klett, 1997: *Microphysics of Clouds and Precipitation*. Kluwer Academic Publishers, Dordrecht.
- Pruppacher, H. R. and R. Rasmussen, 1979: A wind tunnel investigation of the rate of evaporation of large water drops falling at terminal velocity in air. *J. Atmos. Sci.*, **36**, 1255–1260.
- Quaas, J., 2012: Evaluating the “critical relative humidity” as a measure of subgrid-scale variability of humidity in general circulation model cloud cover parameterizations using satellite data. *J. Geophys. Res.*, **117**, doi:10.1029/2012JD017495.
- Randall, D. A., R. Wood, S. Bony, R. Colman, T. Fichefet, J. Fyfe, V. Kattsov, A. Pitman, J. Shukla, J. Srinivasan, R. Stouffer, A. Sumi, and K. Taylor: 2007, Climate models and their evaluation. *Climate Change 2007: The Physical Science Basis. Contribution of Working Group I to the Fourth Assessment Report of the Intergovernmental Panel on Climate Change*, S. Solomon, D. Qin, M. Manning, Z. Chen, M. Marquis, K. Averyt, M. Tignor, and H. Miller, eds., Cambridge University Press, Cambridge, United Kingdom and New York, NY, USA.
- Rangno, A. L., 2008: Fragmentation of freezing drops in shallow maritime frontal clouds. *J. Atmos. Sci.*, **65**, 1455–1466.
- Rauber, R. M., B. Stevens, H. T. Ochs, III, C. Knight, B. A. Albrecht, A. M. Blyth, C. W. Fairall, J. B. Jensen, S. G. Lasher-Trapp, O. L. Mayol-Bracero, G. Vali, J. R. Anderson, B. A. Baker, A. R. Bandy, E. Burnet, J. L. Brenguier, W. A. Brewer, P. R. A. Brown, P. Chuang, W. R. Cotton, L. D. Girolamo, B. Geerts, H. Gerber, S. Goke, L. Gomes, B. G. Heikes, J. G. Hudson, P. Kollias, R. P. Lawson, S. K. Krueger, D. H. Lenschow, L. Nuijens, D. W. O’Sullivan, R. A. Rilling, D. C. Rogers, A. P. Siebesma, E. Snodgrass, J. L. Stith, D. C. Thornton, S. Tucker, C. H. Twohy, and P. Zuidema, 2007: Rain in shallow cumulus over the ocean - the RICO campaign. *Bull. Am. Met. Soc.*, **88**, 1912–1924, doi:10.1175/BAMS-88-12-1912.
- Riechermann, T., Y. Noh, and S. Raasch, 2012: A new method for large-eddy simulations of clouds with Lagrangian droplets including the effects of turbulent collision. *New J. Phys.*, **14**, doi:10.1088/1367-2630/14/6/065008.

-
- Riehl, H., T. Yeh, J. S. Malkus, and N. E. La Seur, 1951: The north-east trade of the Pacific Ocean. *Quart. J. Roy. Met. Soc.*, **77**, 598–626.
- Rodts, S. M., P. G. Duynkerke, and H. J. Jonker, 2003: Size distributions and dynamical properties of shallow cumulus clouds from aircraft observations and satellite data. *J. Atmos. Sci.*, **60**, 1895–1912.
- Rogers, R. R. and M. K. Yau, 1989: *A Short Course in Cloud Physics*, volume 113 of *International Series in Natural Philosophy*. Elsevier, 3rd edition.
- Rotstayn, L. D., 2000: On the “tuning” of autoconversion parameterizations in climate models. *J. Geophys. Res.*, **105**, 15495–15507.
- Saffman, P. G. and J. S. Turner, 1956: On the collision of drops in turbulent clouds. *J. Fluid Mech.*, **1**, 16–30.
- Sandu, I. and B. Stevens, 2011: On the factors modulating the stratocumulus to cumulus transitions. *J. Atmos. Sci.*, **68**, 1865–1881.
- Sant, V., U. Lohmann, and A. Seifert, 2013: Performance of a triclass parameterization for the collision–coalescence process in shallow clouds. *J. Atmos. Sci.*, **70**, 1744–1767.
- Savic-Jovicic, V. and B. Stevens, 2008: The structure and mesoscale organization of precipitating stratocumulus. *J. Atmos. Sci.*, **65**, 1587–1605.
- Schemann, V., 2014: *Towards a scale aware cloud process parameterization for global climate models*. Ph.D. thesis, Berichte zur Erdsystemforschung, **145**, Universität Hamburg.
- Schmeissner, T., R. Shaw, J. Ditas, F. Stratmann, M. Wendisch, and H. Siebert, 2015: Turbulent mixing in shallow trade wind cumuli: Dependence on cloud life cycle. *J. Atmos. Sci.*, in press, doi:10.1175/JAS-D-14-0230.1.
- Seifert, A., 2002: *Parametrisierung wolkenmikrophysikalischer Prozesse und Simulation konvektiver Mischwolken*. Ph.D. thesis, Institut für Meteorologie und Klimaforschung, Universität Karlsruhe, Karlsruhe (in German).
- 2005: A note on the shape-slope relation of the drop size distribution in convective rain. *J. Appl. Met.*, **44**, 1146–1151.
- 2008: On the parameterization of evaporation of raindrops as simulated by a one-dimensional rainshaft model. *J. Atmos. Sci.*, **65**, 3608–3619.
- Seifert, A. and K. D. Beheng, 2001: A double-moment parameterization for simulating autoconversion, accretion and selfcollection. *Atmos. Res.*, **59-60**, 265–281.

- Seifert, A., U. Blahak, and R. Buhr, 2014: On the analytic approximation of bulk collision rates of non-spherical hydrometeors. *Geosci. Model Dev.*, **463–478**, doi:10.5194/gmd-7-463-2014.
- Seifert, A. and T. Heus, 2013: Large-eddy simulation of organized precipitating trade wind cumulus clouds. *Atmos. Chem. Phys.*, **13**, 5631–5645, doi:10.5194/acp-13-5631-2013.
- Seifert, A., A. Khain, U. Blahak, and K. D. Beheng, 2005: Possible effects of collisional breakup on mixed-phase deep convection simulated by a spectral bin cloud model. *J. Atmos. Sci.*, **62**, 1917–1931.
- Seifert, A., L. Nuijens, and B. Stevens, 2010: Turbulence effects on warm-rain autoconversion in precipitating shallow convection. *Quart. J. Roy. Met. Soc.*, **136**, 1753–1762, doi:10.1002/qj.684.
- Seifert, A. and B. Stevens, 2010: Microphysical scaling relations in a kinematic model of isolated shallow cumulus clouds. *J. Atmos. Sci.*, **67**, 1575–1590.
- Shaw, R. A., 2003: Particle-turbulence interactions in atmospheric clouds. *Annu. Rev. Fluid Mech.*, **35**, 183–227.
- Shaw, R. A., W. C. Reade, L. R. Collins, and J. Verlinde, 1998: Preferential concentration of cloud droplets by turbulence: Effects on the early evolution of cumulus cloud droplet spectra. *J. Atmos. Sci.*, **55**, 1965–1976.
- Shima, S., K. Kusano, A. Kawano, T. Sugiyama, and S. Kawahara, 2009: The super-droplet method for the numerical simulation of clouds and precipitation: A particle-based and probabilistic microphysics model coupled with a non-hydrostatic model. *Quart. J. Roy. Met. Soc.*, **135**, doi:10.1002/qj.441.
- Short, D. A. and K. Nakamura, 2000: TRMM radar observations of shallow precipitation over tropical oceans. *J. Climate*, **13**, 41070–4124.
- Sidin, R. S., R. H. IJzermans, and M. W. Reeks, 2009: A Lagrangian approach to droplet condensation in atmospheric clouds. *Phys. Fluids*, **21**, 106603.
- Siebert, H., K. Lehmann, M. Wendisch, H. Franke, R. Maser, D. Schell, E. Wei Saw, and R. A. Shaw, 2006: Probing finescale dynamics and microphysics of clouds with helicopter-borne measurements. *Bull. Am. Met. Soc.*, **87**, 1727–1738.
- Simpson, G. C., 1941: On the formation of cloud and rain. *Quart. J. Roy. Met. Soc.*, **67**, 99–133.
- Slingo, J. M., 1987: The development and verification of a cloud prediction scheme for the ECMWF model. *Quart. J. Roy. Met. Soc.*, **113**, 899–927.

- Smagorinsky, J.: 1960, On the dynamical prediction of large-scale condensation by numerical methods. *Physics of Precipitation*, American Geophysical Union, Washington, U.S.A, number 5 in Geophys. Mon., 71–78.
- Smiatek, G., H. Kunstmann, and J. Werhahn, 2012: Implementation and performance analysis of a high resolution coupled numerical weather and river runoff prediction model system for an alpine catchment. *Environ. Modell. Softw.*, **38**, 231–243.
- Soden, B. J. and I. M. Held, 2006: An assessment of climate feedbacks in coupled ocean-atmosphere models. *J. Climate*, **19**, 3354–3360.
- Sölch, I. and B. Kärcher, 2010: A large-eddy model for cirrus clouds with explicit aerosol and ice microphysics and Lagrangian ice particle tracking. *Quart. J. Roy. Met. Soc.*, **136**, 2074–2093.
- Sommeria, G. and J. W. Deardorff, 1977: Subgrid-scale condensation in models of non-precipitating clouds. *J. Atmos. Sci.*, **34**, 344–355.
- Stephens, G. L., T. L’Ecuyer, R. Forbes, A. Gettleman, J.-C. Golaz, A. Bodas-Salcedo, K. Suzuki, P. Gabriel, and J. Haynes, 2010: Dreary state of precipitation in global models. *J. Geophys. Res.*, **115**.
- Stevens, B., 2007: On the growth of layers of non-precipitating cumulus convection. *J. Atmos. Sci.*, **64**, 2916–2931.
- Stevens, B. and S. Bony, 2013: What are climate models missing? *Science*, **340**, 1053–1054.
- Stevens, B., G. Feingold, W. R. Cotton, and R. L. Walko, 1996a: Elements of microphysical structure of numerically simulated nonprecipitating stratocumulus. *J. Atmos. Sci.*, **53**, 980–1006.
- Stevens, B., D. Lenschow, G. Vali, H. Gerber, A. Bandy, B. Blomquist, J. Brenguier, C. Bretherton, F. Burnet, T. Campos, et al., 2003: Dynamics and chemistry of marine stratocumulus – DYCOMS-II. *Bull. Am. Met. Soc.*, **84**, 579–594.
- Stevens, B., C. Moeng, A. Ackerman, C. Bretherton, A. Chlond, S. De Roode, J. Edwards, J. Golaz, H. Jiang, M. Khairoutdinov, M. Kirkpatrick, D. Lewellen, A. Lock, F. Muller, D. Stevens, E. Whelan, and P. Zhu, 2005a: Evaluation of large-eddy simulations via observations of nocturnal marine stratocumulus. *Mon. Wea. Rev.*, **133**, 1443–1462.
- Stevens, B., C.-H. Moeng, and P. P. Sullivan, 1999: Large-eddy simulations of radiatively driven convection: sensitivities to representation of small scales. *J. Atmos. Sci.*, **56**, 3963–3984.

- Stevens, B. and A. Seifert, 2008: Understanding macrophysical outcomes of microphysical choices in simulations of shallow cumulus convection. *J. Met. Soc. Jap.*, **86**, 143–162.
- Stevens, B., G. Vali, K. Comstock, R. Wood, C. van Zanten, P. H. Austin, C. S. Bretherton, and D. H. Lenschow, 2005b: Pockets of open cells and drizzle in marine stratocumulus. *Bull. Am. Met. Soc.*, **86**, 51–57.
- Stevens, B., R. Walko, and W. Cotton, 1996b: The spurious production of cloud-edge supersaturation by Eulerian models. *Mon. Wea. Rev.*, **124**, 1034–1041.
- Straub, W., K. D. Beheng, A. Seifert, J. Schlottke, and B. Weigand, 2010: Numerical investigation of collision-induced breakup of raindrops. Part II: Parameterizations of coalescence efficiencies and fragment size distributions. *J. Atmos. Sci.*, **67**, 576–588.
- Sui, C.-H., X. Li, and M.-J. Yang, 2007: On the definition of precipitation efficiency. *J. Atmos. Sci.*, **64**, 4506–4513.
- Sundqvist, H., 1978: A parameterization scheme for non-convective condensation including prediction of cloud water content. *Quart. J. Roy. Met. Soc.*, **104**, 677–690.
- Sundqvist, H., E. Berge, and J. E. Kristjánsson, 1989: Condensation and cloud parameterization studies with a mesoscale numerical weather prediction model. *Mon. Wea. Rev.*, **117**, 1641–1657.
- Sutherland, W., 1893: The viscosity of gases and molecular force. *Philosophical Magazine*, **5**, 507–531.
- Telford, J., 1955: A new aspect of coalescence theory. *J. Meteor.*, **12**, 436–444.
- Tompkins, A. M., 2002: A prognostic parameterization for the subgrid-scale variability of water vapor and clouds in large-scale models and its use to diagnose cloud cover. *J. Atmos. Sci.*, **59**, 1917–1942.
- Toschi, F. and E. Bodenschatz, 2009: Lagrangian properties of particles in turbulence. *Annu. Rev. Fluid Mech.*, **41**, 375–404.
- Ulbrich, C. W., 1983: Natural variations in the analytical form of the raindrop size distribution. *J. Clim. Appl. Met.*, **22**, 1764–1775.
- Vaillancourt, P. and M. Yau, 2000: Review of particle-turbulence interactions and consequences for cloud physics. *Bull. Am. Met. Soc.*, **81**, 285–298.
- van Zanten, M. C. and B. Stevens, 2005: Observations of the structure of heavily precipitating marine stratocumulus. *J. Atmos. Sci.*, **62**, 4327–4342.

-
- van Zanten, M. C., B. Stevens, L. Nuijens, A. P. Siebesma, A. S. Ackerman, F. Burnet, A. Cheng, F. Couvreur, H. Jiang, M. Khairoutdinov, Y. Kogan, D. C. Lewellen, D. Mechem, K. Nakamura, A. Noda, B. J. Shipway, J. Slawinska, S. Wang, and A. Wyszogrodzki, 2011: Controls on precipitation and cloudiness in simulations of trade-wind cumulus as observed during RICO. *J. Adv. Model. Earth Syst.*, **3**, doi:10.1029/2011MS000056.
- Voßkuhle, M., A. Pumir, E. Lévêque, and M. Wilkinson, 2014: Prevalence of the sling effect for enhancing collision rates in turbulent suspensions. *J. Fluid Mech.*, **749**, 841–852.
- Wacker, U. and C. Lüpkes, 2009: On the selection of prognostic moments in parameterization schemes for drop sedimentation. *Tellus*, **61A**, 498–511.
- Wacker, U. and A. Seifert, 2001: Evolution of rain water profiles resulting from pure sedimentation: Spectral vs. parameterized description. *Atmos. Res.*, **58**, 19–39.
- Walko, R. L., W. R. Cotton, M. P. Meyers, and J. Y. Harrington, 1995: New RAMS cloud microphysics parameterization. Part I: The single-moment scheme. *Atmos. Res.*, **38**, 29–62.
- Wang, H. and G. Feingold, 2009a: Modeling mesoscale cellular structures and drizzle in marine stratocumulus. Part I: Impact of drizzle on the formation and evolution of open cells. *J. Atmos. Sci.*, **66**, 3237–3256.
- 2009b: Modeling mesoscale cellular structures and drizzle in marine stratocumulus. Part II: The microphysics and dynamics of the boundary region between open and closed cells. *J. Atmos. Sci.*, **66**, 3257–3275.
- Wang, L.-P., O. Ayala, B. Rosa, and W. Grabowski, 2008: Turbulent collision efficiency of heavy particles relevant to cloud droplets. *New J. Phys.*, **10**, 075013.
- Wang, L.-P., B. Rosa, H. Gao, G. He, and G. Jin, 2009: Turbulent collision of inertial particles: point-particle based, hybrid simulations and beyond. *Int. J. Multiphas. Flow*, **35**, 854–867.
- Wang, L.-P., Y. Xue, O. Ayala, and W. W. Grabowski, 2006: Effects of stochastic coalescence and air turbulence on the size distribution of cloud droplets. *Atmos. Res.*, **82**, 416–432.
- Weil, J. C., P. P. Sullivan, and C.-H. Moeng, 2004: The use of large-eddy simulations in Lagrangian particle dispersion models. *J. Atmos. Sci.*, **61**, 2877–2887.
- Witte, M., P. Chuang, and G. Feingold, 2014: On clocks and clouds. *Atmos. Chem. Phys.*, **14**, 6729–6738.

- Wyszogrodzki, A., W. Grabowski, L.-P. Wang, and O. Ayala, 2013: Turbulent collision-coalescence in maritime shallow convection. *Atmos. Chem. Phys.*, **13**, 8471–8487.
- Xu, K.-M. and D. A. Randall, 1996: A semiempirical cloudiness parameterization for use in climate models. *J. Atmos. Sci.*, **53**, 3084–3102.
- Yamaguchi, T. and D. A. Randall, 2012: Cooling of entrained parcels in a large-eddy simulation. *J. Atmos. Sci.*, **69**, doi:10.1175/JAS-D-11-080.1.
- Yang, Y., G.-W. He, and L.-P. Wang, 2008: Effects of subgrid-scale modeling on Lagrangian statistics in large-eddy simulation. *J. Turbu.*, doi:10.1080/14685240801905360.
- Yin, Y., Z. Levin, T. G. Reisin, and S. Tzivion, 2000: The effects of giant cloud condensation nuclei on the development of precipitation in convective clouds a numerical study. *Atmos. Res.*, **53**, 91–116.
- Zhang, G., J. Vivekanandan, E. Brandes, R. Meneghini, and T. Kozu, 2003: The shape-slope relation in observed gamma raindrop size distributions: Statistical error or useful information? *J. Atmos. Ocean. Tech.*, **20**, 1106–1119.
- Zhang, G., J. Vivekanandan, and E. A. Brandes, 2001: A method for estimating rain rate and drop size distribution from polarimetric radar measurements. *IEEE Trans. Geosci. Remote Sens.*, **39**, 830–841.

ACKNOWLEDGEMENTS

First and foremost I would like to thank Axel Seifert for being such a great supervisor. I am deeply thankful that he gave me the opportunity for this work and that he never got tired of sharing his seemingly infinite scientific insights with me. He manages to have an eye on the fundamental processes and their parametrisation at the same time, an approach that I find really helpful. I hope that his twofold view is reflected somehow appropriately in this thesis.

Special thanks to my co-advisors Bjorn Stevens, Felix Ament and Cathy Hohenegger for scientific input and extremely encouraging and helpful panel meetings. Felix Ament is especially thanked for taking over without hesitation when university's regulations challenged us unexpectedly.

Thanks to the whole HErZ group, former and current members, for all the discussions and help in the last years. Especially, I would like to thank Vivek Sant for discussing warm and cold microphysics, Linda Schlemmer for her support with mastering the LES, Juan Pedro Mellado for discussing turbulent cloud structures and the details of the LD model, Alessandra Lanotte for discussing inertial particles, Robert Pincus for discussing model selection, Bart van Stratum and Thijs Heus for the barticles and finally Mirjana Sakradzija for making our office such a friendly place. Thanks also to the IMPRS office for their organisational effort and support. Thanks to Cathy Hohenegger, Vivek Sant, Juan Pedro Mellado, Florian Rauser and reviewers from GMD and JAMES, who read and commented on parts of this thesis.

Last but not least I would like to thank my parents for their unconditional support.

This research was carried out as part of the Hans-Ertel Centre for Weather Research. This research network of Universities, Research Institutes and the Deutscher Wetterdienst is funded by the BMVI (Federal Ministry of Transport and Digital Infrastructure).

Aus dieser Dissertation hervorgegangene Vorver- öffentlichungen

List of Publications

Naumann, A. K., A. Seifert and J. P. Mellado (2013): A refined statistical cloud closure using double-Gaussian probability density functions. *Geosci. Model Dev.*, **6**, 1641–1657, doi:10.5194/gmd-6-1641-2013.

Naumann, A. K. and A. Seifert (2015): A Lagrangian drop model to study warm rain microphysical processes in shallow cumulus. *J. Adv. Model. Earth. Syst.*, in review.

Eidesstattliche Versicherung

Declaration on oath

Hiermit erkläre ich an Eides statt, dass ich die vorliegende Dissertationsschrift selbst verfasst und keine anderen als die angegebenen Quellen und Hilfsmittel benutzt habe.

I hereby declare, on oath, that I have written the present dissertation by myself and have not used other than the acknowledged resources and aids.

Hamburg, 31. März 2015

